Modern Turboramjet Conceptual Design for a Supersonic Business Jet

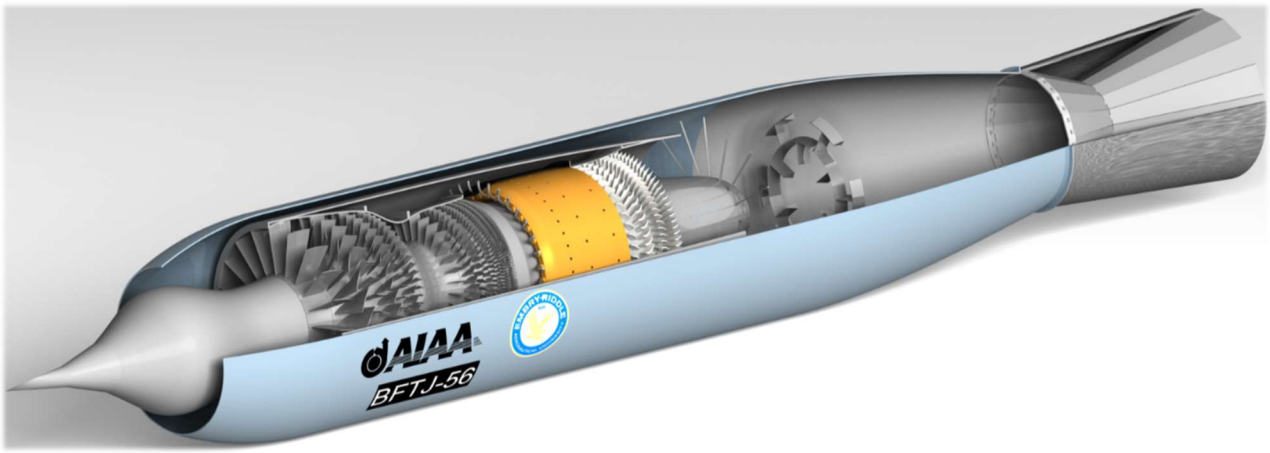

BFTJ-56

AIAA 2019 – 2020 Engine Design Competition

Embry-Riddle Aeronautical University

Department of Aerospace Engineering

Signature Page

Design Team:

Aranda, Bruno

Member # : 983794

Clares, Jorge

Member # : 1098214

Ferrand, Jesus

Member # : 1098215

Scott, Michael

Member # : 983780

Vavdiwala, Fahad

Member # : 1108928

Faculty Advisors:

Attia, Magdy, Ph.D

Member # : 230683

Ricklick, Mark, Ph.D

Member # : 495666

Executive Summary

A powerplant is designed for a Supersonic business Jet (SSBJ) with drag characteristics representative of the F-104 Starfighter. The aircraft is to travel round-trip from London to New York in one business day. The SSBJ must be able to cruise at both Mach number 2.1 and 0.98 over the Atlantic Ocean. The engine design is constrained by current nacelle dimensions and thrust required to overcome drag at steady-level flight.

The proposed propulsion system consists of two turboramjet engines designed at a flight condition with Mach number of 1.6 and an altitude of 40,000 [ft]. It is designed for an OPR of 20:1 with a 3-5-1-1 architecture. With recent material technology advancements known, the design TIT is 3700 [°R]. However, off-design analysis shows that maximum TIT is not required to ***meet*** thrust requirements. This engine provides a sea level static thrust of 45,232 [lb_f], 4.22% more than required while reducing TIT to 3613 [°R] (or -26.5%).

The ramjet is designed to operate only when max speed (Mach 3.0) is necessary. The turbojet will operate during all other flight conditions. This variable cycle is possible due to a bypass duct and an actuation system similar to that of the SR-71 powerplant, the PW-J58. The total length of the proposed engine is 26.6 [ft], 21.8% shorter than the given nacelle length. The largest cross-sectional diameter is 47.98 [in], 2.5% smaller than the given nacelle diameter, 49.2 [in]. The LPC and the HPC operate well off-design with the lowest surge margins of 22.4% and 26.9%, respectively.

The turbine system was designed to operate in a high temperature environment. Due to recent material technology advancements, neither the HPT nor LPT will require cooling. However, to alleviate thermal stresses, vanes and blades are protected by two layers of Thermal Barrier Coatings (TBC). Additionally, the turbine was designed to not need an inter-turbine duct.

A convergent-divergent nozzle is designed with variable geometry and has a length from nozzle-inlet to exit of 54.1 [in]. The variable geometry is to allow for perfect expansion for off-design performance. Because of the high amount of thrust required at different mission legs, a convergent-divergent nozzle will be able to provide the necessary jet velocity for the required thrust.

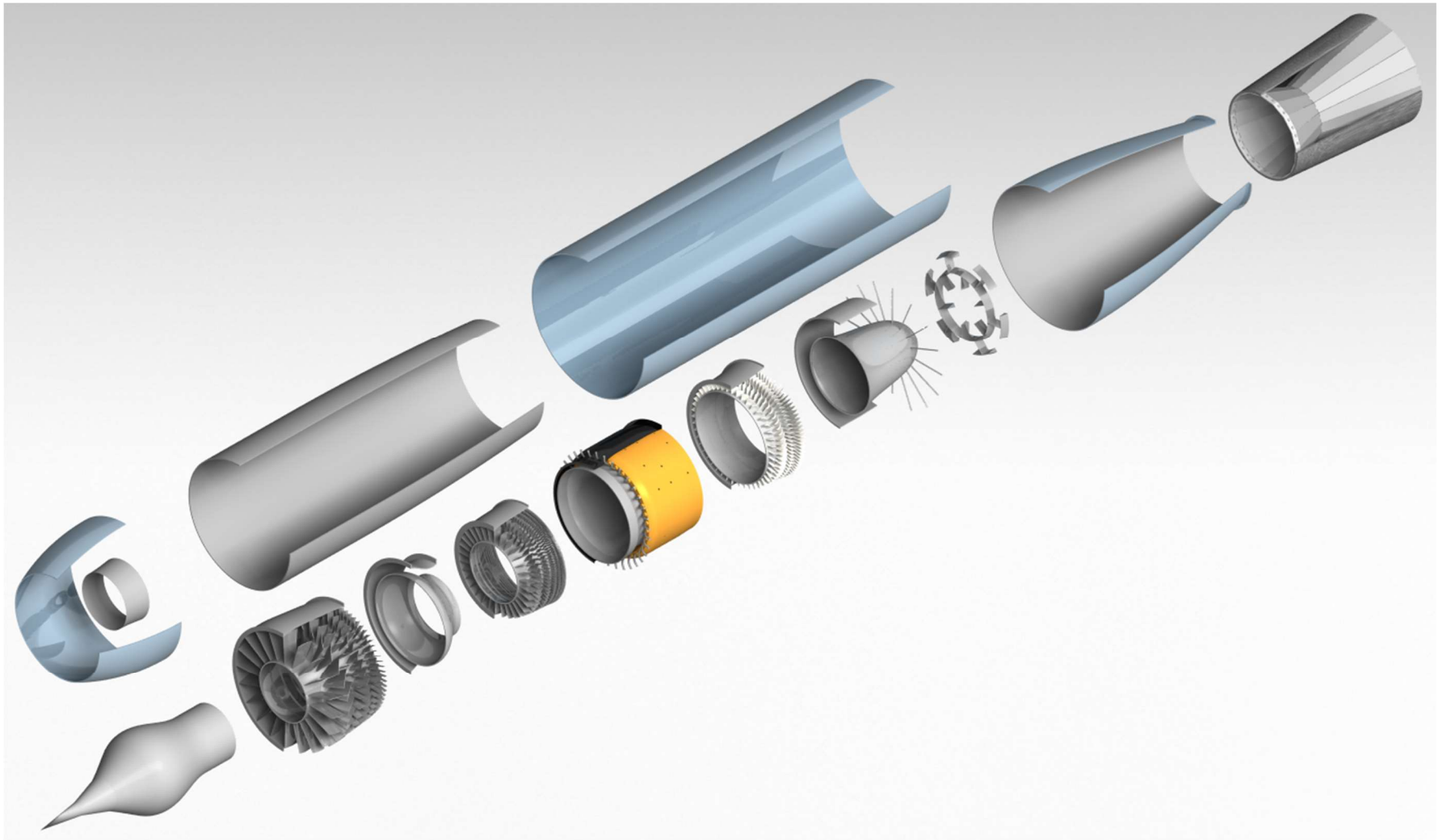

Nomenclature

BCA	=	Best Cruise Altitude
BL	=	Boundary Layer
C	=	Chord Length
e	=	Polytropic Efficiency
DF	=	Diffusion Factor
DH	=	Dehaller's Number
FOM	=	Figure of Merit
FPR	=	Fan Pressure Ratio
$F/\dot{m}$	=	Specific Thrust
h	=	Altitude
H/T	=	Hub-to-Tip Ratio
LE	=	Leading Edge
M	=	Mach Number
NS	=	Normal Shock
OS	=	Oblique Shock
°R	=	Degree of Reaction
S	=	pitch
$t_{\delta x}$	=	Spacing between R_{t1} and R_{t2}
T	=	Installed Thrust
TSFC	=	Thrust Specific Fuel Consumption
TIT	=	Turbine Inlet Temperature
T_{t7}	=	Ramjet Burner Temperature
η	=	Adiabatic Efficiency
λ	=	Stage Work Coefficient
π	=	Pressure Ratio
ϕ	=	Stage Flow Coefficient
σ	=	Solidity
σ_s	=	Stagger Angle
ρ	=	Density
τ	=	Total Temperature Ratio

Subscript

AB	=	Afterburner
b	=	Burner
cH	=	High Pressure Compressor
cL	=	Low Pressure Compressor
d	=	Diffuser
D	=	Duct
n	=	Nozzle
r	=	Ram/Recovery
R	=	Rotor
rel	=	Relative
S	=	Stator
SLS	=	Sea Level Static
tH	=	High Pressure Turbine
tL	=	Low Pressure Turbine

Table of Contents

List of Figures

List of Tables

1 Introduction

This report is a response to the AIAA Request for Proposal (RFP) to design a Propulsion System (PS) to power a Supersonic Business Jet (SSBJ) with an entry into service date of 2030. The specifications of the RFP are listed in the succeeding section. The proposed engine fits in the nacelle and outperforms the baseline engine outlined in the RFP (hereinafter "baseline engine"). The specifications of the SSBJ are listed in **Table 1** below.

Table 1: General Specifications of SSBJ

SSBJ Specifications	
Max ($\boldsymbol{W_{TO}}$)	146,000 [lb_m]
Wing Area ($\boldsymbol{S_w}$)	1,200 [ft^2]
Capacity	8 – 12 passengers
Crew	2
Current Propulsion System	2 x LBTF (21,700 [lb_f] each)

1.1 RFP Specification

The proposed engine complies with the following specifications regarding size, performance, and mission requirements. The size of the engine fits within the dimensions of the engine nacelle outlined in **Table 2.**

Table 2: SJ Engine Nacelle Limitations

Length	34.0 ft
Diameter	49.2 in
Area	13.2 ft^2

The engine produces the required thrust for the specified aircraft to travel round-trip from London to New York (4600 [nmi]) in 1 business day. Supercruise over the Atlantic Ocean, 3600 [nmi], must be completed under 2 hours while not exceeding a fuel burn of 96,000 [lbm]. The mission requirements are outlined in **Table 3.**

Table 3: Request for Proposal Specifications

RFP Specification	**Requirement**
Total Range	4600 [nmi]
Supercruise Range	3600 [nmi]
Supercruise Time Requirement	≤ 2 hours
Cruise Fuel Burn	≤ 96,000 [lb_m]

Table 4 outlines the considered mission legs used to dictate the cycle of the PS. Included are the steady-level flight thrust requirements provided by the RFP.

Table 4: Required thrust for a single engine

Mission Leg	Mach Number	Altitude [ft]	Required Thrust [lb_f]
1 (Subsonic Cruise)	0.98	40,000	5,050
3 (BCA)	1.15	40,000	10,700
2 (Supersonic Cruise)	2.1	40,000	27,000
4 (Max Speed)	3.0	60,000	13,475
5 (SLS)	0	0	21,700

1.2 RFP Response

The presented engine, BFTJ-56 (referred to as "BFTJ") is a turboramjet. Before deciding on a cycle, 4 different engine architectures and over 90 engine cycles were studied. In order to lower SFC, a high-bypass turbofan architecture was studied. After several engine tests, it was concluded that the thrust requirements for Supercruise and Mach 3.0 were unachievable by any high-bypass engine without exceeding the max diameter constraint. An afterburning low-bypass turbofan was studied in hopes of increasing thrust and maintaining low SFC. Over 30 LBTF engine cycles were studied, but all diameters exceeded the nacelle limit.

A promising solution was an afterburning 2-spool turbojet. Over 40 engine cycles were studied and most met thrust and SFC requirements. However, they all encountered operability challenges at Mach 3.0. With the use of GasTurb, it was concluded that the LPC of a turbojet would surge due to the natural ram compression that occurs at Mach 3.0.

This led to the conclusion that a two-cycle engine would be needed. The SR-71 powerplant (PW-J58) was studied because of its architecture and cruise conditions. The SR-71 cruised at Mach 3.2 and used only a ramjet as its source for thrust at those speeds. At lower Mach numbers, the ramjet bypass duct was closed and only the turbojet engine would operate. **Figure 1** shows the operation of the PW-J58 at its flight conditions.

A similar approach was used for the BFTJ. From take-off until supercruise, the turbojet would be used with the bypass doors closed. When flying at Mach 3.0, the bypass doors will open, and the front of the turbojet will be closed allowing all of the mass flow to enter the bypass duct. The air will bypass the turbojet in a diffuser to decelerate the flow before coming in contact with the flame holder of the ramjet. To finalize the turbojet and ramjet cycles, a sensitivity analysis using on and off-design parametric cycle analysis was completed. This proposed engine cycle produces all thrust

required at every flight condition while achieving competitive TSFC values of commercial jets in use today. A list of candidate engines was developed and can be found in **Table 64** in Appendix E.

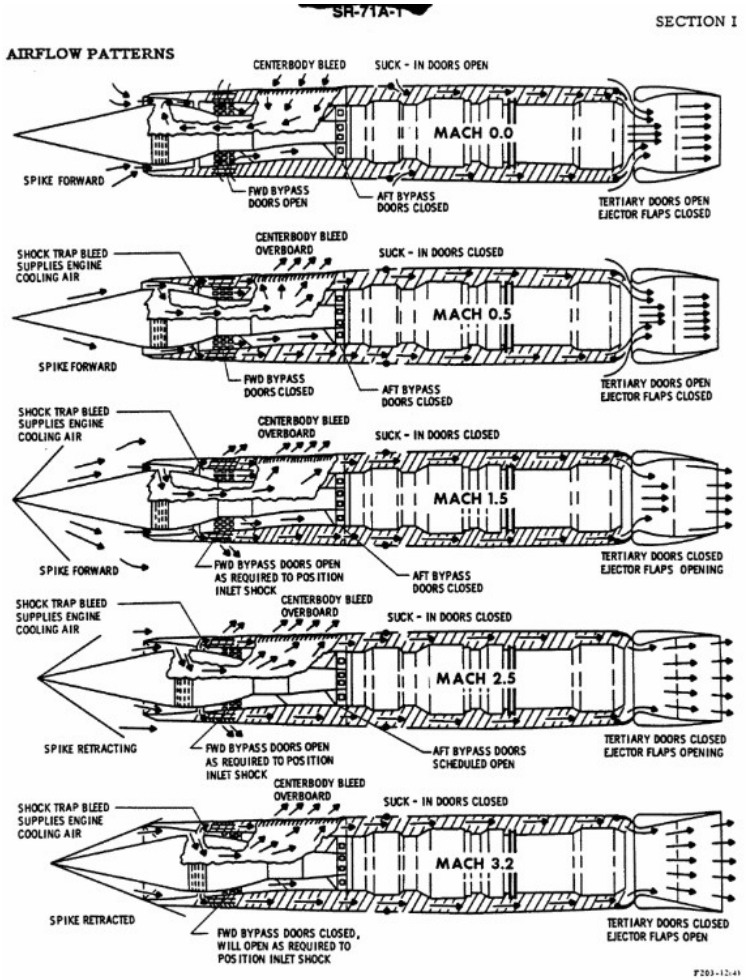

Figure 1: SR-71 inlet operation

1.3 Engine Cycle

The BFTJ cycle will be compared to the baseline engine. The preliminary analysis will outline both benefits and drawbacks of using the proposed engine cycle versus the baseline engine. **Table 5** lists the Figures of Merits (FOM) used throughout the analysis, which are based on a technology level appropriate for the entry into service date.

Table 5 : Figures of Merits (Technology Level 5) [8]

η_b	η_{AB}	η_{mPH}	η_{mL}	e_f	e_{cL}	e_{cH}	e_{tL}	e_{tH}	π_b	π_{AB}	π_D	π_n
0.999	0.995	0.98	0.996	0.92	0.91	0.91	0.9	0.91	0.96	0.98	0.995	0.98

1.3.1. RFP Baseline Cycle

The process of identifying the most ideal cycle for this mission requires the need of a baseline cycle to compare performance. **Table 6** outlines the major design parameters of the baseline engine cycle provided by the RFP.

Table 6: AIAA Baseline Engine Cycle

BPR	OPR	Outer FPR	Inner FPR	IPC PR	TIT	$\dot{m}_0$	M_0	Alt [km]
1.7	21	2	1.8	2.8	2492 [°R]	479 [$lb_m\ s^{-1}$]	0	0

The RFP provided a GasTurb performance output file at Sea Level Static (SLS) conditions. It was recommended to iteratively find the design reference point for the presented engine. Given a GasTurb input file for the baseline engine (with no reference conditions), the cycle was modeled in GasTurb and it was determined that the reference conditions used were at SLS. All input and output files comparing the baseline engine with the design team's model can be found in Appendix E which confirms the baseline engine was modeled accurately in GasTurb.

The off-design performance of the baseline engine was analyzed for the required flight conditions. The final off-design comparison of the baseline engine and the BFTJ are shown in **Table 9**.

1.3.2. BFTJ-56 Proposed Cycle

The cycle for the BFTJ is shown in **Table 7** and **Table 8** for the turbojet and ramjet, respectively. The TIT selected for this turbojet cycle was 3700 [°R], keeping in mind material technology advancements of Ceramic Matrix Composites (CMC) and Carbon-Carbon Composites (C-CC) that allow for TIT "as high as 3460 and 4460 [°R]" [13]. Although higher temperatures showed to increase specific thrust and decrease engine size, an upper limit on TIT was found where TSFC began to increase.

Table 7: BFTJ, turbojet cycle

OPR	FPR	TIT_{max}	$\dot{m}_0$	M_0	Alt [ft]
20	3.4	3700 [°R]	203.9 [$lb_m\ s^{-1}$]	1.6	40,000

Table 8: BFTJ, ramjet cycle

P_{t2}/P_{t1}	$\dot{m}_0$	T_{t7}	M_0	Alt [ft]
0.728	154.3 [$lb_m\ s^{-1}$]	3900 [°R]	3.0	60,000

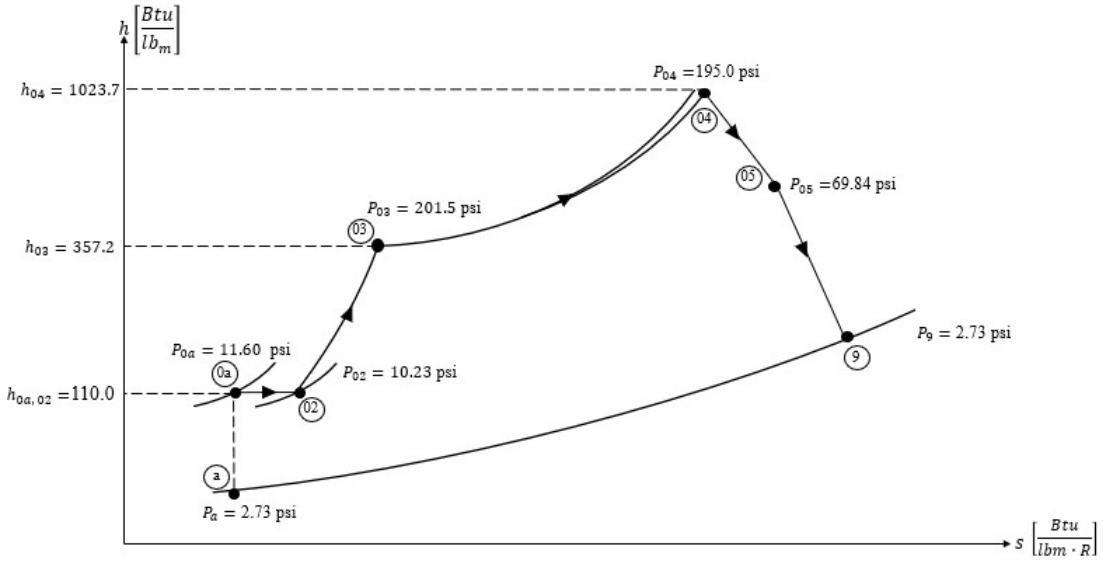

Figure 2: Brayton cycle for the BFTJ-56, turbojet operation

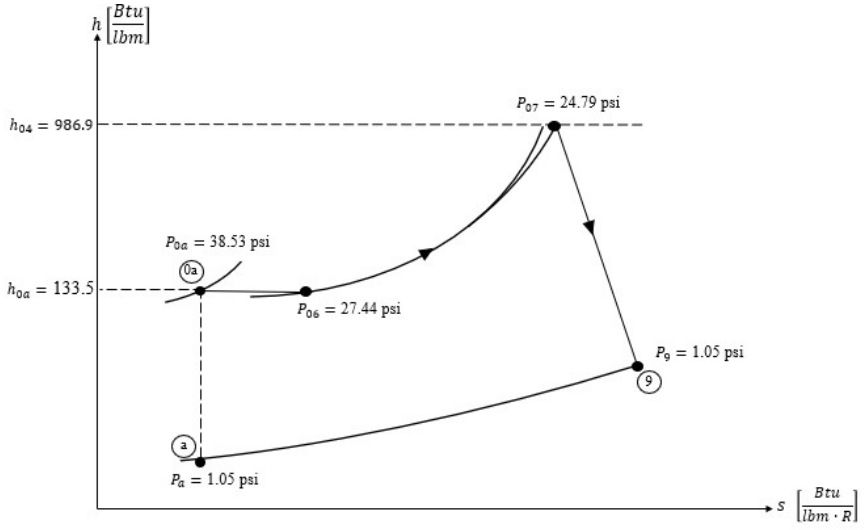

Figure 3: Brayton cycle for the BFTJ-56, ramjet operation

1.3.1 Benefits and Drawbacks

The BFTJ yields a compromise in both fuel savings and engine size. A turbofan, regardless of bypass ratio, will be more fuel efficient than a turbojet at lower speeds. The tradeoff for an increase in fuel efficiency is a decrease in specific thrust and the need for a larger overall engine. **Figure 4** illustrates the trends found of specific thrust ($F/\dot{m}$) and TSFC with a variation of bypass ratio at the reference point. These curves were used as a guide to determine to optimal bypass ratio for the proposed engine.

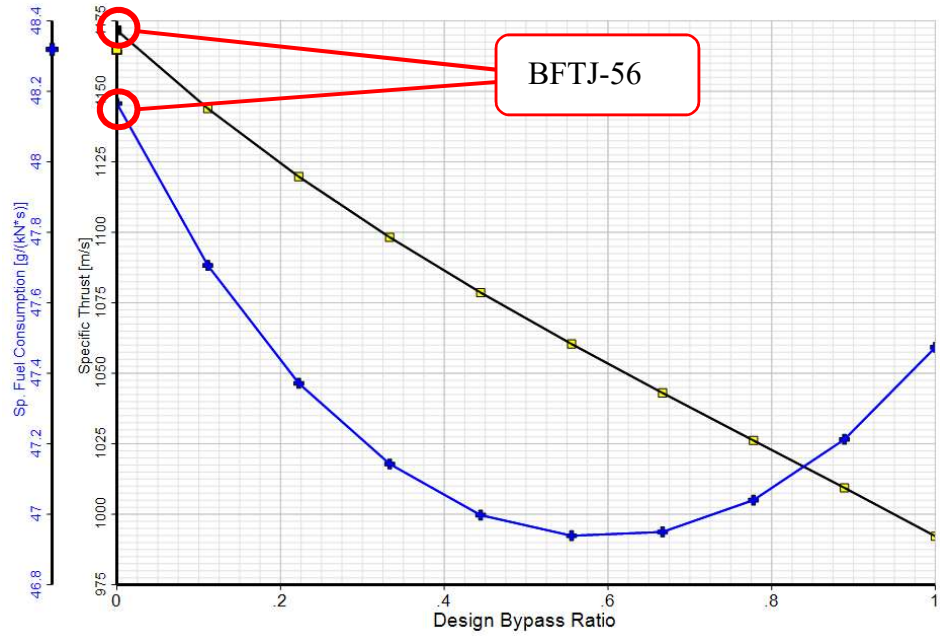

Figure 4: Specific Thrust and SFC vs Bypass Ratio

Figure 5 and **Figure 6** display trends with specific thrust and TSFC through variation of α and TIT. The goal is to find a compromise between TSFC and specific thrust to meet the needs for required thrust while maintaining a lower TSFC. The design point of the BFTJ is circled on **Figure 5** and **Figure 6** in red. **Figure 6** suggests that, for a given bypass ratio, an increase in TIT yields an increase in thrust. The figure also suggests that the TSFC, for a given bypass ratio, decreases with an increasing TIT.

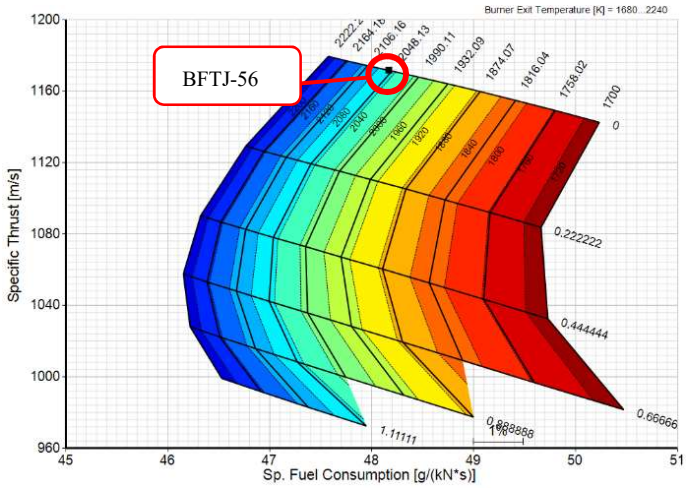

Figure 5: Carpet plot of TSFC and specific thrust through variation of TIT and α

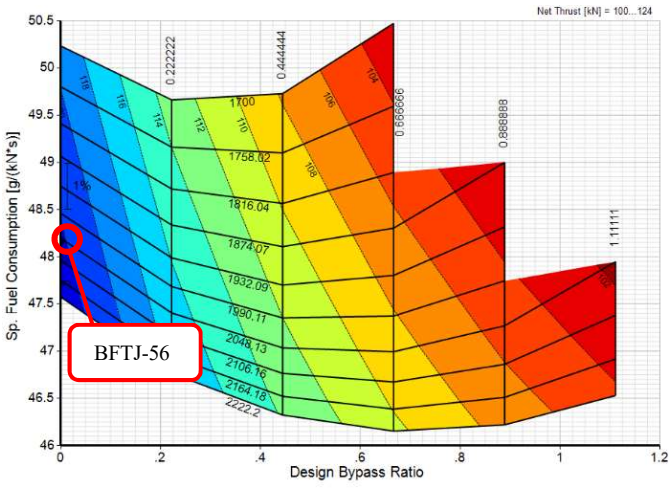

Figure 6: Carpet plot of TSFC and α through variation of Net Thrust and TIT

The TSFC for a turbojet is higher than that of a turbofan. However, the TSFC of the BFTJ is much less than that of the baseline engine at supercruise. The reason for this is the difference of design points for each engine. The baseline engine is designed to perform best at subsonic speeds, where the BFTJ is optimized for ***both*** the subsonic and supersonic cruise conditions.

1.3.2 Turbine Inlet Temperature (TIT)

The performance at Mach 2.1 is predicated upon the high TIT. The choice of selecting a TIT of 3700 [°R] poses additional considerations for maintenance and production costs. Today's turbine engines in service operate at a maximum TIT of about 3200 [°R] [8]. This operational temperature limit is related to the current materials technology capable of withstanding the thermal stresses. Because the BFTJ will enter service in 2030, the advancement of materials technology and manufacturing is considered in the preliminary analysis. It is assumed that future developments in CMCs and C-CC's will provide a sufficient life cycle for the turbine components.

Data is presented from Gerald Knip, Jr. of NASA's Lewis Research Center who conducted an analysis on advanced turbofans incorporating revolutionary materials [13]. **Figure 8** estimated that by 2010, CMCs in turbine vanes could withstand an operating temperature of ~3500 [°R], while C-CCs could withstand above 4000 [°R]. Similarly, **Figure 12** shows the same materials used in turbine blades. The application of these materials will eliminate the need for coolant flow for the turbine. However, TBCs were considered in the turbine design to alleviate thermal stresses.

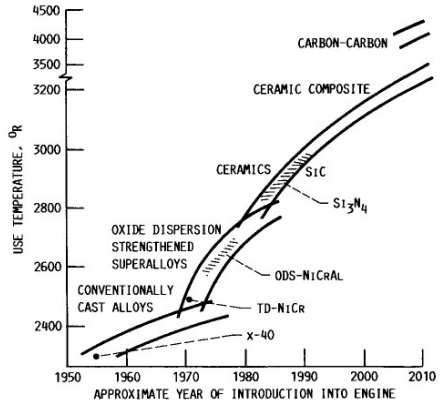

Figure 8: Temperature trends of turbine vane materials [13]

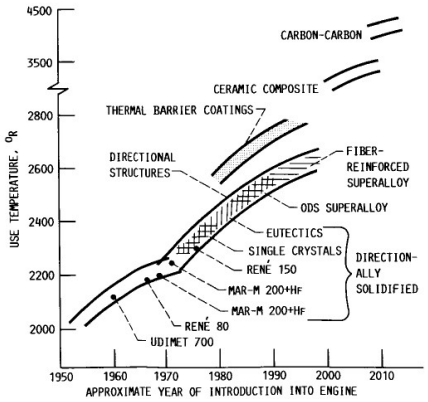

Figure 7: Temperature trends of turbine blade materials [13]

1.4 Engine Performance and Operability

The overall performance of the BFTJ is compared to the baseline engine, shown in **Table 9**. The thrust values shown are compared to the required thrust. Since there are no explicit TSFC requirements, the TSFC of each engine is compared to one another. Additionally, the BFTJ shows that it does not require max TIT to meet thrust requirements, except for max speed condition. Therefore, TIT was reduced to decrease TSFC. The percentages shown for TIT are relative to each engine's max TIT.

Table 9: Propulsion System Performance Comparison

	Required	Baseline		BFTJ-56	
T (Mach 3) * [lb_f]	13475	Inoperable		14052.2*	**+4.28%**
TSFC (Mach 3) * [1/hr]	-			2.032*	
T (Supercruise) [lb_f]	27000	**3967.9**	**-85.3%**	27819.3	**+3.03%**
TIT (Supercruise) [°R]	-	2492 (Max)		3613	-2.35%
TSFC (Supercruise) [1/hr]	-	1.655		**1.3658**	
T (BCA) [lb_f]	10675	**5692.1**	**-46.7%**	10978.8	**+2.85%**
TIT (BCA) [°R]	-	2492 (Max)	0.0%	2989	**-19.2%**
TSFC (BCA) [1/hr]	-	0.8123		1.144	
T (Subcruise) [lbf]	5050	5373.7	6.40%	5212.4	**+3.20%**
TIT (Subcruise) [°R]	-	2492 (Max)	0.00%	2332	**-36.90%**
TSFC (Subcruise) [1/hr]	-	0.7706		1.082	
T_{SLS} [lb_f]	21700	21700	0.0%	22616.1	**+4.22%**
TIT (Take-Off) [°R]	-	2492 (Max)	0.0%	2682	**-27.5%**

* Ramjet operation

Critical to the performance of the BFTJ is the operation of the turbomachinery. **Table 10** shows the surge margins predicted by GasTurb for the LPC and HPC. **Table 11** shows the spool speeds w.r.t the design RPM for the LPC, HPC, HPT and LPT at all flight conditions. There is no data for Mach 3.0 due to the operation of the ramjet.

Table 10: LPC and HPC surge margins off-design

Flight Condition	SLS	Subcruise	BCA	Supercruise
LPC	36.2%	22.4%	48.8%	35.64
HPC	38.9%	42.6%	26.9%	39.892

Table 11: Off-design spool speed w.r.t to design RPM

Flight Condition	SLS	Subcruise	BCA	Supercruise
LPC	86.4%	80.6%	97.0%	83.4%
HPC	98.2%	89.3%	97.0%	92.3%
HPT	99.2%	96.5%	98.3%	100%
LPT	95.7%	90.7%	99.0%	94.2%

The following figures show the compressor maps for the LPC and HPC for the subsonic cruise and supercruise.

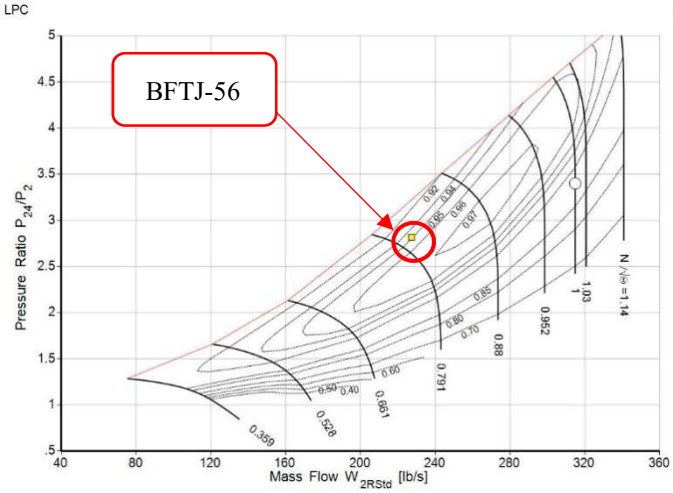

Figure 10: LPC operating point for subsonic cruise

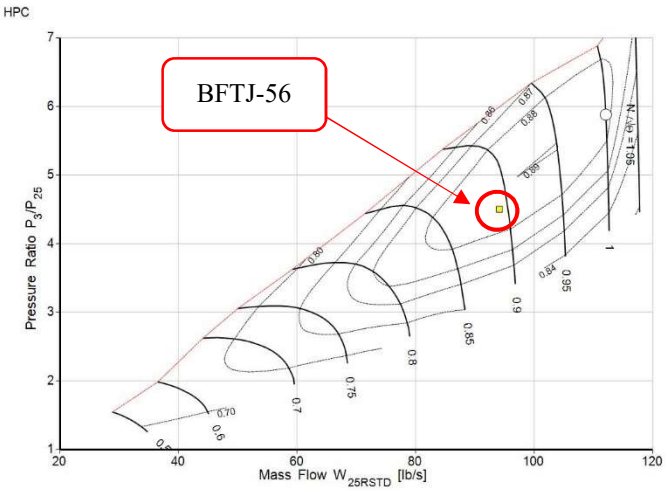

Figure 9: HPC operating point for subsonic cruise

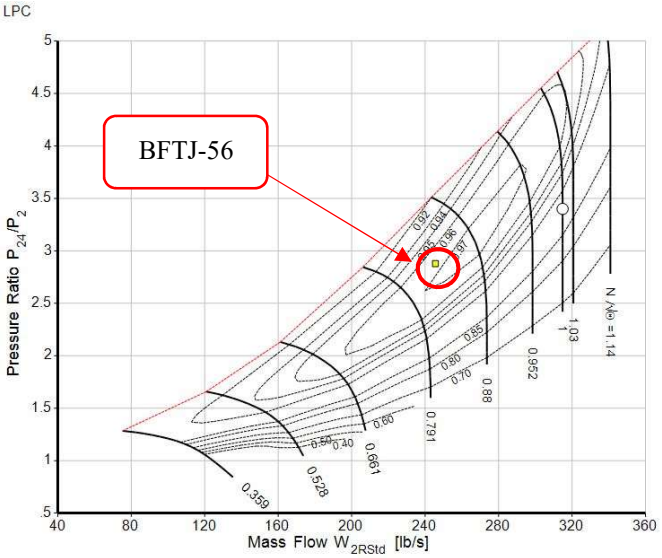

Figure 12: LPC operating point for supercruise

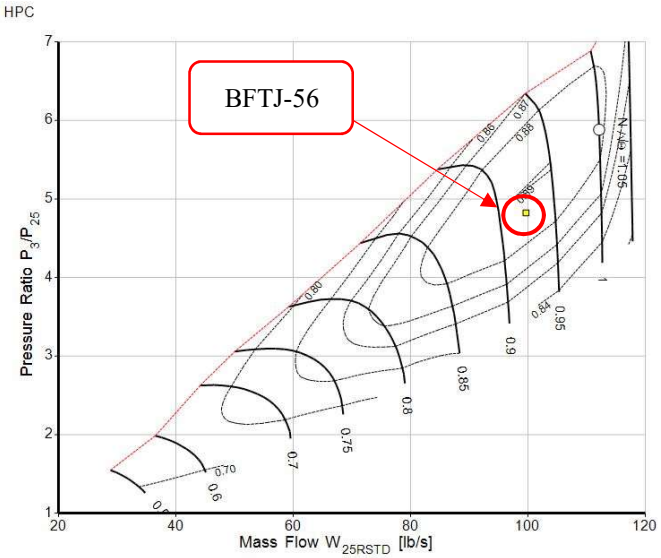

Figure 11: HPC operating point for supercruise

2 Inlet Design

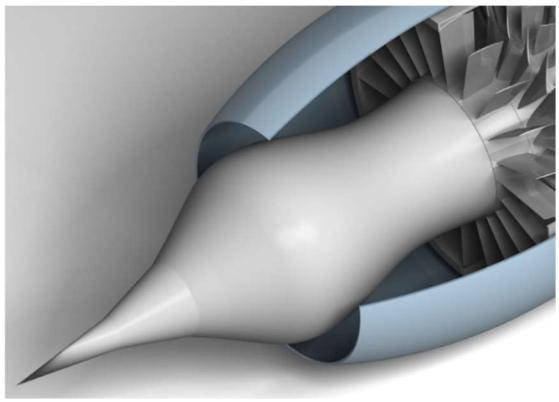

Figure 13: Inlet isometric view

The inlet is designed to maximize the total pressure recovery at each flight condition while delivering a healthy Mach number to the LPC entrance. Given the wide range of required flight conditions, a middle ground was settled upon for the design. The middle ground design yielded desirable off-design performance. Additionally, variable geometry is incorporated into the design to adjust the inlet throat area and to redirect the flow for ramjet operation. The meridional view of the design point of the inlet is displayed in **Figure 14**. The on-design length of the inlet, to the entrance of the LPC is 5.71 [ft]. The extension mechanism of the spike is locked back to allow for the designed mass flow to enter the engine. The extension is used to control the throat inlet and the amount of mass flow allowed in during different operating conditions. The maximum extension is 9.14 [in] during ramjet operation at Mach 3.

Table 12: Inlet on-design parameters

M_0	Alt [ft]	π_d	M_{LPC}	$\dot{m}_0$ [lbm/s]	Length [ft]
1.6	40,000	0.8825	0.61	92.5	5.71

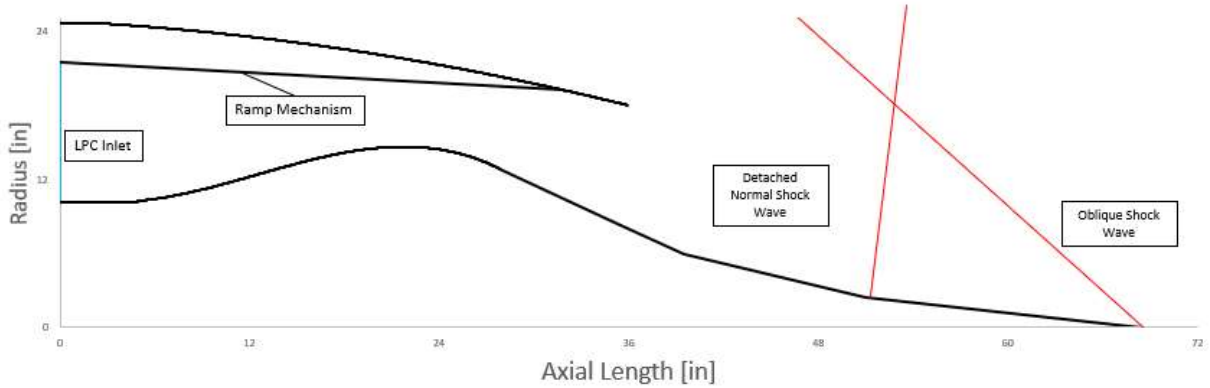

Figure 14: Design point meridional view of inlet

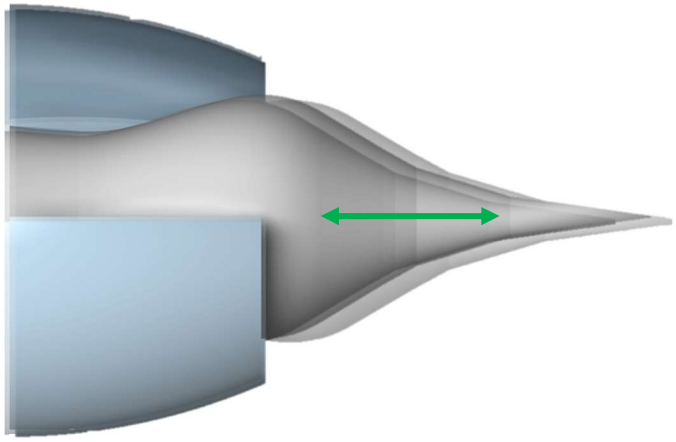

Figure 15: Inlet motion for varying flight conditions

2.1 Supersonic Diffuser

The centerpiece of the inlet is designed to provide an external compression to the incoming flow. The flow analysis of the cone is approximated by treating the 3D cone as a 2D ramp. For a given oblique shock angle, flow analysis over a 3D cone would yield ramp angles that are slightly larger than that using a 2D ramp. The external compression of the flow is analyzed through shock wave analysis. The geometry of the cone is in **Figure 16** and **Table 13.**

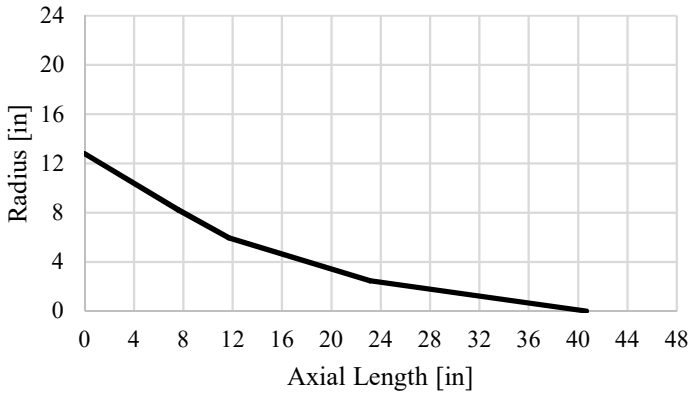

Table 13: Centerpiece Geometry

Ramp	θ [°]	Axial Length [in]
1 (Tip)	8	17.549
2	9	11.449
3	12	4.090
4	2	7.590

Figure 16: Inlet centerpiece

The angles of the ramps are designed to have shock waves detach at a specific location for each operation condition. **Table 14** summarizes the shock detachment location for each supersonic operating condition. According to NASA, detached shocks behave like normal shocks and would be able to decelerate the supersonic flow to a manageable magnitude for the subsonic diffuser. The entry Mach number for the subsonic diffuser is an important parameter for the overall performance and length of the diffuser.

Table 14: Location of shock detachment

Mach Number	Shock Detachment Location	Mach Number Entering Subsonic Diffuser
1.6	Ramp 2	0.776
2.1	Ramp 3	0.704
1.15	Ramp 1 (Tip)	0.875
3	No Detached Shocks	0.643

2.2 Subsonic Diffuser

The subsonic diffuser further decelerates the flow to the design Mach number for the LPC. The geometry and performance for design point of the subsonic diffuser are summarized in **Table 15** The length of the diffuser is determined using empirical data that relates the area ratio, length, coefficient of pressure, and difference of tip and hub radii at the throat. **Figure 8** displays the design point extrapolated from the performance chart [9].

Table 15: Subsonic diffuser design parameters

M_t	**0.776**
π_{dmax}	0.91
M_{LPC}	0.610
c_p	0.128
A_t [ft^2]	6.023
A_{LPC} [ft^2]	7.464
AR - 1	0.233
L [in]	35.9

The value $L/\Delta R$ is retrieved from the figure and, with a given ΔR, the length of the diffuser is computed.

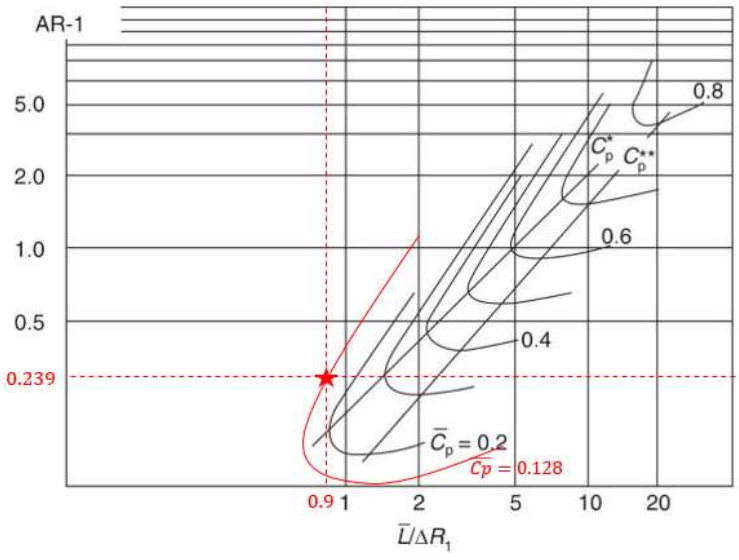

Figure 17: Diffuser performance chart

2.2.1 **Performance and Variable Geometry**

Table 16 tabulates the performance of the inlet at all major operating points. Listed is the inlet pressure ratio (π_D), required mass flow, and exit Mach number. The inlet pressure ratios are used for on and off-design performance cycle analysis.

Table 16: Summary of inlet performance at major operating points

Flight Condition	Supersonic Diffuser π	Subsonic Diffuser π	Inlet PR (π_D)	$\dot{m}_0$ [lbm/s]	M_{EXIT}
M = 0.98	1.0000	0.91	0.9100	74.1	0.662
M = 1.15	0.9967	0.91	0.9070	118.1	0.743
M = 1.6	0.9698	0.91	0.8825	203.9	0.610
M = 2.1	0.9146	0.91	0.8323	290.9	0.408
M = 3.0	0.7997	0.91	0.7277	154.3	0.447

The inlet centerpiece is designed to move axially to adjust the throat area. The adjustment of the throat area affects the magnitude of the incoming mass flow and subsonic diffuser performance. Summarized in **Table 17** is the required centerpiece extension and all diffuser performance parameters.

Table 17: Summary of inlet performance at major operating points

Flight Condition	$\dot{m}_0$ [lbm/s]	A_t [ft^2]	AR - 1	c_p	$L/\Delta R$	Spike Extension [in]
M = 1.6	203.9	6.023	0.239	0.128	0.90	0
M = 2.1	290.9	4.918	0.510	0.332	3.55	2.379
M = 0.98	74.1	4.129	0.798	0.378	4.71	4.241
M = 1.15	118.1	5.610	0.324	0.371	3.12	0.866
M = 3.0*	154.3	2.468	0.400	0.164	2.20	9.139

* Ramjet designed with different subsonic diffuser located in bypass duct

The performance of the subsonic diffuser can be plotted on the subsonic diffuser performance chart seen earlier in **Figure 17**. This approximation indicates that the inlet will behave at all operating conditions and yields a minimal risk for flow separation.

2.3 Ramjet Operation

Operating conditions at Mach 3.0 will require the transition from a turbojet to a ramjet. This is accomplished by opening the bypass duct and closing entry to the core with a moveable flap. **Figure 18** illustrates the inlet with an open bypass and closed core. Additionally, the centerpiece is required to shift forward 9.14 [in] at Mach 3 to allow in the required mass flow.

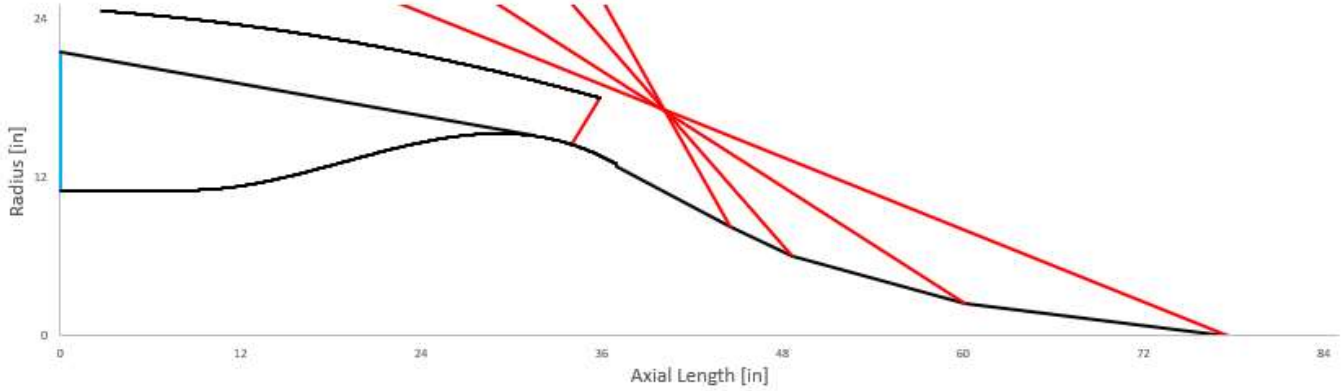

Figure 18: Inlet meridional view during ramjet operation at Mach 3.0

3 Compressor Design (LPC and HPC)

The OPR of 20 was achieved for the entire compression system. The LPC was designed to achieve a π_{cL} of 3.4 in 3 stages. The HPC was design for a π_{cH} of 5.88 in 5 stages. An inter-compressor duct was necessary due to compressor architecture. The largest fan diameter is 44.6 [in.] at the LPC 1st stage and has an axial length of 55.1 [in.]. An IGV imparts swirl to the flow before entering the LPC and HPC to preserve off-design engine performance.

Figure 19: Compressor isometric view

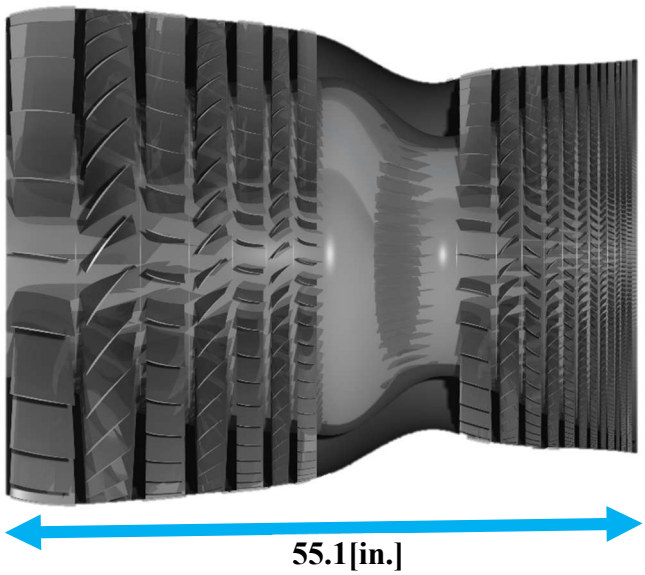

Figure 20: Compressor right side view

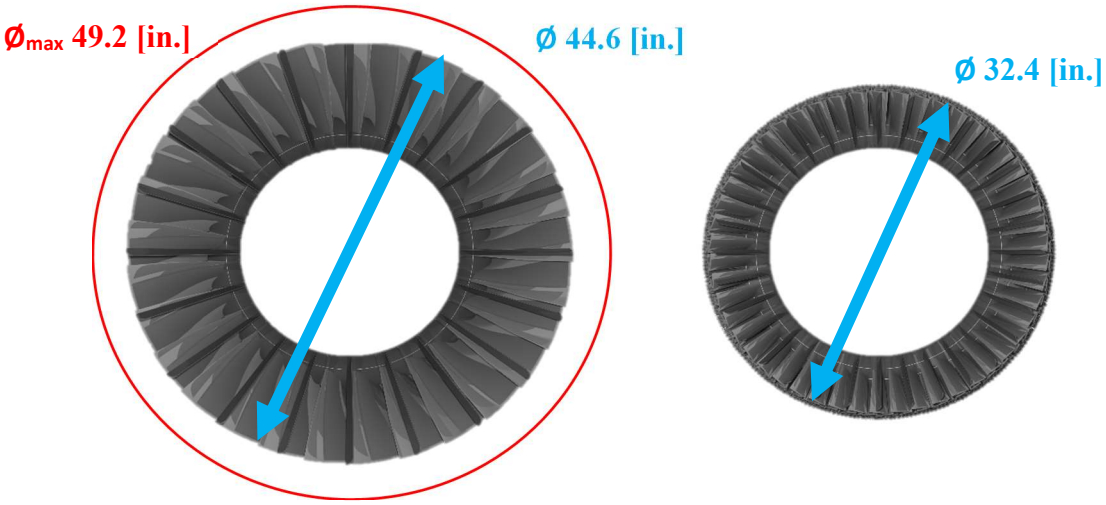

LPC Front View **HPC Front View**

3.1.1 **Design Criteria**

All criteria are explained in the following sections. It must also be noted that due to an entry into service date of 2030, assumptions on technology advancements were made with documented precaution. Some of the assumptions lie in the stage health assessments and noise emissions due to supersonic flow in the compressor.

3.1.1.1 Inlet Guide Vane (IGV)

The highly loaded design of the fan led to supersonic circumferential tip speeds. An IGV was placed to impart positive swirl onto the flow in effort to reduce the rotor relative tip speed (W_1 and $M_{tip,r1}$). The swirl is directly controlled by the selection of α_1 and M_1.

3.1.1.2 H/T, Flow Coefficient, and Spool Speed

In the preliminary stages of design, the constraints led to high flow speeds at the tip of the LPC and large flow areas. At first, low ϕ (~0.4-0.6) and low H/T (~0.4-0.75) were experimented with and selected at the 1st stage of each component only. The lower ϕ were selected to reach higher spool speeds and effectively decrease the axial length of the compressors, however, this led to high $M_{r,tip}$ and $M_{U,tip}$. Due to flow coefficient being a direct ratio of these Mach numbers, the H/T selection was crucial in mitigating these issues. As described by Farokhi [9]:

$$\phi = \frac{M_Z}{M_T} = \frac{V_{ax}}{U} \tag{1}$$

During the preliminary design, it was found that lower H/T, although led to smaller tip radii, also led to increases in flow speeds. The higher H/T led to a reduction in flow speeds, but at the cost of a larger area at the fan entrance and much higher H/T in later stages. A design with higher H/T led to difficulties when matching the LPC and HPC components. The final selections were made with small tip radii and manageable flow speeds in mind.

3.1.1.3 Degree of Reaction

The Degree of Reaction (°R) is calculated at hub, mid, and tip-span locations. However, for the compressors, only the °R at the mid is of importance. A perfectly balanced compressor stage will have a °R of 50% at the mid-span. Paraphrasing Farokhi, rotors have shown to have boundary layers that are more resistant to adverse pressure gradients than stators. Therefore, "a degree of reaction of 60% may be a desirable split between the two blade rows in a compressor stage." [Farokhi, 9] The relationships used to calculate the °R for the compressors are as follows:

$$°R = \frac{\frac{1}{2}W_1^2 - \frac{1}{2}W_2^2}{\left(\frac{1}{2}W_1^2 - \frac{1}{2}W_2^2\right) + \left(\frac{1}{2}V_2^2 - \frac{1}{2}V_1^2\right)} \tag{2}$$

3.1.1.4 Stage Loading

The stage loading (λ) is used in the design to determine how hard each stage is working relative to double the kinetic energy for the blade. By definition, λ is calculated by relating Δh_0 and the tangential velocity as follows:

$$\lambda = \frac{\Delta h_0}{2 * \frac{1}{2} U^2} = \frac{\Delta h_0}{U^2} \tag{3}$$

Historically, λ for each compressor stage should continuously decrease, yet not plateau. Additionally, low values of λ indicate that a stage is not working as hard, therefore, the work addition from the stage is not as significant as that from the previous stages. This is a strong indication that the final stage of the design could be eliminated. Both LPC and HPC designs experienced low λ values during the preliminary stages of design and this led to the elimination of a single stage in both components.

3.1.2 Health Assessment

3.1.2.1 DeHaller Number

The health of each stage was critical to the design process as off-design performance will play a large role to the success of the powerplant. The wide range of flight conditions will put the engine through many scenarios that will push it to its limits. For this reason, the LPC and HPC were designed with a conservative approach w.r.t flow speeds, but an aggressive one w.r.t architecture.

The DH were calculated at all radial stations. The DH for rotor and stator are defined as follow:

$$DH_R = \frac{W_2}{W_1} \tag{4}$$

$$DH_S = \frac{V_3}{V_2} \tag{5}$$

The criteria for the DH was, DH > 0.68. This criterion will ensure that rotors and stators are decelerating their relative flows at a reasonable pace so that flow separation will not occur.

3.1.2.2 Lieblein Diffusion Factor

An indication of flow separation can be represented by the average DF at every span location. The DFs for rotor and stator are found using the equations below:

$$DF_R = 1 - DH_R + \frac{\Delta W_U}{2W_1\sigma} \tag{6}$$

$$DF_S = 1 - DH_S + \frac{\Delta V_U}{2V_2\sigma} \tag{7}$$

The original criteria for this design was to limit DF to 0.45 at the design point to reduce the tendency of boundary layer stall. However, research into this topic led to the increase of this criteria. According to Farokhi, "Hence, the maximum diffusion factor associated with well-behaved boundary layer on these classical blade profiles is Dmax ~ 0.6. A higher D-factor (of ~ 0.7) may be achieved in cascades of modern controlled-diffusion profiles."[Farokhi, 9] The findings of D_{max} are based on historical data based on experiments conducted by Seymour Lieblein in 1965, shown in Figure 21 [Lieblein, 4]. His experiments are based on measuring the wake profiles of cascades with classical blades and their correlation with D_{max}.

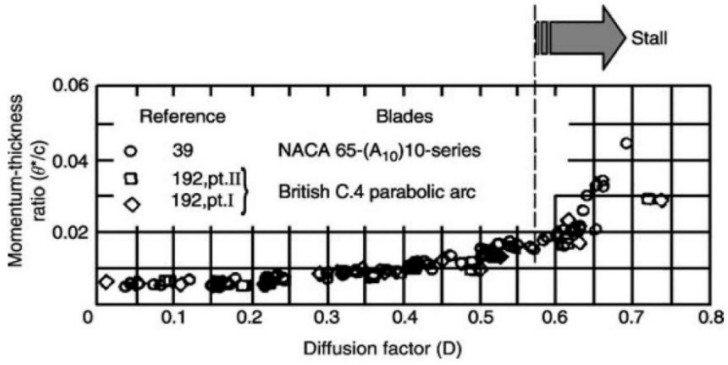

Figure 21: Correlation of DF and wake momentum deficit thickness. [4]

Although Lieblein and Farokhi explain that a DF of 0.7 is achievable, two major assumptions would be needed: the use of NACA 65-series airfoils and use CFD for verification. For this reason, the design team chose a conservative limit of 0.6 throughout the LPC and HPC.

3.1.3 Summary of Design Criteria

Table 18 shows all design criteria for the LPC and HPC.

Table 18: Summary of design criteria used in LPC and HPC designs

Parameter	Range	Parameter	Range
Flow Coefficient (ϕ)	[0.4 – 0.7]	All Exit Mach	≤ 0.9
Stage Loading (λ)	[0.2 – 0.55]	Δα / Δβ	≤ 45°
Degree of Reaction (°R)	[0.1 – 0.9]	α / β	≤ 68°
Lieblein Diffusion Factor	≤ 0.6	H/T	[0.3 – 0.98]
DeHaller Criterion	≥ 0.68	Aspect Ratio	[1.8 – 4]
Tip Tangential Mach Number	[1.0 – 1.5]	Taper Ratio	[0.8 – 1.0]
Tip Relative Mach Number	≤ 1.4		

3.2 LPC Design

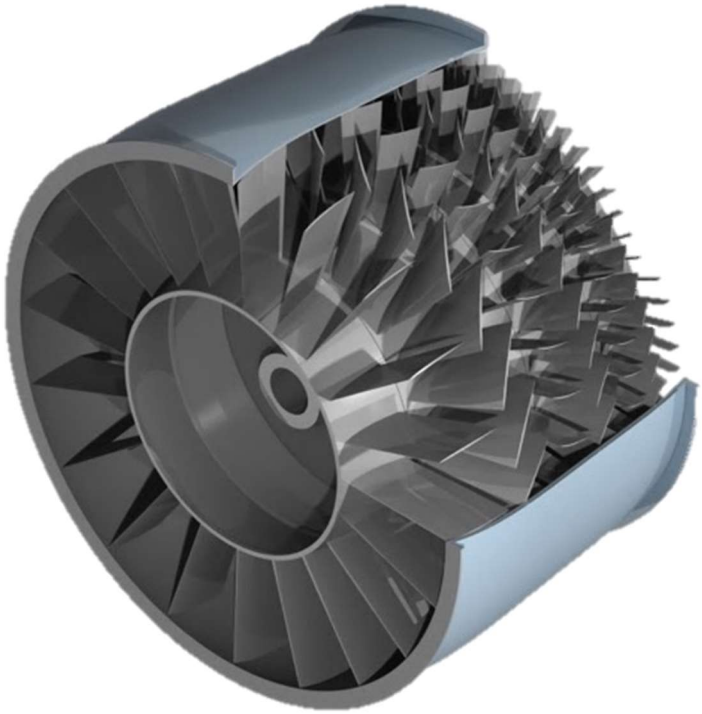

Figure 22: LPC isometric view

3.2.1 Design Choices

Table 19: Design choice summary for LPC

Parameter	$\dot{m}$	H/T	ϕ	RPM	α_1	M_1
	203.9 [lb_m/s]	0.55	0.635	6945	9°	0.61

The main factors were overall engine diameter, compressor axial length, aerodynamic health assessment, and noise emissions. **Table 19** shows the design choices made.

3.2.1.1 Total Pressure Distribution

Minimal changes in $\Delta P_{0,stg}$ were found favorable for the future designs of seals between stages. The preliminary design was attempted with lower π_{stg}, but across 4 stages. The result was a low λ for the 4th stage which led to elimination of a stage. The change from 4 stages to 3 stages in the LPC increased the first stage PR to 1.704. As expected, this led to higher, but satisfactory λ and $°R$ for the remaining stages.

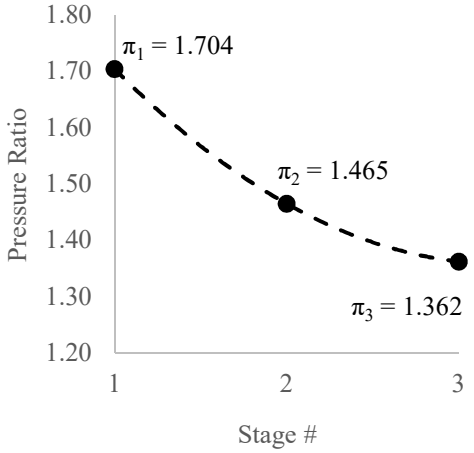

Figure 23: LPC pressure distribution

3.2.1.2 Adiabatic Efficiency

The adiabatic efficiencies for each stage were selected in comparison with empirical data that relates efficiencies with π_{stg}. This data was provided by an engineer with design experience. **Figure 24** shows the adiabatic total-to-total efficiency distribution.

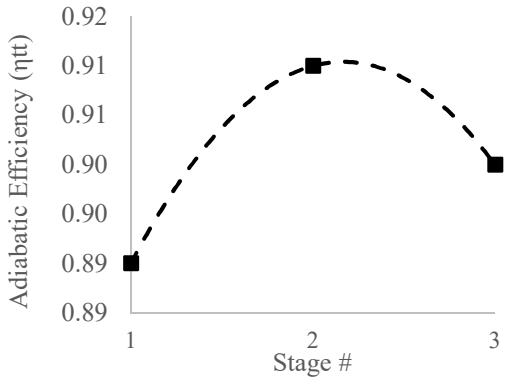

Figure 24: LPC adiabatic efficiency distribution

3.2.2 Geometry

3.2.2.1 Meridional view

Figure 25 shows the meridional view of the LPC in a 1:1 scale.

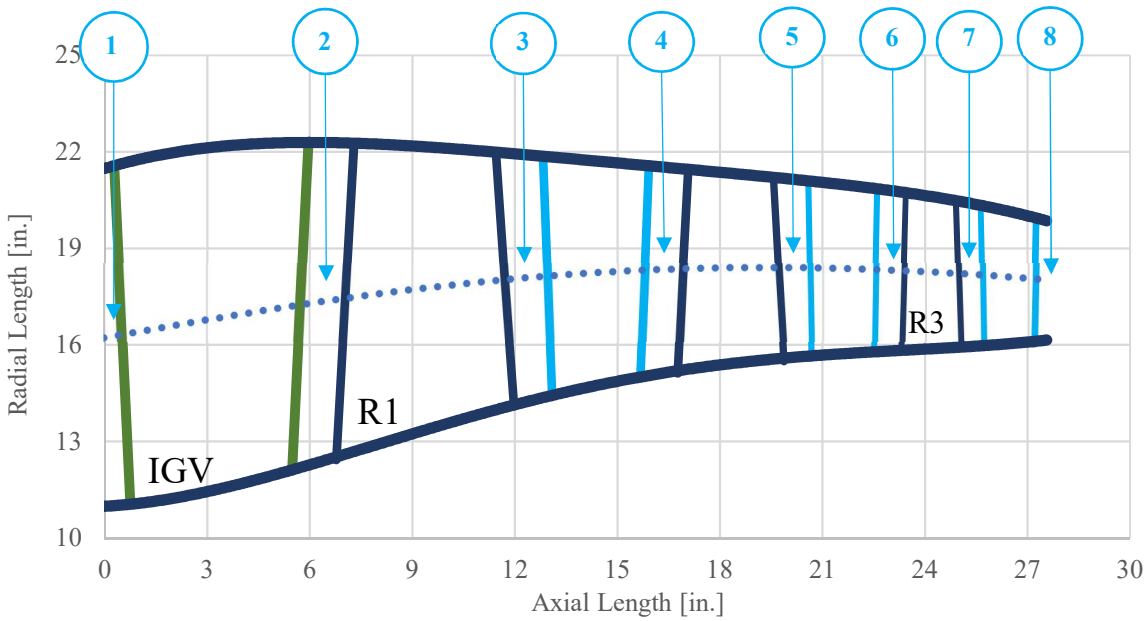

Figure 25: Meridional view of LPC and IGV

3.2.2.2 Number of blades, Solidity, and Pitch

The IGV and fist rotor have the largest blades, and therefore have fewer blades. Finding the final NOB and pitch is calculated through an iterative process, affected by solidity. Pitch and solidity are then recalculated with the new NOB. To clarify, not all calculations for NOB, solidity, and pitch were done at the same span location. Solidity for rotors were chosen at either the mid or tip span locations. The criteria for this selection are based on the flow speed entering the rotor. The following logic was implemented: if the relative flow entering the rotor is subsonic, then solidity would be chosen as 1.0 at the mid-span. However, if any relative flow entering the rotor is supersonic, then solidity would be chosen as follows:

$$\sigma = (M_{rel})_{max} + 0.1 \tag{8}$$

Table 20 summarizes all NOB, σ, and S at the relative span location of importance.

Table 20: NOB, σ, and S for stages in LPC

Stage #	IGV			Rotors			Stators		
	NOB	σ_{mid}	S [in]	NOB	σ_{tip}	S_{tip} [in]	NOB	σ_{mid}	S_{mid} [in]
1	20	1.0	5.1	27	1.36	6.7	34	1.0	3.3
2	-	-	-	40	1.12	3.4	50	1.0	2.3
3	-	-	-	56	0.815*	2.0*	66	1.0	1.7

*Solidity and pitch chosen at mid-span due to subsonic Mach entering rotor

3.2.2.3 Airfoil Geometry

The airfoil geometry is finalized using Aspect Ratio (AR), Taper Ratio (TR), and calculated values of span (b_{avg}), chord (C), axial chord (C_{ax}), and stagger (σ_s). **Table 21** below shows all AR and TR selected for every blade in the LPC, including the IGV.

Table 21: Aspect ratio and taper ratio selections for each blade

Stage #	IGV		Rotors		Stators	
	AR	TR	AR	TR	AR	TR
1	2.0	1.2	1.1	0.8	2.0	1.2
2	-	-	2.0	0.8	2.1	1.1
3	-	-	2.2	0.85	2.3	1.1

Absent CFD analysis to customize the channel shapes with radius, a TR was selected to produce reasonable airfoil shapes in meridional and 3D views. A selection was made based on observed shapes of engines in the ERAU Gas Turbine Lab and online. TR used is defined as follows:

Table 22: Blade span length (b_{avg})

Stage #	IGV [in]	Rotors [in]	Stators [in]
1	10.3	8.7	7.0
2	-	6.1	5.3
3	-	4.6	4.1

$$TR = \frac{C_{ax,t}}{C_{ax,h}} \tag{9}$$

The AR and TR selection allowed for the chords of each blade to be calculated with the use of b_{avg}. The b_{avg} values were calculated by averaging the heights of the intermediate stations between blades. **Table 22** shows all calculated b_{avg} values for each blade. With b_{avg} and C_{ax} calculated for each blade, the stagger angles from the aerodynamics of the stage is used to calculate the true chords of each blade, where:

$$\sigma_{s,R} = \frac{\beta_1 + \beta_2}{2} \tag{10}$$

$$\sigma_{s,S} = \frac{\alpha_2 + \alpha_3}{2} \tag{11}$$

Table 23 shows the aforementioned values at hub, mid, and tip-span locations for only the 1st stage of the LPC. The same values for the 2nd and 3rd stages can be found in Appendix A.

Table 23: Airfoil chords, axial chords, and stagger for LPC 1st stage

Span Location	IGV			Rotor 1			Stator 1		
	C [in]	C_{ax} [in]	σ_s [°]	C [in]	C_{ax} [in]	σ_s [°]	C [in]	C_{ax} [in]	σ_s [°]
Tip	5.7	5.7	3.5	7.1	4.1	54.1	3.5	3.1	29.3
Mid	5.2	5.2	4.5	6.3	4.7	41.7	3.4	2.8	33.5
Hub	4.7	4.7	6.3	5.5	5.2	19.9	3.3	2.6	38.8

3.2.3 Thermodynamics

The individual rotors provide adiabatic compression with work addition to the flow, while the stators provide adiabatic compression with no work. The rotors are analyzed in both the absolute and relative F.O.R, where the relative F.O.R shows the static enthalpy rise and the absolute F.O.R shows the total enthalpy rise. The stators are analyzed in the absolute F.O.R only. A model of constant Cp was used throughout the LPC due to the relative low temperature differences. As a simplification of radial equilibrium across the LPC, the Free Vortex Solution was applied.

3.2.3.1 Thermodynamic Property Variation

Shown in **Figure 26** are the total and static thermodynamic properties for the LPC, beginning with the entrance of the IGV. The adiabatic compression from the stators is visible in the figure below. It must be noted that there is a small total pressure loss through each stator, represented as $\zeta_{Stator} = 0.03$ in the design process. The station numbering can be referenced in **Figure 25**.

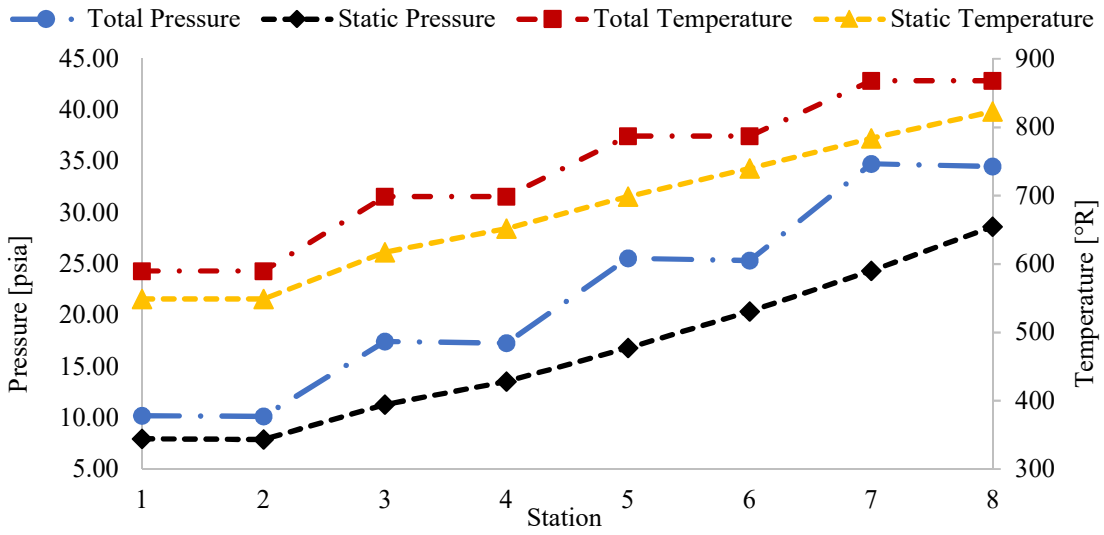

Figure 26: LPC thermodynamic property variation

3.2.3.2 h-s diagrams

The h-s diagram for the entire LPC is shown in **Figure 27**. All thermodynamic data for the LPC can be found in Appendix A.

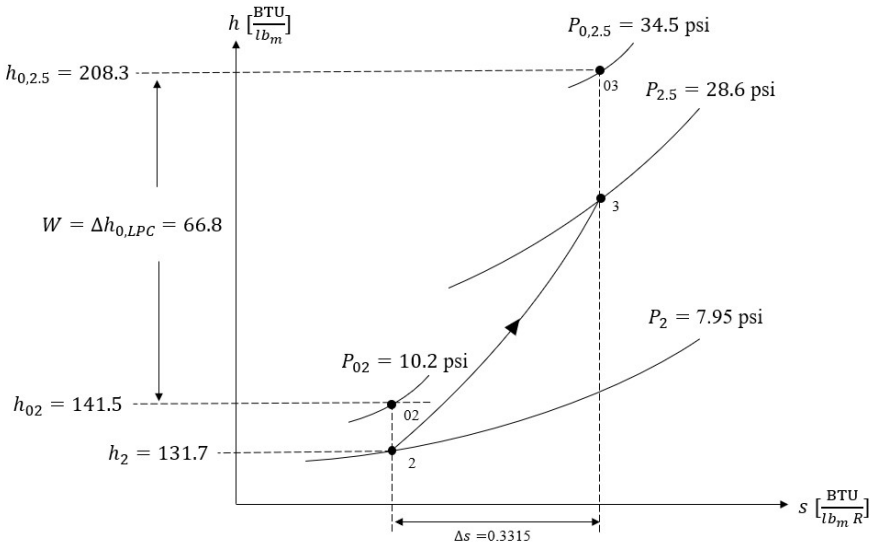

Figure 27: h-s diagram of LPC

3.2.4 Aerodynamics

3.2.4.1 Mach Number Variation

Controlling the flow speeds and Mach number through the LPC was the most challenging aspect of the design. Due to the reduction to a 3-stage configuration, the energy in the flow was relatively higher. The criteria for relative and tangential Mach numbers entering rotors (≤1.4) was met. **Figure 28** –**Figure 30** show the variation of entering Mach numbers through the respective blades. All Mach numbers - relative and absolute respectively - exiting every blade were subsonic. This was done to reduce the probability of unrealistic flow solutions at the trailing edges. Analyzing the turning of supersonic flow requires the use of more advanced tools that were outside the scope of this project.

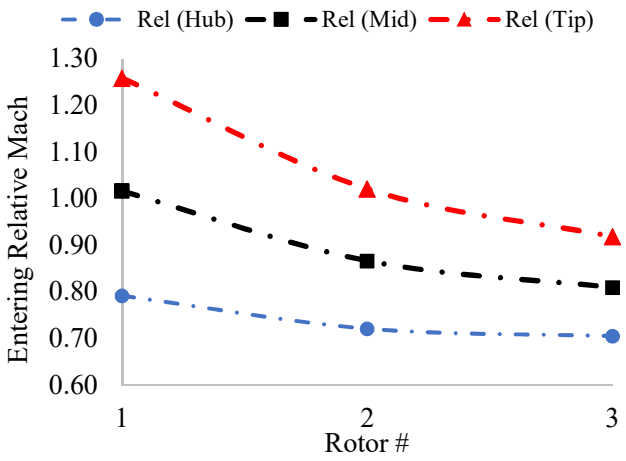

Figure 28: Entering relative Mach number variation

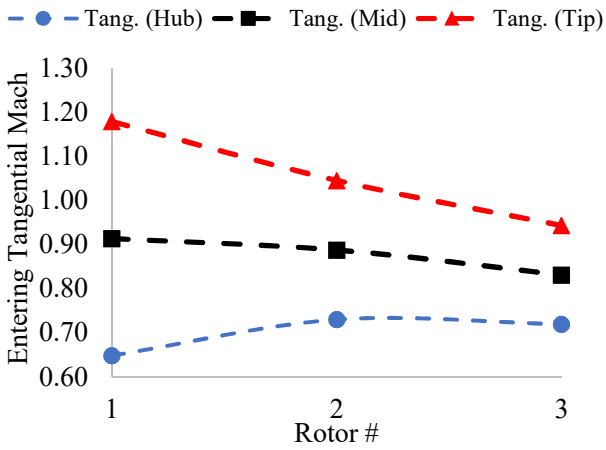

Figure 29: Entering tangential Mach number variation

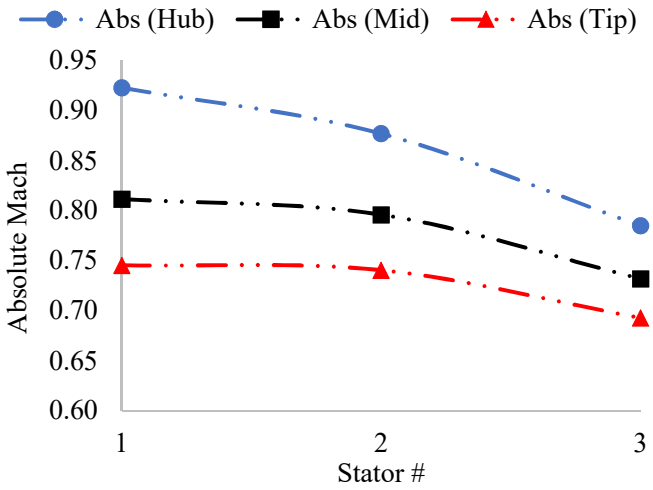

Figure 30: Entering absolute Mach number variation

3.2.4.2 Velocity triangles

Figure 31 displays the cascade view of the 1st stage mid span location. All aerodynamic properties for the LPC can be found in Appendix A.

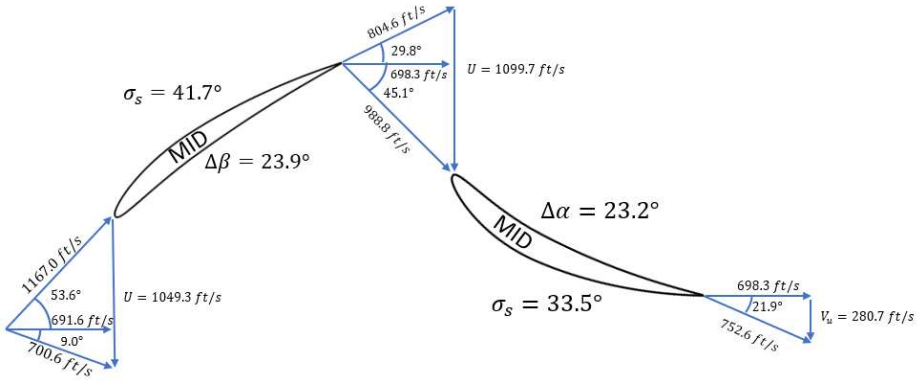

Figure 31: LPC stage 1 cascade (MID)

The axial velocity played a major role in optimizing the performance of the compressor and annulus shape. This was done iteratively to converge on an optimum flow coefficient, stage loading, and stage PR distribution. Finally, the total turning angles (Δα, Δβ) of all blades met the criteria to remain ≤ 45°. Shown in **Figure 32** is the final cascade view for the LPC. All final values for aerodynamics of the LPC can be found in Appendix A.

Figure 32: LPC complete cascade view

3.2.5 Stage Health Assessment

As mentioned in section 3.1.2, the stage health was assessed using both DeHaller numbers and Lieblein Diffusion Factors. Below is the summary of both health criteria relevant to the LPC.

3.2.5.1 DeHaller Number

Table 24 below shows all DH for the LPC at all span locations.

Table 24: LPC blade spanwise DeHaller numbers

Stage #	Rotors			Stators		
	Hub	Mid	Tip	Hub	Mid	Tip
1	0.768	0.689	0.706	0.691	0.761	0.812
2	0.775	0.721	0.732	0.680	0.731	0.773
3	0.761	0.739	0.749	0.684	0.731	0.771

All DH criteria was met. However, the DF is also monitored as it offers a higher fidelity and a higher order check on the airfoil health.

3.2.5.2 Lieblein Diffusion Factor

The DFs are show below in **Table 25.**

Table 25: LPC blade spanwise Diffusion Factor

Stage #	Rotors				Stators			
	Hub	Mid	Tip	**Avg**	Hub	Mid	Tip	**Avg**
1	0.398	0.460	0.427	**0.428**	0.501	0.451	0.402	**0.451**
2	0.432	0.457	0.424	**0.438**	0.528	0.499	0.465	**0.497**
3	0.474	0.464	0.457	**0.465**	0.606	0.571	0.539	**0.572**

3.2.6 Stage Characteristics

The stage characteristics shown in this section include: λ, ϕ, and °R. These characteristics help assess the performance of the LPC.

3.2.6.1 Flow Coefficient and Stage Loading

ϕ was selected for the 1st stage of the LPC. Due to the direct relationship of ϕ with RPM, by selecting ϕ, the optimal RPM was calculated to not exceed the criteria at the 1st stage. ϕ was then controlled with the use of the V_{ax} through the rotors and stators. The final distribution of ϕ is shown in **Figure 33**. In the same figure is the final distribution of λ. All stage loading met the design criteria limits and known trends.

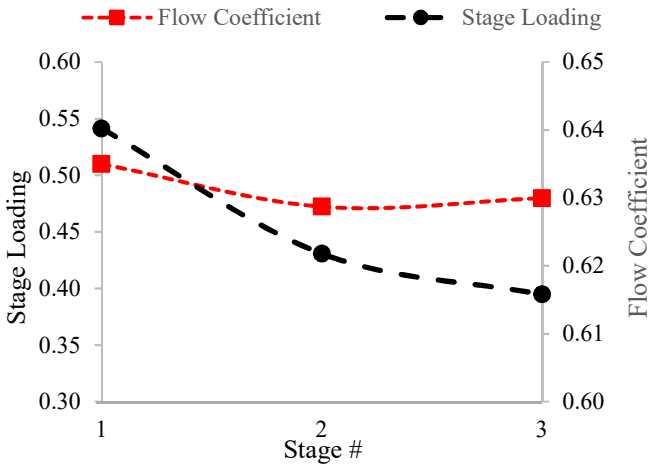

Figure 33: LPC 1st stage flow coefficient and stage loading distribution

Degree of Reaction (°R)

The °R at the mid-span are shown in **Figure 34**. A higher °R indicates greater enthalpy rise in the rotor cascade and greater flow deceleration in the relative F.O.R.

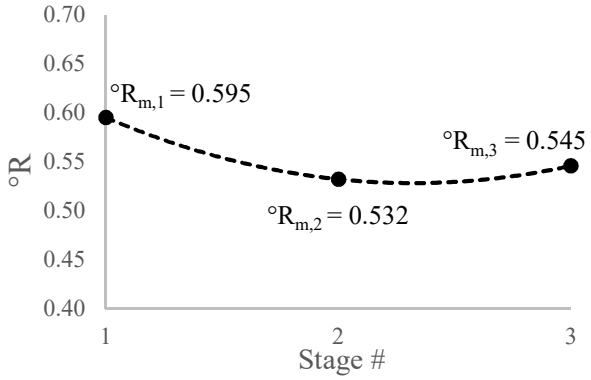

Figure 34: LPC degree of reaction at mid-span

3.2.7 **Inter-Compressor Duct**

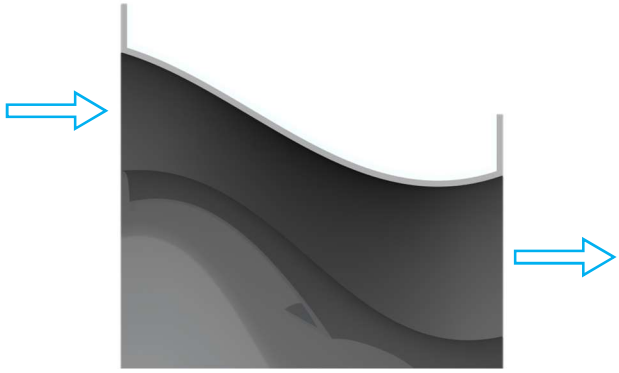

Figure 35: Inter-compressor duct side view

At the exit of the LPC, the downstream architecture of the HPC demanded an inter-compressor duct (ICD). The hub radius at the exit of the LPC is 16.0 [in] and 11.1 [in] at the inlet of the HPC. Similarly, the tip radius for the exit of the LPC is 19.8 [in] and 16.2 [in] for the HPC. Due to these differences, the duct was designed to redirect the flow in a smooth manner to avoid any disruption or flow separation. The duct geometry was constrained by a maximum decreasing wall angle of 30°. The HPC design is sensitive to the entering Vax and Mach number, therefore the flow speed was kept constant. The duct length is 11.6 [in.] with a maximum wall angle of 29.9°.

The duct was assumed to be adiabatic with the total pressure loss through the duct assumed to be 1%. An initial estimation in the cycle design assumed for the loss to be 0.5%, modeling a standard duct. However, due to the abnormal shape and turning of the duct, the total pressure loss estimate was increased to 1.0% as a safety margin. Further investigation and CFD would be necessary to more accurately model the total pressure loss for this duct.

3.3 HPC Design

Figure 36: Isometric view of HPC

Table 26: HPC Characteristics

π_{HPC}	**5.882**
τ_{HPC}	1.715
η_{tt}	0.864
Stages	5
Length	15.9 [in]

The high-pressure compressor is designed to achieve a total pressure ratio of 5.88 in 5 stages. This is more efficient than that of the baseline engine that achieved a total pressure ratio of 4.25 in 7 stages. The length of the proposed high-pressure compression system is 15.9 [in] as compared to 19.0 [in] for that of the baseline engine. The design choices, thermodynamics, aerodynamics, health assessment, and geometry will be discussed below.

3.3.1 Design Choices

The stage design choices are outlined in **Figure 37** and **Figure 38**. The stage pressure ratios are design to decrease smoothly without plateauing towards the later stages. The adiabatic efficiencies are design to the lowest at the boundary stages and the largest toward the middle stages.

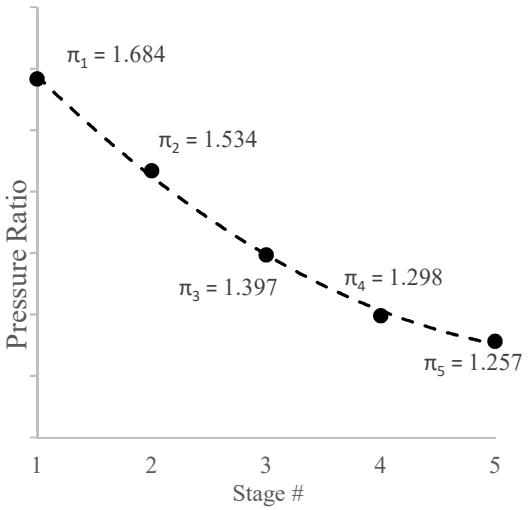

Figure 37: Stage pressure ratio distribution

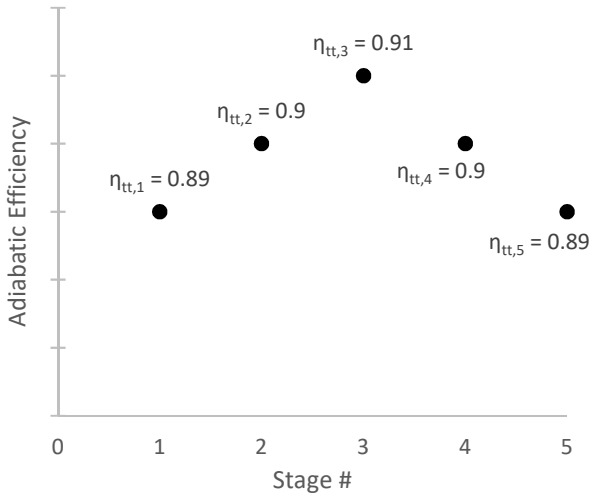

Figure 38: Stage adiabatic efficiency selection

With the backbone of the HPC design, above, the rest of the design was highly dependent upon the 1st stage design choices. Outlined in **Table 27** are the HPC 1st stage design parameters. The HPC was also constrained with exit conditions of no swirl and exit Mach of approximately 0.3. **Figure 39** displays the design choices made for axial velocity variation across the HPC. Design choices for stator $\Delta\alpha$ can be found in **Table 58** located in Appendix B.

Table 27: HPC 1st stage design choices

M_0	**0.55**
α_{IGV}	16°
H/T	0.72
RPM	10158
α_{exit} [Deg]	26.7

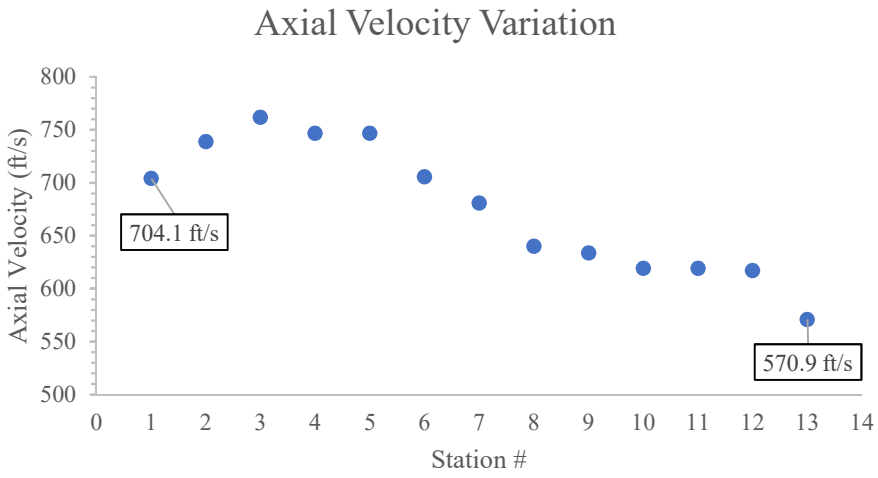

Figure 39: Axial velocity variation across HPC

3.3.1.1 *Tandem* Outlet Guide Vane (OGV)

The high-pressure compressor design necessitated the use of a tandem outlet guide vane. This design, illustrated in **Figure 40**, is used to divide the amount of swirl removed from the flow. The first vane removed 18.9° of swirl and the second removed 36.8°. This design allowed for the swirl to be completely removed as well as decelerating the axial velocity to a manageable magnitude for the compressor exit diffuser without added risks for flow separation. The division of swirl removal provided for reasonable DH and DF values for both vanes.

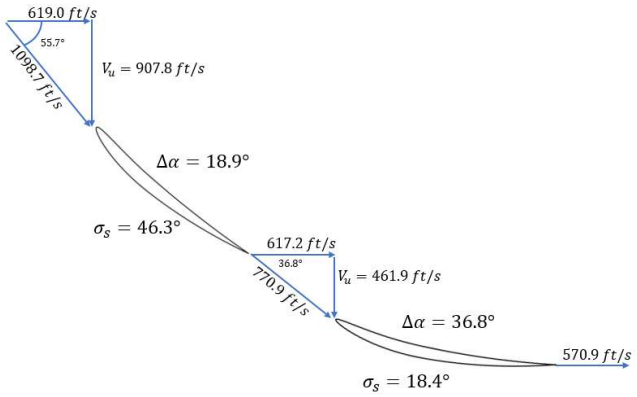

Figure 40: Cascade view of Tandem Compressor Vane

3.3.2 Geometry

Figure 41 shows the meridional view of the HPC. The figure also displays station numbering used for reference in later sections.

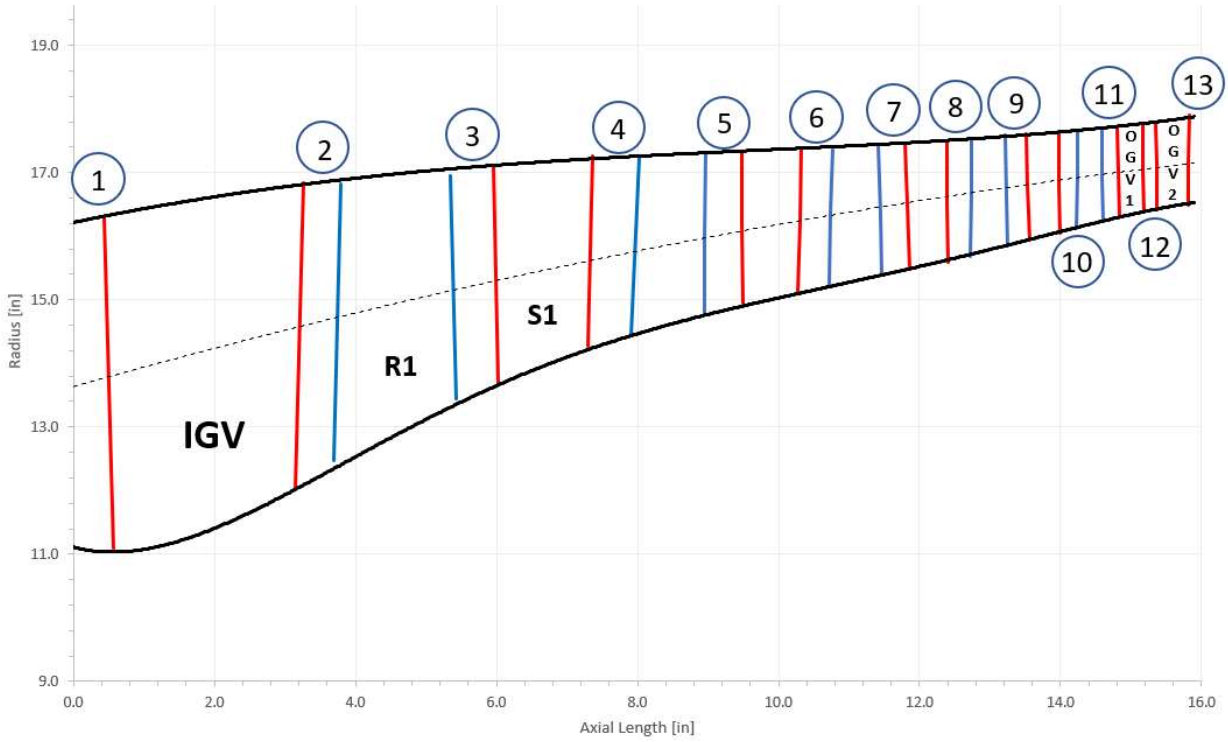

Figure 41: HPC Meridional View

The above figure displays 12 rows of blades including the IGV and OGV. **Table 28** summarizes the characteristics of each row. Data for NOB, pitch at the hub, aspect ratio, and taper ratio is displayed for each row of blades.

Table 28: HPC blade characteristics

Stage #	Rotors				Stators			
	NOB	S_{hub} [in]	AR	TR	NOB	S_{hub} [in]	AR	TR
IGV	-	-	-	-	32	2.181	1.80	1.10
1	50	1.530	1.80	0.90	55	1.544	1.85	1.10
2	69	1.295	1.90	0.90	84	1.113	1.95	1.10
3	96	0.992	2.00	0.90	109	0.889	2.05	1.10
4	122	0.805	2.10	0.90	139	0.718	2.15	1.10
5	157	0.643	2.20	0.90	178	0.575	2.25	1.10
OGV	-	-	-	-	188	0.550	2.30	1.10

The spacing between the blade rows is plotted in **Figure 42**. The spacing between the IGV and rotor 1 was set to 20% of the pitch of rotor 1. Towards the third stage this plateaus to 40% of the pitch of the downstream blade.

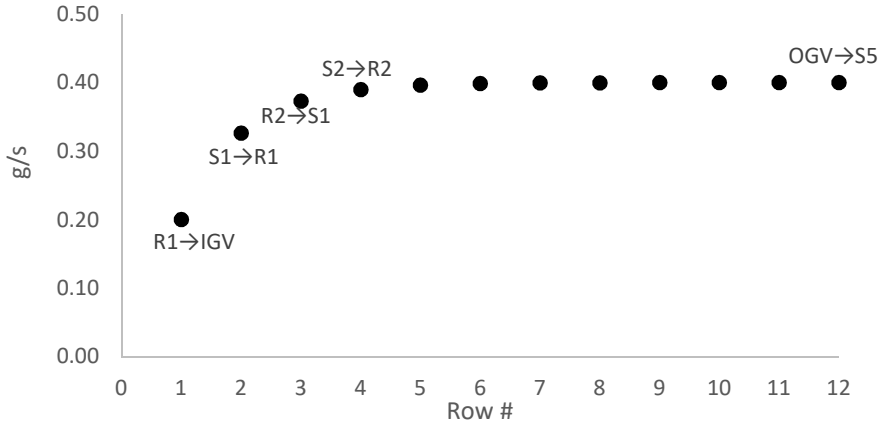

Figure 42: HPC row gap to pitch ratio

3.3.3 **Thermodynamics**

The h-s diagram for the HPC is displayed in **Figure 43**. The inlet of the HPC is denoted by station 2.5 with the respective total quantities denoted by 02.5. The exit is denoted by station 3. A designed pressure ratio of 5.88 increases the entry total pressure of 34.5 psi to 201.5 psi at the exit. Additionally, a variable specific heat model was implemented for the thermodynamic analysis of the HPC.

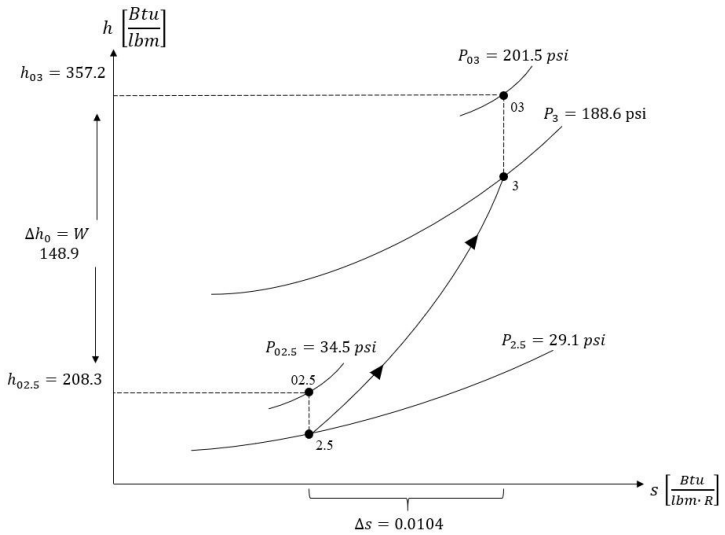

Figure 43: HPC h-s Diagram

The change in total/static pressures and temperatures across the HPC is displayed in **Figure 44**. With respect to the total gas properties, increases are seen across the rotors while the decreases in total pressure are seen across the stators/vanes.

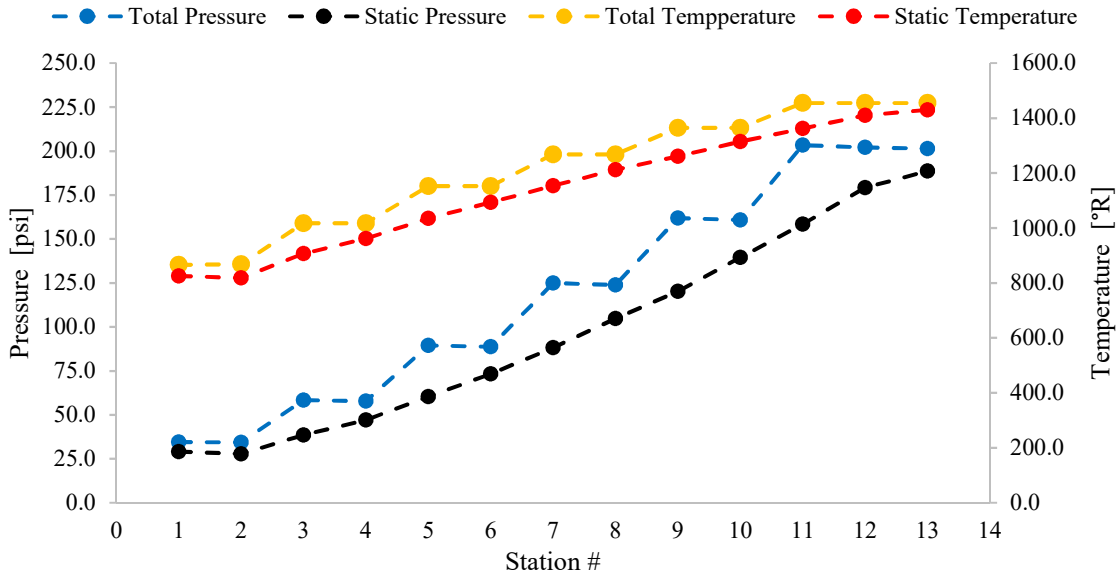

Figure 44: HPC pressure and temperature change

3.3.4 **Aerodynamics**

Figure 45 displays the cascade view and velocity triangles for the 1st stage of the HPC. The complete list of aerodynamic data for the HPC can be found in **Table 61**, located in Appendix B.

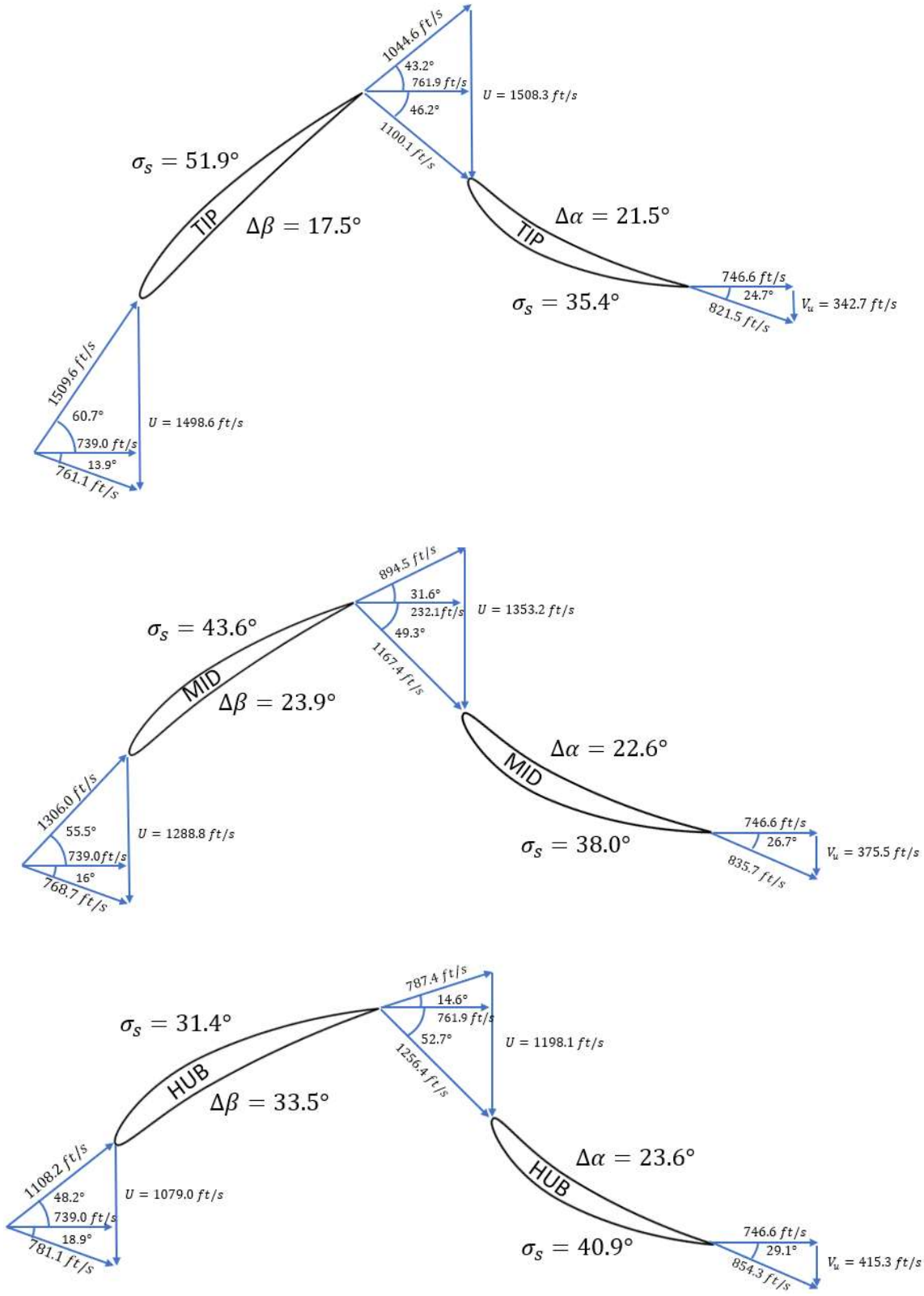

Figure 45: Cascade view and velocity triangles for HPC Stage 1

Figure 46 shows the cascade view of blades within the HPC. The incoming and exit swirl can be seen to be zero degrees.

Figure 46: Cascade view of HPC

3.3.5 Stage Health Assessment

The Diffusion Factors and De Haller numbers are listed in **Table 29**. All De Haller numbers and Diffusion Factors abide by the criteria set forth in the **Design Criteria** section**.**

Table 29: HPC Stage Health Assessment

		Stage					
		1	**2**	**3**	**4**	**5**	**OGV**
DF_{Rotor}	TIP	0.474	0.491	0.477	0.423	0.396	
	MID	0.501	0.518	0.509	0.450	0.416	
	HUB	0.501	0.534	0.536	0.474	0.437	
	AVG	**0.492**	**0.514**	**0.507**	**0.449**	**0.416**	
DF_{Stator}	TIP	0.477	0.472	0.470	0.486	0.490	0.540
	MID	0.500	0.485	0.478	0.496	0.501	0.559
	HUB	0.525	0.498	0.487	0.506	0.512	0.579
	AVG	**0.501**	**0.485**	**0.478**	**0.496**	**0.501**	**0.559**
DH_{Rotor}	TIP	0.692	0.705	0.708	0.741	0.756	
	MID	0.685	0.698	0.696	0.730	0.746	
	HUB	0.711	0.707	0.694	0.724	0.738	
DH_{Stator}	TIP	0.747	0.724	0.715	0.709	0.712	0.750
	MID	0.716	0.707	0.703	0.697	0.702	0.741
	HUB	0.680	0.688	0.690	0.686	0.691	0.730

3.3.6 **Stage Characteristics**

The criteria set for the HPC follows the same guidelines set for the LPC. **Figure 47**, **Figure 48**, and **Figure 49** display the stage Degree of Reaction, Work Coefficient, and Flow Coefficient, respectively.

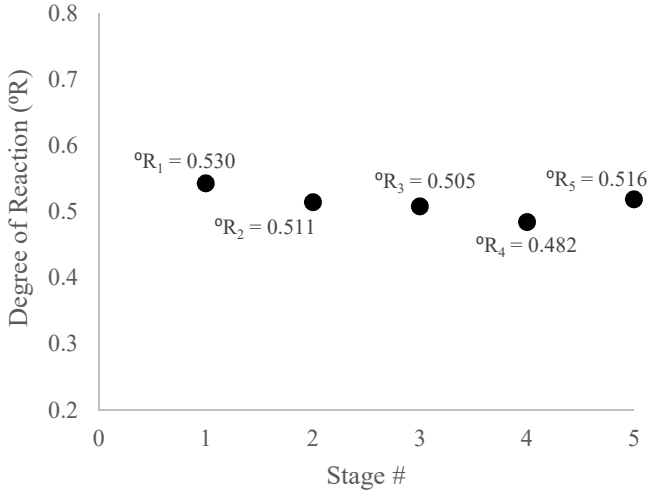

Figure 47: HPC stage Degree of Reaction

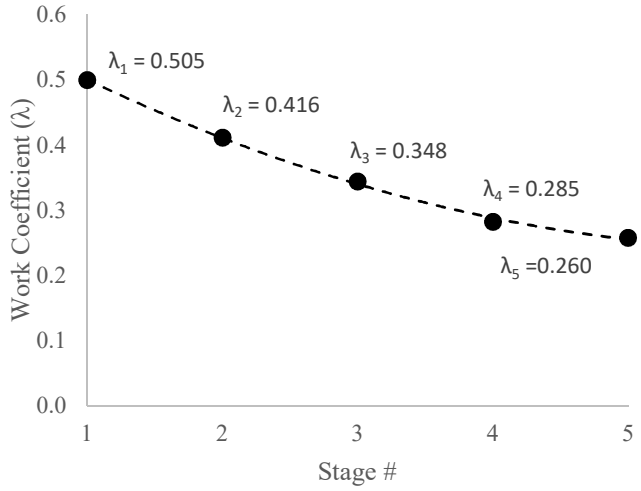

Figure 48: HPC stage Work Coefficient

Like the LPC, the stage degree of reaction was aimed to be the lowest at the 1st stage and settle at around 0.5 toward the later stages. Due to the difficulty of the design, the 1st stage yielded the highest degree of reaction leaving the later stages near the target value. The stage work coefficient started under 0.6 and subtly decreased across the stages. The design ended with a work coefficient well above 0.2 leading to the conclusion that reducing the stages to 4 would be difficult and yield a less healthy design.

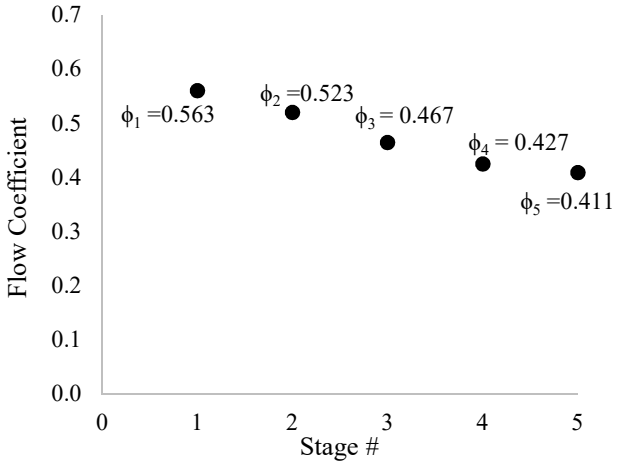

Figure 49: HPC stage Flow Coefficients

4 Combustion Chamber

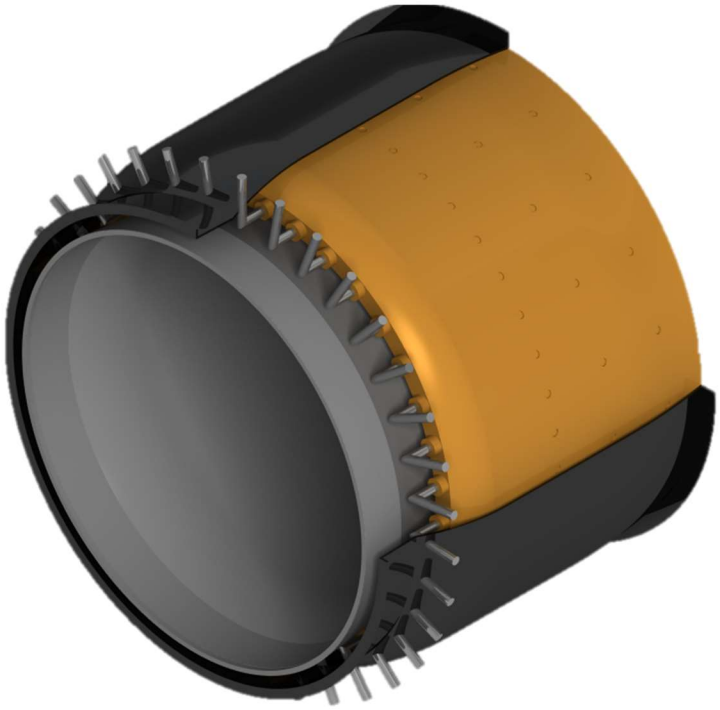

Figure 50 : Combustion Chamber Isometric View

The principal function of a combustion chamber on any propulsion system is to increase the thermal energy of an incoming flowing gas stream through combustion. [8]

The engine's combustion chamber is an annular combustion chamber due to its significant advantages w.r.t size, pressure losses and ignition behavior. These advantages make the annular combustion chamber an ideal chamber [14]. Modern propulsion systems like General Electric's CFM-56, and Rolls Royce's Trent900 make use of annular combustion chambers.

In addition to the annulus chamber, a popular method commonly known as "staged combustion" was employed. It uses two separate zones, each designed specifically to optimize combustion performance [14]. Staged combustion consists of having the needed temperature rise occur in the first zone. This method ensures that both zones maintain smoke and NOx emissions to a minimum.

4.1 Design Point

The combustion inlet parameters at the design point depend on cycle analysis and on the exit conditions of the HPC. The utilized parameters are listed in **Table 30**.

Table 30: Exit HPC and Inlet Combustion Chamber Conditions

Parameter	Symbol	Value	Units	Reference
Air Mass Flow at Inlet	$m_{dot,3}$	203.92	lbm/s	Compressor Design
Total Temperature at Inlet	$T_{T,3}$	1454.94	R	Cycle Analysis
Static Temperature at Inlet	T_3	1430.70	R	Compressor Design
Total Pressure at Inlet	$P_{T,3}$	201.46	psi	Cycle Analysis
Static Pressure at Inlet	P_3	188.62	psi	Compressor Design
Air Density at Inlet	ρ_3	0.3560	lbm/ft^3	Compressor Design
Area at Inlet	A	144.46	in^2	Compressor Design
Ratio of specific heats	ɣ	1.3544	/	Compressor Design
Universal Gas Constant	R	0.0658	BTU/lb.R	Cycle Analysis
Mach Number at Inlet	M	0.3131	/	Compressor Design
Specific Heat	Cp	0.2629	BTU/lb.R	Compressor Design
Velocity at Inlet	V	570.89	ft/s	Compressor Design
Pressure Ratio of Burner	πb	0.96	/	Cycle Analysis

4.2 Diffuser Design

Incoming velocity from the HPC tends to be around M = 0.3. Ideally the incoming flow must be decelerated in the shortest distance possible before entering the combustion chamber. The best method to decelerate this flow is to utilize a diffuser after the HPC and before the combustion chamber inlet. All this must be done while maintaining pressure losses at a minimum.

According to Mattingly [8], the best possible wall angle for the diffuser is 2θ = 9°. Also mentioned by Mattingly, when dealing with area ratios (A2/A1) smaller than 4, the length of the diffuser can be divided by the number of splitter plates used, resulting in a shorter diffuser. Following Mattingly's method for a pre-burner diffuser, geometry parameters and pressure losses were calculated and are displayed in **Table 31**.

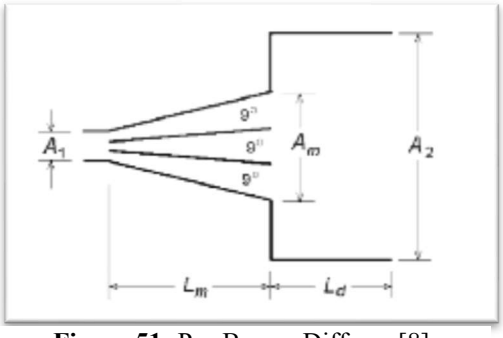

Figure 51: Pre-Burner Diffuser [8]

The downside of having a pre burner diffuser is the decrease in total pressure that happens from decelerating flow. Following Mattingly's method, total pressure loss from the diffuser was calculated as shown below:

$$\Delta P_t = \left(1 - \frac{1}{AR^2}\right) * (1 - \eta D) \quad (12)$$

Table 31: Diffuser Calculated Parameters

Parameter	Symbol	Value	Unit	Reference
Diffuser Inlet Area	A_3	144.46	in2	Compressor Design
Diffuser Flat Wall Area	$A_{3.1}$	291.86	in2	Calculated
Diffuser Exit Area	$A_{3.2}$	334.64	in2	Calculated
Total Pressure at Diffuser Inlet	$P_{T,3}$	201.46	psi	Compressor Design
Pressure Loss in the Diffuser	dP	0.994	psi	Calculated
Total Pressure at Diffuser Exit	$P_{T,3.2}$	200.45	psi	Calculated
Length of the Diffuser	L	6.1023	in	Calculated
Mach Number at Diffuser Exit	$M_{3.2}$	0.13	/	Calculated
Efficiency of flat wall	ηD	0.9378	/	Mattingly
Area Ratio	AR	2.316	/	Calculated

4.3 Geometry

The geometrical aspects of the main burner are limited by the overall engine size, inlet area to the burner and the desired exit area to the High-Pressure Turbine. The engines combustion chamber dimensions were calculated around the main burner length which was calculated following [8], [14] and [15] approach. **Figure 52** illustrates the basic geometry of the combustion chamber.

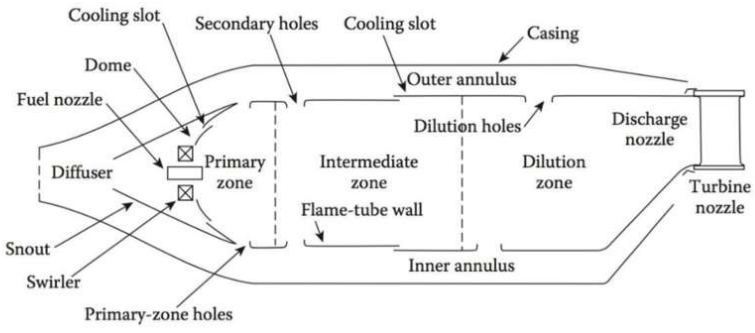

Figure 52: Combustion Chamber [14]

Following Mattingly's approach for combustion chambers of similar design, the following equation was used a scaling law:

$$L \propto \frac{P_{o3}^{-r}}{T_{o4}} \tag{13}$$

The equation above represents the relationship between the overall length of the combustion chamber with total pressure at the inlet, a constant (r), and total temperature at the exit. Where r = 1.51 if n = 1.8, and r = 0.714 if n = 1. Where n is an experimentally determined constant and n = 1 at high pressures [Mattingly, 8]. Following Mattingly's length calculation, a contemporary table of similar engine's geometrical parameters is presented. **Figure 53** displays industry contemporary main burners.

Engine Type	TF39 Annular	TF41 Cannular	J79 Cannular	JT9D Annular	F100 Annular	T63 Can
Mass Flow						
Air (lb/s)	178	135	162	242	135	3.3
Fuel (lb/h)	12,850	9,965	8,350	16,100	10,580	235
Size						
Length (in)	20.7	16.6	19.0	17.3	18.5	9.5
Diameter (in)	33.3	5.3/24.1*	6.5/32.0*	38.0	25.0	5.4
P_{t3} (psia)	382	314	198	316	366	92
T_{t4} max (°R)	2915	2620	2160	2865	3025	1840
* Can Diameter/Annulus Diameter						

Figure 53: Contemporary Main Burners

The procedure to calculate the length for the burner from this this figure was the following. First, an engine was picked that resembled the design. After analyzing all 6 engines in **Figure 53**, the engine that resembled the BFTJ the most was the J79. Since the engine has a slightly higher mass fuel flow, it required a larger diameter in comparison with the BFTJ. The ratios were calculated for the BFTJ as well as for the J79. The BFTJ ratio was then divided by the J79 ratio and multiplied by 100 to get a sizing percentage. Using the outlined method, a length was calculated for the BFTJ. Maintaining the same L/D as the J79 ratio for feasibility, a final length for the combustion chamber was computed as shown below.

The main burner is then subdivided into 3 main zones which are the primary zone, secondary zone, and dilution zone. Following the method from [15], the primary zone is about 28% of the combustion chamber length. The secondary

zone is about 43.2% and the dilution zone is 28.8%, respectively . **Table 32** represents the calculated values for the geometry of the combustion chamber.

Table 32: Primary Geometry of Main Burner

Parameter	Symbol	Value	Unit	Reference
Total Pressure at Diffuser Inlet	$P_{T,3}$	201.46	psi	Compressor Design
Total Temperature at Main Burner Exit	$T_{T,4}$	3700.0	R	Cycle Analysis
Equation 16 Ratio	R	0.000346	/	Calculated
Casing Diameter	D	40	in	Calculated
Main Burner Length	L	23.740	in	Calculated
Primary Zone Length	L_{PZ}	6.649	in	Calculated
Secondary Zone Length	L_{SZ}	10.259	in	Calculated
Dilution Zone Length	L_{DZ}	6.838	in	Calculated

From these calculated parameters an in-dept calculation of different sections of the combustion chamber can be calculated following the outlined methods in [15] and [8]. **Table 33** portrays the parameters calculated following this method.

Table 33: Geometry of Main Burner

Parameter	*Symbol*	Value	Unit	Reference
Casing Diameter	D	40	in	Calculated
Combustor Diameter	D_C	33.46	in	Calculated
Inner/Outer Annulus Height	H_{AN}	0.586	in	Calculated
Snout Height	H_s	1.149	in	Calculated
Swirler Height	H_{SW}	1.551	in	Calculated
Height of Flame Tube	H_L	2.858	in	Calculated
Pattern Factor	PF	0.35	/	Calculated
Main Burner Exit Diameter	D_4	17.86	in	Calculated
Optimal Height Ratio	α_{OPT}	22.03	/	Calculated
Combustor Height	H_R	3.326	in	Calculated
Dome Height	H_L	1.862	in	Calculated
Half Passage Height	H_p	0.720	in	Calculated

4.4 Mass Flow Distribution

The annular combustion chamber has different sections into which the mass flow divides itself to meet desired conditions like fuel to air ratio as well as to make sure that it meets the cooling demands. Under normal circumstances the mass flow distribution throughout the combustion chamber does not change. **Table 34** shows the amount of mass flow that goes through each zone of the main burner.

Table 34:Mass Flow Distribution

Parameter	Symbol	Value	Unit	Reference
Mass Flow Rate at Burner Inlet	$\dot{m}$	203.88	lbm/s	Compressor Design
Mass Flow Rate at Annulus	$\dot{m}_{AN}$	163.12	lbm/s	Calculated
Mass Flow Rate at Recirculation	$\dot{m}_{RZ}$	40.763	lbm/s	Calculated
Mass Flow Rate at Dome	$\dot{m}_{DCool}$	16.298	lbm/s	Calculated
Mass Flow Rate at Swirler	$\dot{m}_{SW}$	40.763	lbm/s	Calculated
Mass Flow Rate at Primary Zone	$\dot{m}_{PZ}$	130.49	lbm/s	Calculated
Mass Flow Rate at Secondary Zone	$\dot{m}_{SZ}$	171.27	lbm/s	Calculated
Mass Flow Rate at Dilution Zone	$\dot{m}_{DZ}$	212.06	lbm/s	Calculated
Mass Flow Rate for Cooling	$\dot{m}_{cooling}$	91.756	lbm/s	Calculated

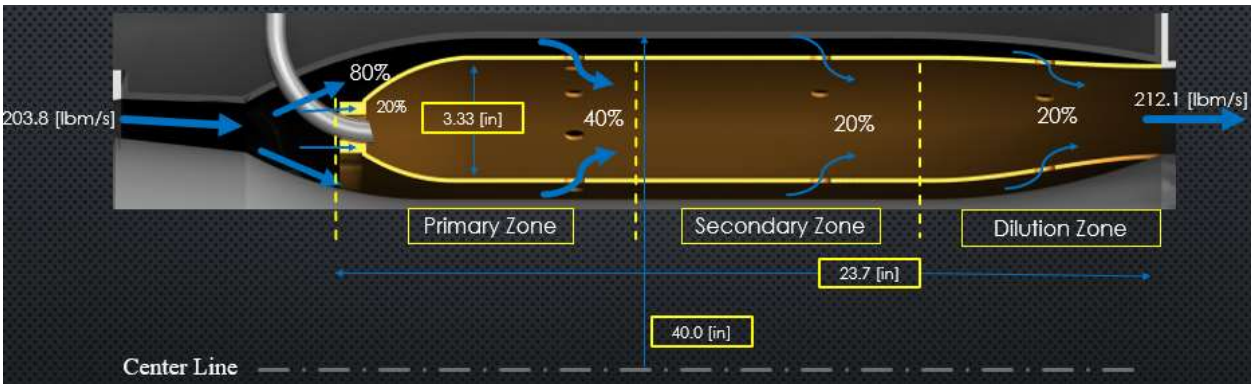

Figure 54: Mass flow distribution through the combustion chamber

Figure 54 illustrates the mass flow distribution through the combustion chamber. The 203.8 [lb_m/s] that enter the combustion chamber gets divided into 2 primary zones. The annulus takes 80% of the mas flow which will later be used as coolant air for the hottest parts of the engine. The other 20% goes through the swirler which later is combined with fuel to be ignited. As seen on **Figure 54**, of the 80% of the mass flow that enters the annulus, 40% is put back into the primary zone of the combustion chamber through 40 dilution holes. Later, of the remaining mass flow in the

annulus, 20% goes into the secondary zone through 20 dilution holes and another 20% goes into the dilution zone through 20 dilution holes. The purpose of the annulus and dilution holes is to cool the flow and to protect the material from extremely hot temperatures that can be reached inside the combustion chamber.

4.5 Fuel System

4.5.1 Fuel Injection

Liquid atomization and evaporation are of extreme importance to the process of combustion. Normal liquid fuels are not sufficiently volatile to produce vapor in the amounts required for ignition and combustion unless they are atomized into many droplets with a corresponding, vastly increased surface area [14]. When talking about fuel injection there are 2 main atomizers: pressure swirl atomizers and air blast atomizer. According to [14], pressure swirl atomizers have good mechanical reliability and an ability to sustain combustion at very weak mixture strengths. Their drawbacks include potential plugging of the small passages and orifices by contaminants in the fuel and an innate tendency toward high soot formation at high-combustion pressures. The combustion chamber of the BFTJ has Air Blast Atomizers because of significant advantages which include fuel distribution dictated by the airflow pattern and the components are protected from overheating by the air flowing over them.

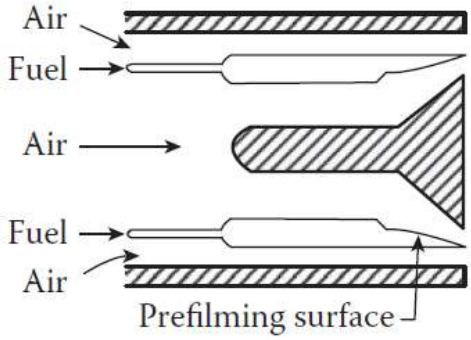

Figure 55: Air-Blast Atomizer [14]

4.5.2 Number of Fuel Injectors

According to Mattingly [8], for a single array, the number of fuel nozzles required can be calculated by dividing the annular flow passage into square segments. The following equation was used to calculate the number of fuel injectors needed and the results are shown in **Table 35**.

$$N_{noz} \approx \frac{\pi(r_o + r_i)}{H_r} \tag{14}$$

Table 35: Fuel injector calculations

Parameter	Symbol	Value	Unit	Reference
Fuel Injectors	N_{noz}	28.20	/	Equation 23
Fuel Injectors Used	N_{noz}	29	/	Round Up

4.5.3 Fuel Atomizing Flow

For the BFTJ, Mattingly's approach was used as a guide to design the atomization of the flow. **Table 36** shows different parameters used to calculate the fuel atomizing flow.

Table 36: Fuel Atomizing Flow

Parameter	Symbol	Value	Unit	Reference
Mass Flow Rate at Burner Inlet	$\dot{m}$	203.8	lbm/s	Compressor Design
Fuel Flow Rate	$\dot{m}_f$	8.148	lbm/s	Calculated
Atomize Air to Fuel Ratio	AFR	3	/	[8]
Fuel Atomizing Flow	$\dot{m}_{FAF}$	15.10	lbm/s	Calculated

4.6 Liner Cooling

The primary zone of the combustion chamber is the section with the highest temperature of the entire engine. Temperatures may reach 4500 [°R] or average around 3600 [°R], which is greater than the metal in the main burner can withstand. Consequently, proper cooling must be applied through the combustion chamber especially in and aft of the primary zone. The burner liner and the burner dome must have proper allocation of cooling mass flow to withstand the harsh temperatures at that section. According to Mattingly [8], "The coolant air is normally introduced through the liner in such a way that a protective blanket or film of air is formed between the combustion gases and the liner hardware".

Although there is many different techniques and implementations for liner cooling, the burner will utilize pedestal tile film cooling. This cooling method is both cost effective, weight aware and utilizes minimal airflow. This makes it the most ideal cooling method for the BFTJ's needs.

According to Mattingly [8], regardless of the method implemented on the main burner, the effectiveness of the cooling method can be quantified using equation 15. **Figure 56** illustrates the applied method to compute the cooling air percentage.

$$\emptyset = \frac{T_g - T_m}{T_g - T_c} \tag{15}$$

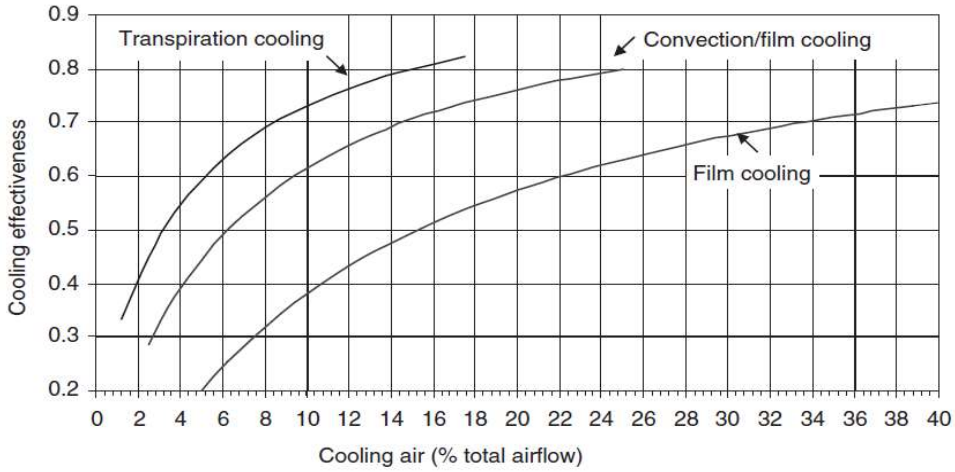

Figure 56: Combustion Liner Cooling [8]

Following the equation above, an effectiveness parameter was calculated. Utilizing film cooling and having calculated the cooling effectiveness of the main burner, using **Figure 56** we can estimate the cooling air as a percentage of the total mass flow. **Table 37** shows this process and final parameters.

Table 37: Cooling Mass Flow Rate

Parameter	Symbol	Value	Unit	Reference
Hot Gas Temperature	T_g	4500	R	Mattingly
Desired Wall Temperature	T_m	3600	R	Mattingly
Total Temperature at HPC Exit	T_C	1454.9	R	Compressor Design
Cooling Effectiveness	Φ	0.768	/	Equation 17
Mass Flow Rate for Cooling	$\dot{m}_{cooling}$	88.66	lbm/s	Table 35

4.7 Combustion Efficiency

According to [Farokhi, 9] the combustion efficiency measures the actual rate of heat release in a burner and compares it with the theoretical heat release rate possible. In other words, the combustion efficiency of this burner is compared to a theoretical value and consequently computing a percentage of combustion efficiency. “The theoretical heat of reaction of the fuel assumes a complete combustion with no unburned hydrocarbon fuel and no dissociation

of the products of combustion. The actual heat release is affected by the quality of fuel atomization, vaporization, mixing, ignition, chemical kinetics, flame stabilization, intermediate air flow, liner cooling, and, in general, the aerodynamics of the combustor" [9].

Using equation (16) a combustor loading factor is computed, utilizing the combustor loading factor and **Figure 57** the efficiency of the combustion chamber can be calculated.

$$\mathrm{CLP} = \theta = \frac{P_{t3}^{0.75} * A * H * e^{\frac{Tt3}{b}}}{\dot{m}} \tag{16}$$

Where the parameter used in equation 16 (b) can be calculated using equation 17

$$b = 382\left(\sqrt{2} \pm \ln\frac{\emptyset PZ}{1.03}\right) \tag{17}$$

[(+) for $\phi < 1.03$, (−) for $\phi > 1.03$]

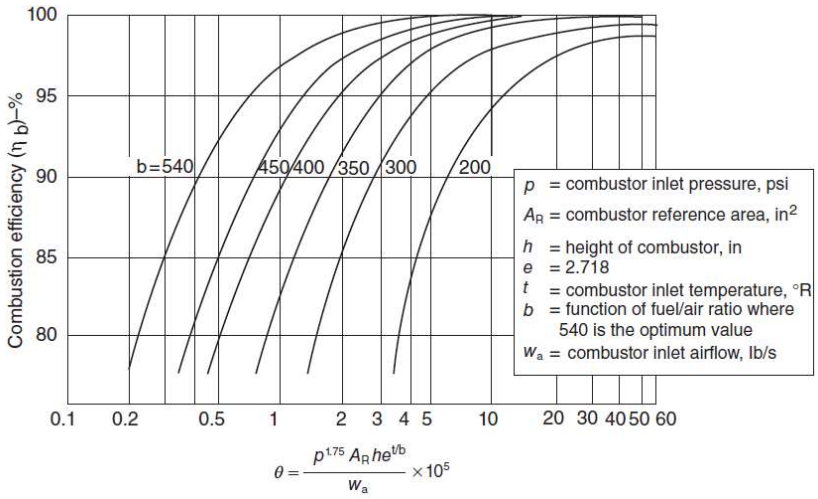

Figure 57: Combustion Efficiency [9]

Table 38: Combustion Efficiency Result

Parameter	Symbol	Value	Unit	Reference
Equivalence Ratio of Primary Zone	Φ_{PZ}	0.91	/	Calculated
Function of Fuel to Air Ratio	b	493	/	Calculated
Combustor Loading Factor	CLP	153 x105	/	Calculated
Combustion Efficiency	ηb	0.999	/	Theoretical
Combustion Efficiency	ηb	0.998	/	Figure 59

4.8 Thermodynamics of the Combustion Chamber

The thermodynamic parameters of the combustion chamber are limited by HPC exit conditions, the type of fuel that the engine uses, the geometry of the combustion chamber and by the sought conditions for the HPT. Amongst these sought conditions, the most important one is the total temperature entering the HPT. This total temperature is set on the early stages of the cycle analysis and its crucial because it is the highest temperature in the cycle analysis. **Table 39** displays the thermodynamic design parameters of the combustion chamber.

Table 39: Thermodynamic Design Parameters

Parameter	Symbol	Value	Unit	Reference
Total Temperature Exiting the Main Burner	$T_{T,4}$	3700	R	Cycle Analysis
Stoichiometric FAR (fuel to air ratio)	f_{ST}	0.0685	/	Calculated
Snout Discharge Coefficient	C_{DS}	1	/	[Melconian]
Equivalence Ratio in Primary Zone	Φ_{PZ}	0.911	/	Calculated
Equivalence Ratio in Secondary Zone	Φ_{SZ}	0.310	/	Calculated
Fuel to Air Ratio	f	0.0399	/	Calculated
Mass Flow Rate	m_f	8.148	lbm/s	Calculated

The process followed to calculate the thermodynamics of the primary zone , secondary zone and dilution zone is outlined in [15]. It consisted of calculating the flame temperature and adding it to the temperature entering the zone. The following equations outline the process followed to calculate parameters in the primary zone. The same process was utilized to calculate parameters in secondary zone and dilution zone

$$T_{out,PZ} = T_3 + \eta_{PZ}\Delta T_{PZ} \tag{18}$$

$$\eta_{PZ} = 0.71 + 0.29\tanh\left[1.5475x10^{-3}(T_3 + 108lnP_3)\right] \tag{19}$$

Where ΔT_{PZ} represents the ideal temperature rise between inlet and exit of the zone and can be computed as follows [15]:

$$T_{AFT} = T_3 + \frac{\emptyset fst}{Cp} \tag{20}$$

$$\Delta T_{PZ} = T_{AFT} + T_3 \tag{21}$$

$$f_{ST} = \frac{36x+3}{103\,(4x+y)} \quad \text{where for Fuel Jet A x=12 and y = 23} \tag{22}$$

Following [14], estimations for the number of dilution holes per each zone can be utilized for a combustion chamber of our dimensions. According to [15], a combustion chamber of the BFTJ's dimensions has 40 dilution holes in the

primary zone, 20 dilution holes in the secondary zone and 20 dilution holes in the dilution zone. The mass flow per each hole was calculated as follows:

$$m_{Hole} = \frac{m_{AN}}{Nt} \tag{23}$$

Where N_t is the total number of dilution holes along the primary, secondary and dilution zone.

4.8.1 Primary Zone

The main purpose of the primary zone is to achieve complete combustion of the air/fuel. Following Mattingly's and Lefebvre's methods, the thermodynamics of the primary zone were calculated. **Table 40** displays calculated parameters.

Table 40 : Primary Zone Thermodynamics

Parameter	Symbol	Value	Unit	Reference
Total Temperature at Primary Zone	$T_{T,PZ}$	4335.66	R	Calculated
Static Temperature at Primary Zone	T_{PZ}	4334.94	R	Calculated
Mach at Primary Zone	M_{PZ}	0.0312	/	Calculated
Number of Dilution holes	$\eta_{h,PZ}$	40	/	Melconian
Dilution Holes Mass Flow	m_{Hole}	2.04	lbm/s	Calculated

4.8.2 Secondary Zone

The main purpose of the secondary zone is to allow the flow to slowly cool down to avoid problems in the dilution zone. According to [13] the temperature to an intermediate level by the addition of small amounts of air encourages the burnout of soot and allows the complete combustion of all fuel. **Table 41** displays calculated parameters.

Table 41 : Secondary Zone Thermodynamics

Parameter	Symbol	Value	Unit	Reference
Total Temperature at Secondary Zone	$T_{T,SZ}$	3976.9	R	Calculated
Static Temperature at Secondary Zone	T_{SZ}	3976.2	R	Calculated
Mach at Secondary Zone	M_{SZ}	0.034	/	Calculated
Number of Dilution holes	$\eta_{h,SZ}$	20	/	Melconian
Dilution Hole Mass Flow	m_{Hole}	2.04	lbm/s	Calculated

4.8.3 **Dilution Zone**

According to [13], "The role of the dilution zone is to admit the air remaining after the combustion and wall-cooling requirements have been met, and to provide an outlet stream with a temperature distribution that is acceptable to the turbine". **Table 42** displays the calculated parameters.

Table 42 : Dilution Zone Thermodynamics

Parameter	Symbol	Value	Unit	Reference
Total Temperature at Dilution Zone	$T_{T,DZ}$	3700.0	R	Calculated
Static Temperature at Dilution Zone	T_{DZ}	3699.2	R	Calculated
Mach at Dilution Zone	M_{DZ}	0.034	/	Calculated
Number of Dilution holes	$\eta_{h,DZ}$	20	/	Melconian
Dilution Hole Mass Flow	m_{Hole}	2.04	lbm/s	Calculated

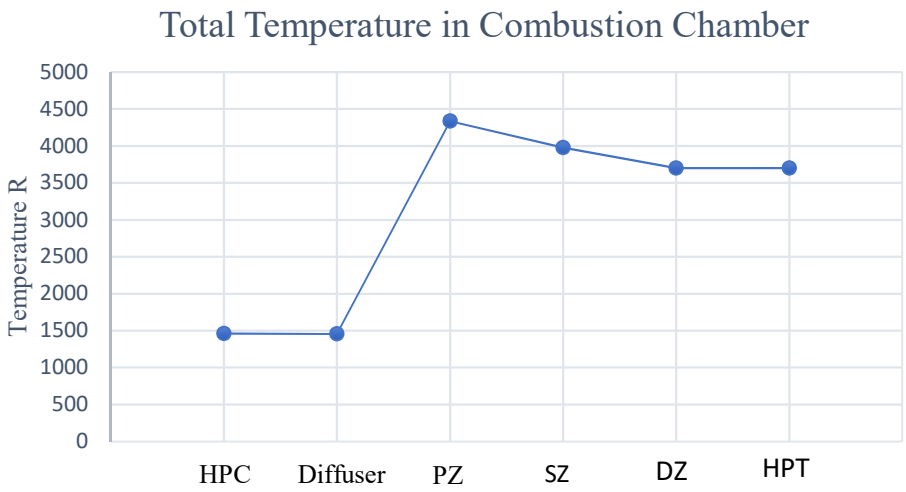

Figure 58: Total temperature Distribution through Main Burner

Figure 58 shows the total temperature distribution throughout the combustion chamber is clear. The temperature that enters the combustion chamber changes minimally as it goes through the diffuser. Afterwards as it reaches the primary zone, the fuel injectors add fuel, ignites and the temperature increases quickly. From the primary zone to the main burner exit, the flow cools down until it reaches the required TIT.

4.8.4 **Main Burner Exit/HPT Entrance**

The calculated parameters in the main burner exit are the same parameters that will go into the High-Pressure Turbine which will power the Compressor. They were calculated making use of the following thermodynamic equations. Having a target total temperature of 3700 [°R] and a target Mach number of 0.25, the static temperature can be calculated as shown below:

$$T = \frac{TIT}{\left[1+\frac{\gamma-1}{2}*M^2\right]} \tag{24}$$

With a pressure ratio of the burner of π = 0.96 and deducting 2% for duct losses, a total pressure can be calculated with equation (25).

$$Pt = [P_{T,3} * \pi_b] * 0.98 \tag{25}$$

$$P = \frac{Pt}{[1+\frac{\gamma-1}{2}*M^2]\hat{}[\frac{\gamma}{\gamma-1}]} \tag{26}$$

Finally, the mass flow rate coming out of the combustion chamber is obtained using equation (27):

$$\dot{m}_4 = \dot{m}_3 + \dot{m}_f \tag{27}$$

$$\dot{m}_f = \dot{m}_3 * f \tag{28}$$

Where f is obtained from cycle analysis and has a value of 0.03996. **Table 43** display these exit condition parameters.

Table 43 : Parameters Exiting the Main Burner

Parameter	Symbol	Value	Unit	Reference
Mach Number at Main Burner Exit	M_4	0.25	/	Calculated
Velocity at Main Burner Exit	V_4	698.72	ft/s	Calculated
Total Temperature at Main Burner Exit	$T_{T,4}$	3700	R	Calculated
Static Temperature at Main Burner Exit	T_4	3662.3	R	Calculated
Static Pressure at Main Burner Exit	P_4	185.56	psi	Calculated
Total Pressure at Main Burner Exit	$P_{T,4}$	193.39	psi	Calculated
Density at Main Burner Exit	ρ_4	0.1463	lbm/ft3	Calculated
Mass Flow at Main Burner Exit	m_4	212.06	lbm/s	Calculated
Area of the Main Burner Exit	A_4	297.60	in2	Calculated
Ratio of Specific Heats	γ_4	1.33	/	Calculated

5 Turbine design

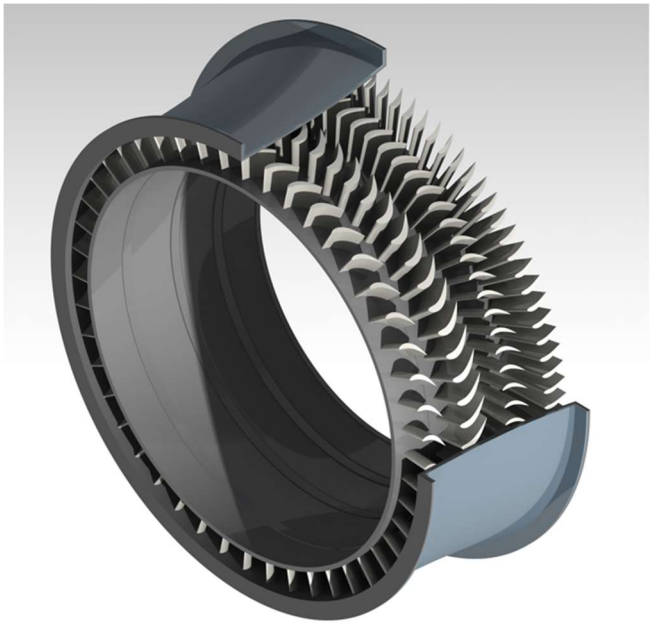

Figure 59: Turbine Isometric View

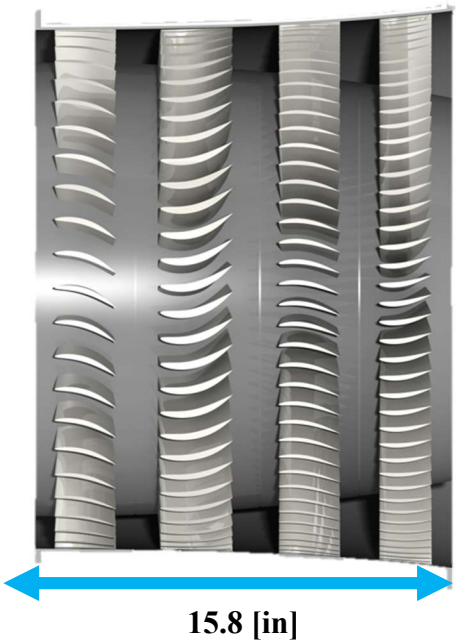

Figure 60: Turbine Side View

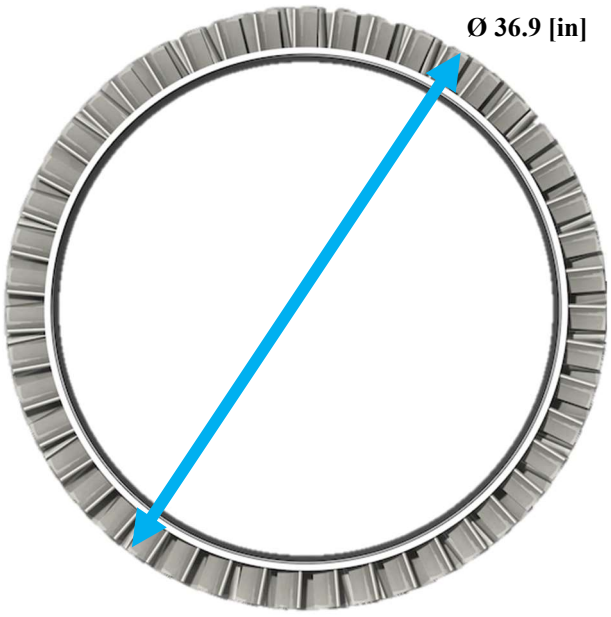

Figure 61: HPT Front View

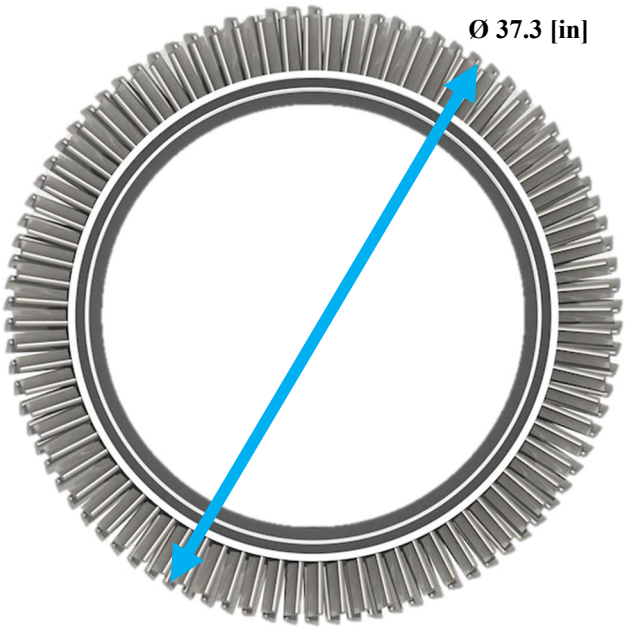

Figure 62: LPT Front View

The high-pressure turbine (HPT) and the low-pressure turbine (LPT) are designed as single stage components each to achieve a total enthalpy change of **146.3 (BTU/lbm)** and **82.9 (BTU/lbm)** respectively. Due to the high temperature in the turbine, C-CC's and CMC's were considered. Additionally, thermal barrier coatings (TBC's) were also considered for this design. TBC's are highly innovative materials applied to turbine blades to further protect the blades from severe thermal conditions. In general, turbine blades are subjected to very high temperatures, high levels of vibration, and very high stresses. All of these factors can be very devasting for the blades and can lead to an engine failure. Therefore, for this design, TBC's will be a necessary addition to the design to ensure extended life, reducing the overall life cycle cost, and to optimize the blades performance. **Figure 63** shows a comparison between two turbine blades.

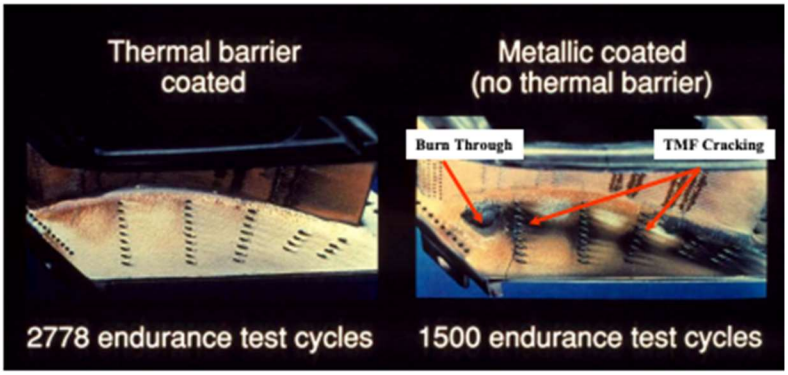

Figure 63: Blade endurance comparison [17]

5.1 Design Choices and Criteria

Table 44 lists the design choices for the two components as well as the criteria used.

Table 44: Turbine design choices and criteria

Parameters	HPT	LPT	Units/criteria
Stages	1	1	-
Δh_0	146.3	82.9	BTU/lbm
RPM	10158	6946	-
$\dot{m}_0$	212.1	212.1	kg/s
ϕ	0.8	0.8	[0.8-1.2]
λ	1.6	1.6	<2.2
η_{tt}	0.92	0.92	
Z	0.8	0.8	[0.8-0.9]
α_2	64°	54.3°	$< 72°$
Power Off-take	50	0	HP
η_M	0.98	0.996	Tech. Lvl. 5

The work extracted from the HPT and LPT only require one stage each power the HPC and LPC, respectively. The annulus of the turbine follows a third order polynomial curve fit to ensure smoothness and manufacturability. The HPT design incorporated a decreasing mean pitch line and an increasing axial velocity. The LPT follows a similar geometric trend, but the flow is decelerated to avoid the design of an inter-turbine duct; as shown in **Figure 64**.

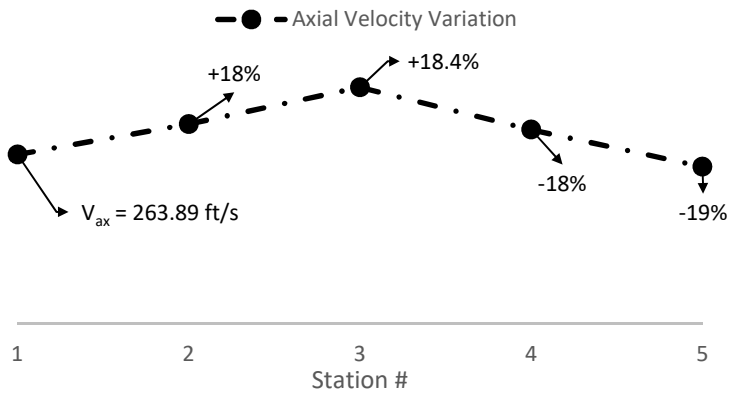

Figure 64: Axial velocity variation through the turbine

5.1.1 Flow Coefficient (φ) and Spool Speed

A higher φ led to smaller flow areas and higher axial velocities. The differences in spool speeds led to larger flow areas in the LPT, which was not ideal. To balance this challenge, a lower φ was selected. The flow areas would increase naturally, but this allowed the axial velocities to remain subsonic.

5.1.2 Stage Loading (λ)

λ is used to quantify the workload of a turbine stage. This dictated the amount of work extraction that a stage can handle and gave confidence that a single-stage design was feasible. A stage loading of 1.9 in the preliminary stages of the design (reasonable value because turbine blades accept much more loading without danger of BL separation) showed that the turbine stage was working harder than it needed to. This led to a reduction of λ in the HPT and LPT to balance the workload of each turbine with respect to their tangential velocity.

Additionally, a higher λ decreased the radial position of the turbines, which created conflict with mating the combustion chamber to the HPT. It is favorable for the combustion chamber to be either horizontal or tilted slightly upwards towards the HPT entrance. For this reason, a lower λ was utilized, which is a beneficial feature considering component life expectancy.

5.1.3 Adiabatic Efficiency (η_{tt})

η_{tt} of the stage was found using the Turbine Smith Chart [7]. **Figure 65** shows the efficiency for the turbine stages (92%). These values were used to obtain the pressure ratios for each turbine based on their respective temperature ratios.

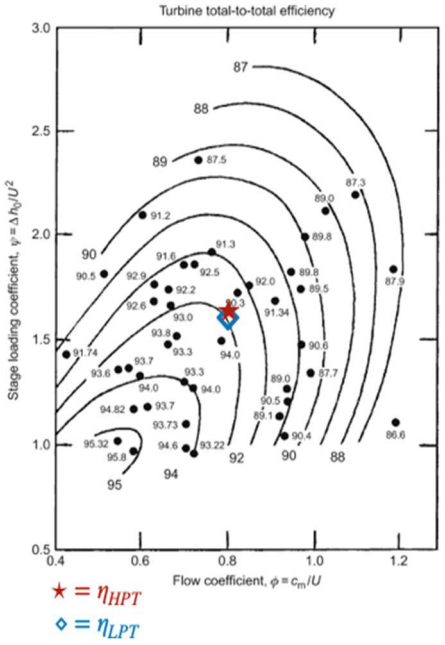

Figure 65: Turbine Smith chart [7]

5.2 Geometry

This section highlights all the geometrical parameters that were calculated during the design process and also explains the significance of each value. **Figure 66** shows the meridional view of the turbines with their respective station numbers.

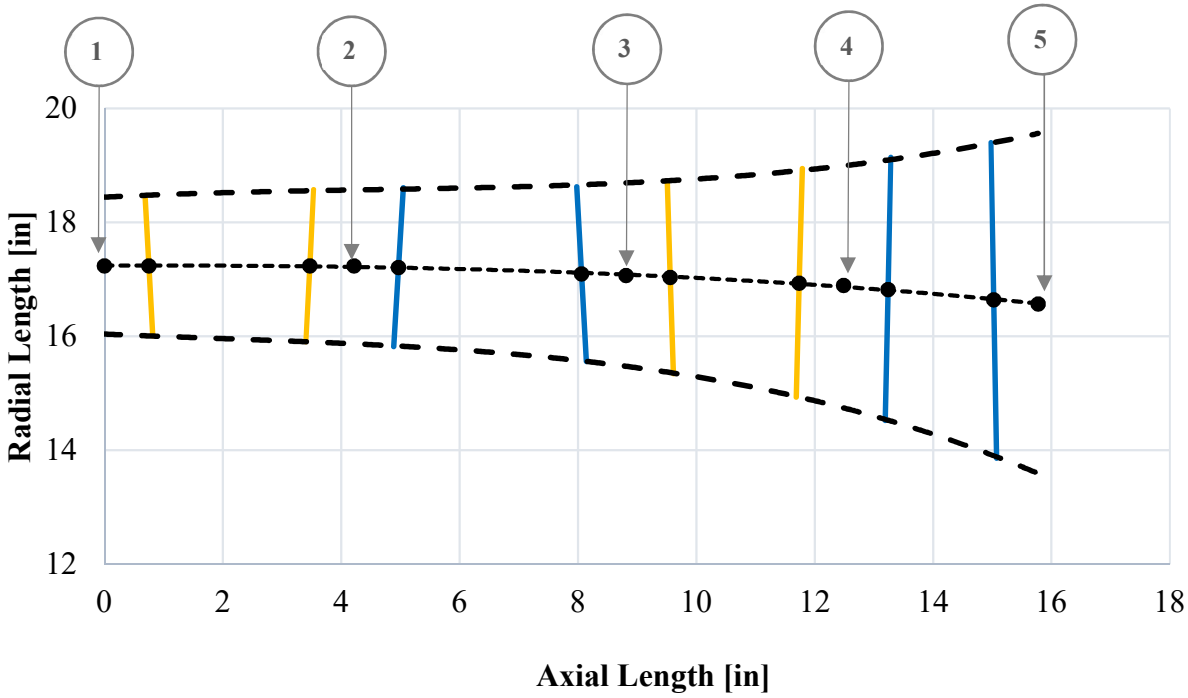

Figure 66: Turbine component meridional view [1:1]

5.2.1 Zweifel' coefficient (Z), Number of Blades (NOB), and Pitch (S)

NOB for each stage in the turbine increases from the first row of the HPT to the last row of the LPT. The NOB for each row is calculated at the mid-span location using the Zweifel Coefficient (Z). Because of high speeds in the turbine, there is always a risk for flutter and possible mechanical failure. Therefore, an optimum value of Z = 0.8 for all stations was selected. This value was then used with the flow angles (relative for rotors and absolute for stators) to find pitch at the mid-span location of the turbine using the equations shown below:

$$Z_{rotor} = 2\left(\frac{s}{C_{ax}}\right)\cos^2\beta_3(\tan\beta_2 - \tan\beta_3) \tag{29}$$

$$Z_{stator} = 2\left(\frac{s}{C_{ax}}\right)\cos^2\alpha_2(\tan\alpha_1 - \tan\alpha_2) \tag{30}$$

The value of pitch was then used to calculate the NOB at the mid-span location:

$$S_{mid} = \frac{2\pi r_{mid}}{NOB} \tag{31}$$

Table 45 contains the NOB and S at an optimum value of Z = 0.8 at the mid span location of the turbine. All other geometric parameters can be found in **Table 62** in Appendix C.

Table 45: S and NOB for turbine stages

Stage #	Stator		Rotor	
	NOB	S [in]	NOB	S [in]
1	40	2.71	56	1.93
2	69	1.60	86	1.23

5.3 Thermodynamics

Figure 67 shows the thermodynamic property variation throughout the turbine.

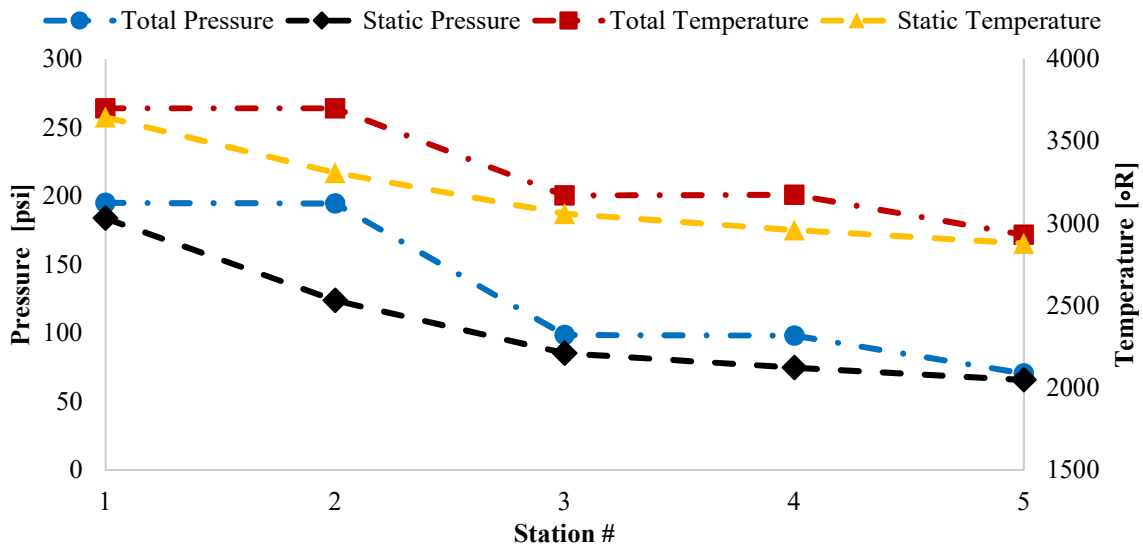

Figure 67: Variation of thermodynamic properties through the turbine

The decreasing trend of total/static temperatures and pressures are due to the work extraction in the turbine as shown in **Figure 67**. This energy is converted to mechanical power to drive the LPC and the HPC. The total temperature across the stator remains constant with a small drop in the total pressure due to losses from the presence of a boundary layer and quantified by the stator loss coefficient ($\zeta_{Stator} = 0.04$). This represents adiabatic expansion with no work as the stator's purpose is to accelerate flow by adding swirl, while stationary. The total temperature and total pressure drop significantly through the rotors due to the work extraction.

5.3.1 HPT

Table 46 shows the thermodynamic state variation through the HPT.

Table 46: Thermodynamic State Variation for the HPT

Parameter	Entrance	Exit	Δ
P_0 [psia]	195.0	98.82	96.19
T_0 [°R]	3700	3171.7	528.3
h_0 [BTU/lbm]	1008.1	845.9	146.4
ρ [lbm/ft^3]	0.136	0.0754	0.0606

5.3.1.1 h-s diagrams

To better show the thermodynamic variation through the HPT, representative h-s diagram for the stage is shown in **Figure 68**. The figure shows the HPT stage in the Absolute Frame of Reference ("F.O.R.").

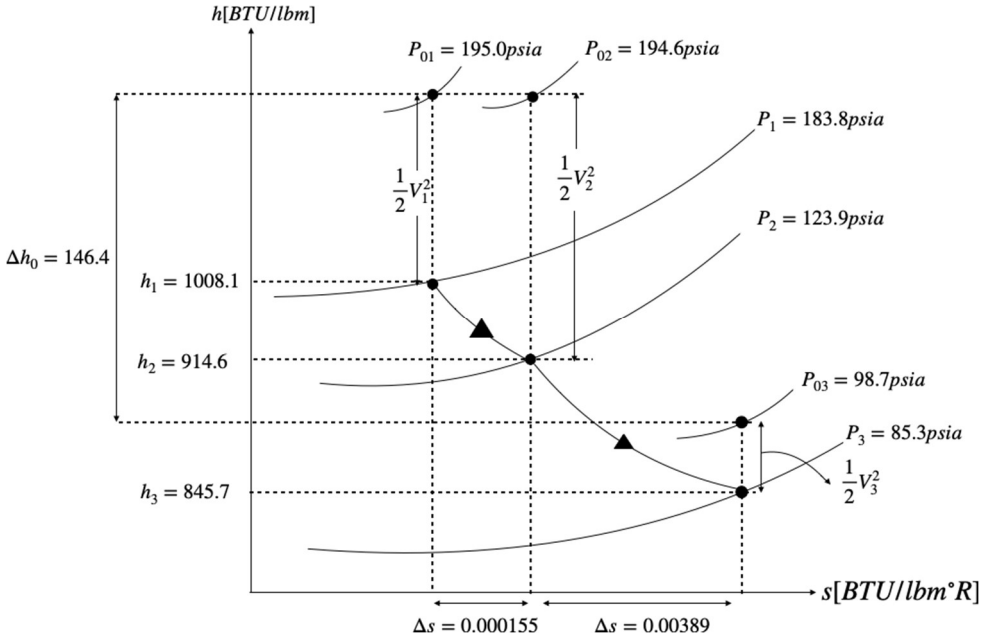

Figure 68: HPT stage in Abs. F.O.R.

The h-s diagram for the HPT shows that a total specific work of 146.4 BTU/lbm is needed to power the HPC. This shows that the HPT needs to extract an additional 2.2% of mechanical power in order to account for all losses due to mechanical inefficiencies and power take-off. The power required by the HPT was calculated to be 43,888 HP to power the HPC.

5.3.2 LPT

Table 47 shows the thermodynamic state variations through the LPT stage.

Table 47: Thermodynamic state variation through LPT

Parameter	Entrance	Exit	Δ
P_0 [psia]	98.8	70.7	28.1
T_0 [°R]	3171.7	2931.5	240.2
h_0 [BTU/lbm]	876.9	794.0	82.9
ρ [lbm/ft^3]	0.0754	0.0618	0.0135

5.3.2.1 h-s diagrams

Figure 69 shows the representative h-s diagram of the LPT.

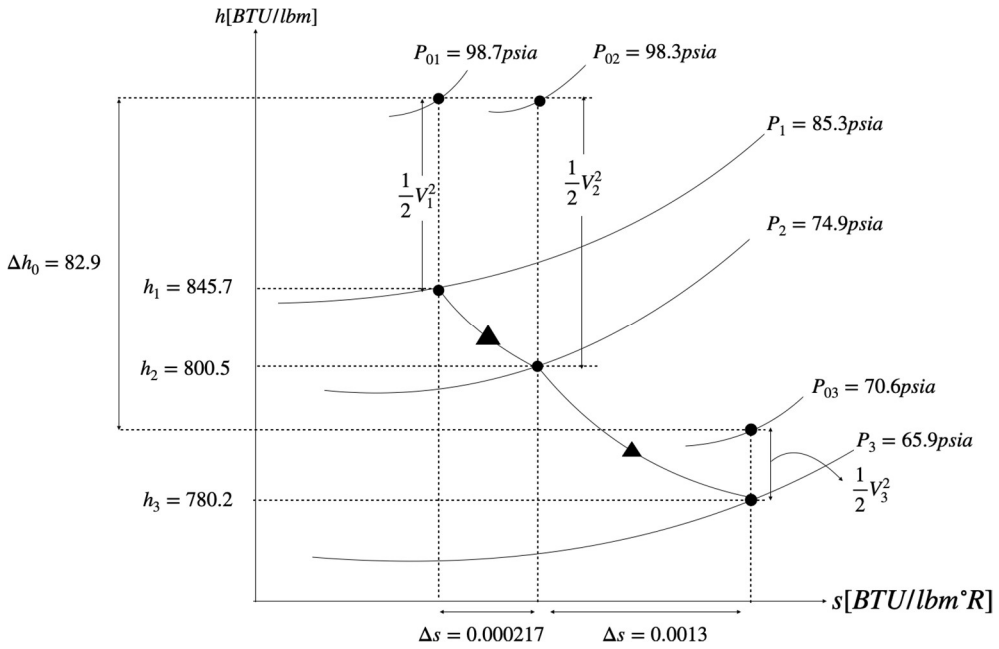

Figure 69: LPT stage in Abs. F.O.R.

The h-s diagram for the LPT shows that a total specific work of 82.9 BTU/lbm is needed to power the LPC. This shows that the LPT needs to extract an additional 0.4% of shaft power in order to account for all losses due to mechanical inefficiencies. The power produced by the by the LPT was 19339 HP.

5.4 Aerodynamics

5.4.1 Mach Number Variation

For this design, the flow comes into the turbine cascade with a Mach Number of 0.3 and 0° of swirl. Since the stator imparts swirl and adds kinetic energy to the flow, the highest absolute Mach number was recorded at the exit of the 1st stage stator at 0.907 at the hub. **Figure 70** shows all exiting absolute Mach numbers leaving the stators satisfy the criteria of $M \leq 1.2$ which was set as a self-imposed design constraint to mitigate excessive losses.

The relative and tangential Mach numbers followed a similar criterion. The relative Mach numbers leaving the rotors were highest at the tip, common with Free Vortex solutions for radial equilibrium. For this design the highest relative Mach number was calculated to be 0.862 at the tip of the HPT rotor. **Figure 71** shows all exiting relative Mach numbers calculated for this design.

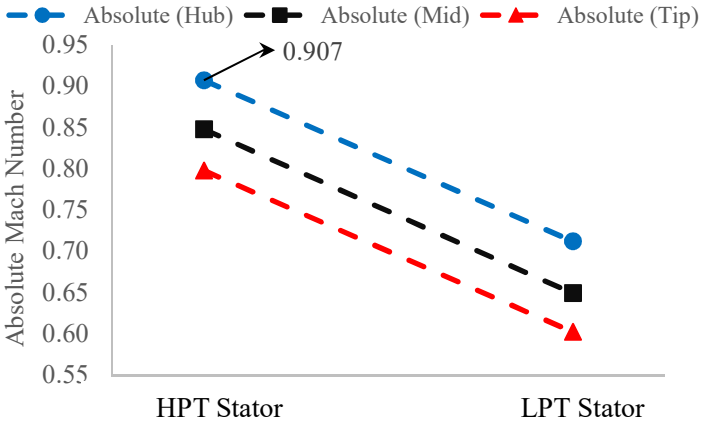

Figure 70: Exiting Absolute Mach Number Variation

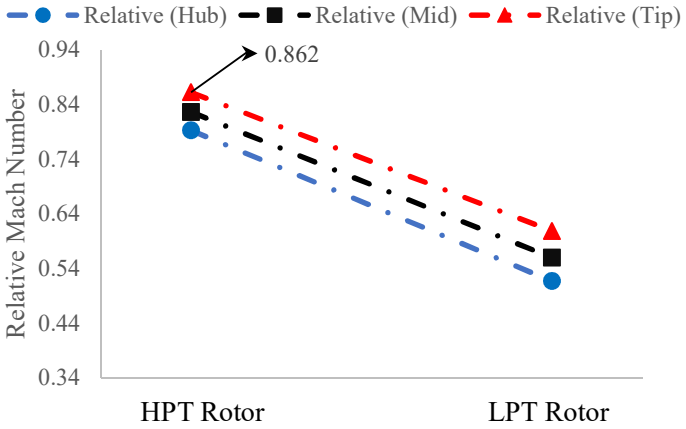

Figure 71: Exiting Relative Mach Number Variation

5.4.2 Flow Angle Variation

Similar to the Mach numbers, the flow angles had set self-imposed criteria. All the flow angles (α and β) were kept below 72° to avoid excessively large velocities and to ensure the Mach number criteria was satisfied. Additionally, all total turning angles (Δα and Δβ) were kept below 120°.

For this design, α_2 was a critical design choice to bridge the gap between the entrance and the exit of either the HPT or LPT stage as this angle determines the required turning of the flow by the stator. Since the axial velocity was a design choice, choosing α_2 helped in finding the absolute velocity and finally complete the respective velocity triangle. This flow angle selection also affected the $°R$ for the stage at the hub, mid, and tip locations so an optimum value of α_2 was chosen for both the HPT and LPT to satisfy all criteria and also maintain a healthy stage. **Figure 72** and **Figure 73** show all total turning angles ($\Delta\alpha_{stator}$ and $\Delta\beta_{rotor}$) for the turbine.

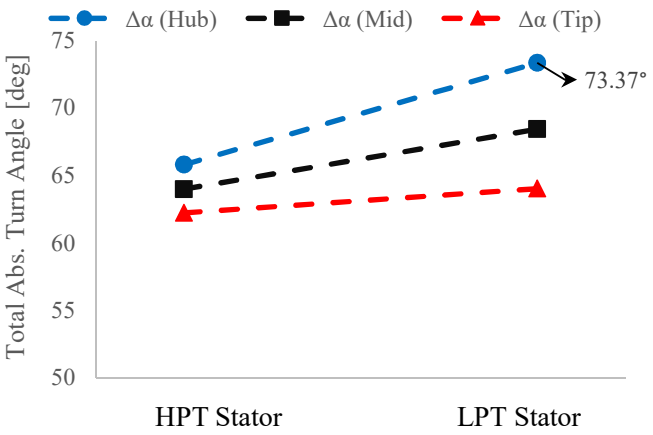

Figure 72: Absolute Total Turn Angle

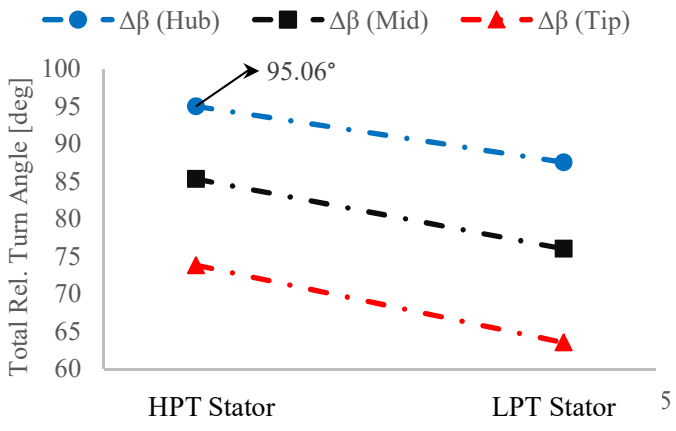

Figure 73: Relative Total Turn Angle

5.4.3 HPT

Table 48 shows aerodynamic variable variations at the mid-span through the HPT stage.

Table 48: Aerodynamic State Variation, Entering Values

Parameter	Stator 1	Rotor 1	Exit
α [°]	0.0	64.0	14.1
β [°]	0.0	29.0	56.3
$\mathbf{V_{ax}}$ [ft/s]	865.8	1021.6	1210.3
$\mathbf{V_u}$ [ft/s]	0.0	2094.7	305.0
V [ft/s]	865.8	2330.5	1248.1
W [ft/s]	0.0	1168.3	2183.9
U [ft/s]	0.0	1528.0	1512.9

5.4.3.1 Velocity Triangles

Figure 74 shows a cascade view for the HPT stage at the mid-span location. The purpose of this figure is to provide the reader with the aerodynamics of the HPT and a sense of relative scale.

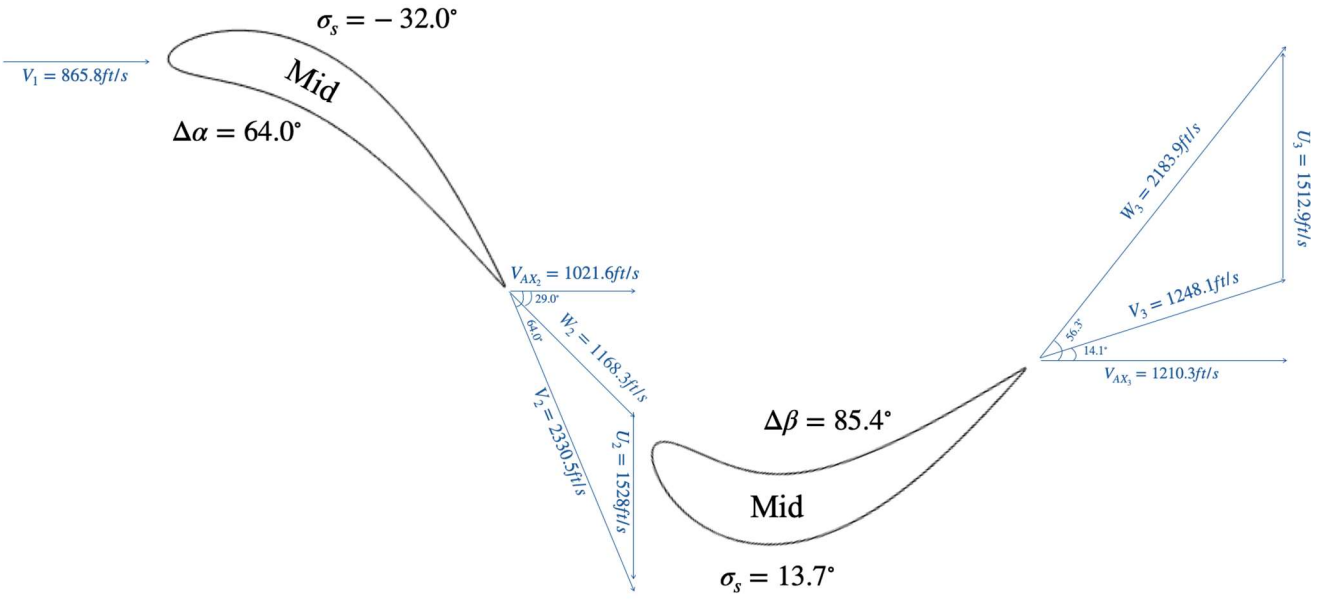

Figure 74: HPT stage cascade view (Mid)

5.4.4 **LPT**

Table 49 shows the aerodynamic variable variations through the LPT stage at the mid-span location.

Table 49: Aerodynamic State Variation, Entering Values

Parameter	Stator 2	Rotor 2	Exit
α [°]	14.1	54.3	13.9
β [°]	56.3	19.8	56.3
$\mathbf{V_{ax}}$ [ft/s]	1210.3	992.4	803.4
$\mathbf{V_u}$ [ft/s]	305.0	1381.1	198.4
V [ft/s]	1248.1	1700.7	827.5
W [ft/s]	2183.9	1054.7	1446.3
U [ft/s]	1512.9	1024.2	1004.3

5.4.4.1 Velocity Triangles

Figure 75 shows LPT stage cascade view at the mid-span location.

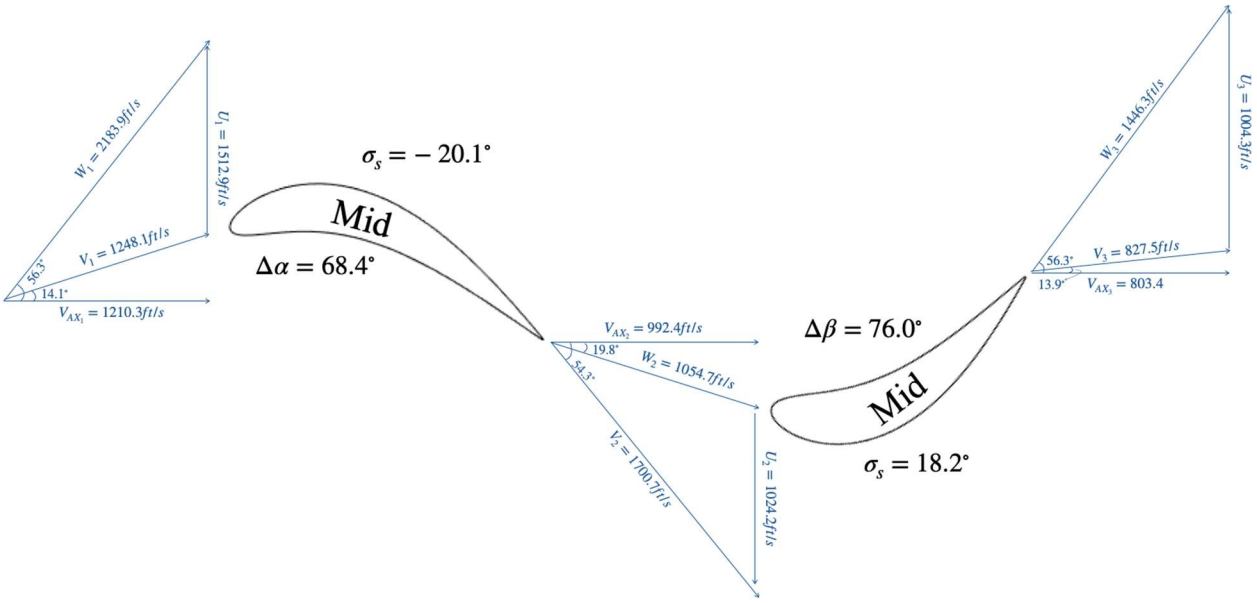

Figure 75: LPT stage cascade view (Mid)

5.4.5 Turbine Health Assessment

5.4.5.1 Degree of Reaction (°R):

Unlike the compressors, the turbines work with a favorable pressure gradient with a much lower risk of BL separation. Therefore, for the health assessment only the °R was taken into consideration. Additionally, for turbines °R is most important at the hub of the rotor. According to Farokhi [9], if °R goes below 10%, the off-design performance of the stage can be at risk. Hence, for this design all the °R were kept above the 10% criterion. **Figure 76** shows the variation of °R for the two turbine stages.

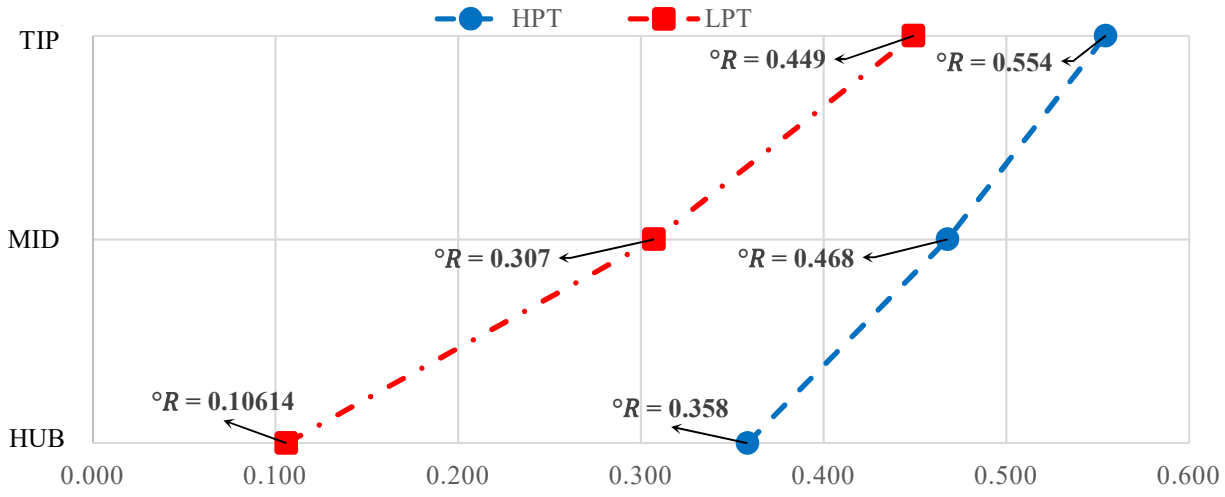

Figure 76: Degree of Reaction for the Turbine stages

5.5 Turbine Exit Diffuser

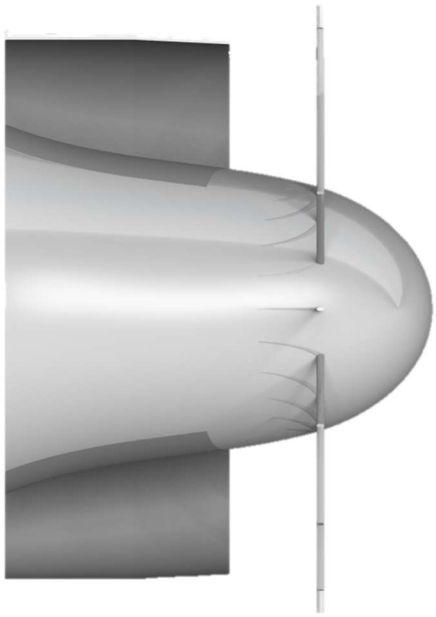

Figure 77: Turbine Exit Diffuser Isometric View

The flow leaves the LPT rotor at a Mach number of 0.345 and a swirl angle of $\alpha = 6°$, at the mid-span. The flow at the exit location is mostly axial with the majority of swirl removed and the axial Mach number constant at the hub, mid, and tip locations. Per the requirements from GasTurb cycle analysis, the flow leaving the LPT must be decelerated before passing the flame holders of the ramjet. The turbine exit diffuser was designed to slow the flow to a Mach number of 0.25.

5.5.1 Dimensioning

The diffuser was designed using a model explained by Mattingly [8]. By applying conservation of mass principles and assuming that area decreases linearly from station 6A to m, the following approach can be taken. Station numbering can be referenced in **Figure 78** for the explanation.

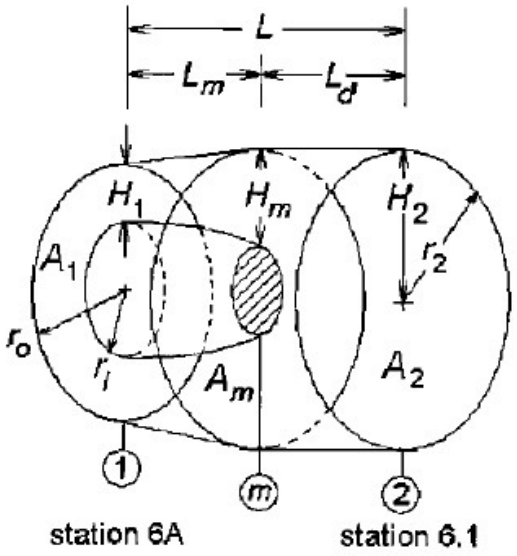

Figure 78: Annulus flat-wall diffuser geometry [8]

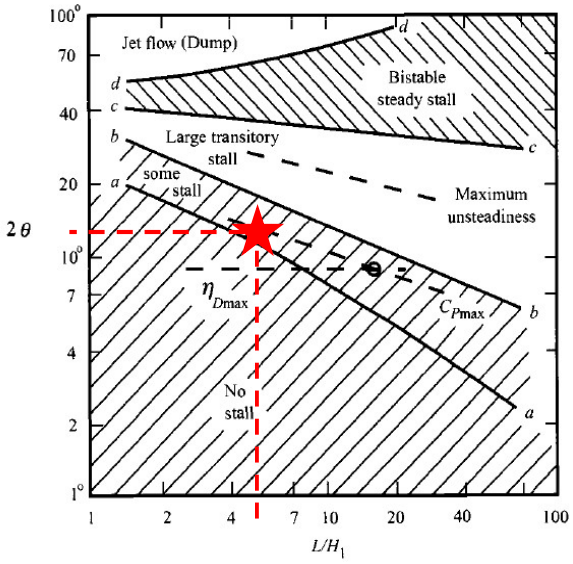

Figure 79: Flat-wall diffuser operating limits [8]

The outer radii and area at station 6A is fixed from the LPT design, therefore, the outer radius at station m and 6.1 is selected. The inner radius and area at station m are found using the following definitions [8]:

$$r_0(x_m) = r_{0,1} + \left(\frac{r_2 - r_{o,1}}{L_m}\right)(x_m - x_1) \tag{32}$$

$$\frac{A(x_m)}{A_1} = 1 + \frac{r_{mm}}{r_{m1}}\frac{(x - x_1)}{H_1}\,2\tan(\theta) \tag{33}$$

Here, θ is defined as the divergence angle. The optimum angle is found using **Figure 79** and it lies in the "some stall" region. Mattingly says, "In the 'no stall' region below curve a-a, flow remains attached to the walls, but performance is suboptimal because of excessive friction resulting from very long walls." For this reason, a θ of 7° was selected and is represented in **Figure 79**. This selection led to calculating the length of the diffuser, 33.5 [in].

6 Ramjet Design

The ramjet is designed in order to achieve the requested max Mach number of 3.0. Therefore, the ramjet will only be active during this flight condition. **Figure 80** shows the conceptual operation of the ramjet when the turbojet is not in operation.

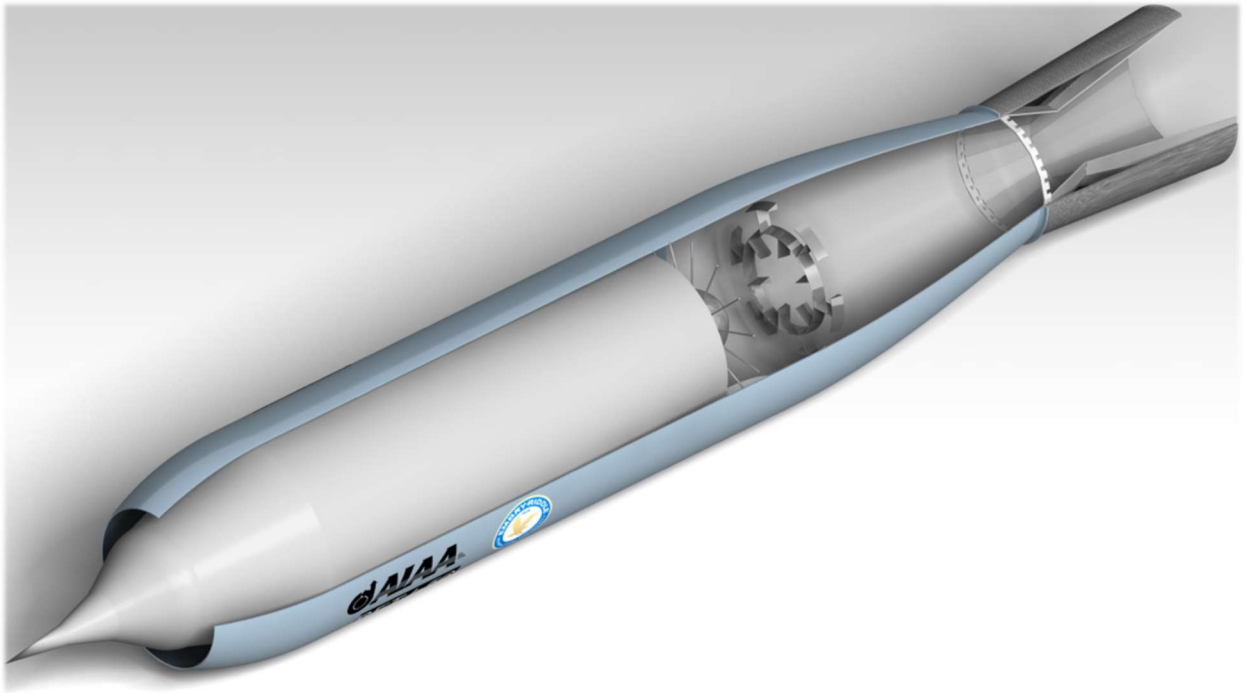

Figure 80: Ramjet isometric view

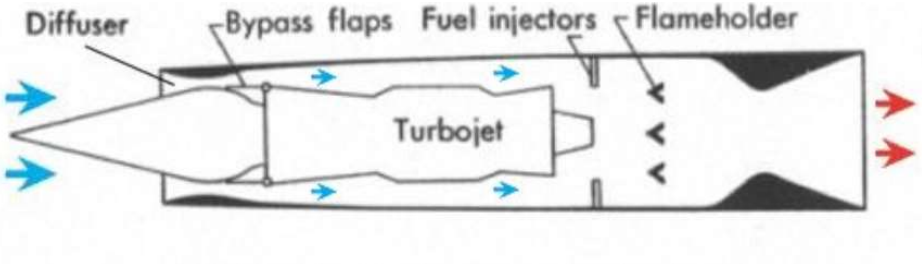

Figure 81: PW-J58 turboramjet architecture with bypass flaps closed

6.1 Geometry

The ramjet architecture is a simple one as seen in **Figure 81**. It consists of the bypass duct (modeled as a diffuser), a burner (afterburner in this case), and a nozzle. The duct is 134.2 [in] long, the entire length of the turbojet. The diffuser

decelerates the flow in the bypass duct from a Mach number of 0.643 to 0.2. This is done to satisfy the velocity constraints at the entrance of the flame holder, where the Mach number should not exceed 0.2 to prevent a flame-out.

The duct height is 2.49 [in]. This was calculated using the principles of mass conservation based on the required mass flow and flow properties at the entrance of the duct. **Table 50** shows the flow properties entering the duct.

Table 50: Ramjet bypass duct entering flow properties (exit of terminal shock of inlet)

$\dot{m}_2$ [lb_m s^{-1}]	V [ft s^{-1}]	ρ_2 [lb_m ft^{-3}]	P_0 [psi]	T_0 [°R]	A_2 [in^2]
154.3	1000.7	0.0625	30.8	1091.9	**355.39**

Applying the following relationship and the given radii of the turbojet, the tip and hub radius of the ramjet can be found. Here the hub radius of the ramjet is also known to be the tip radius of the turbojet, 21.504 [in].

$$A = \pi\left(r_{tip}^2 - r_{hub}^2\right) \tag{34}$$

$$r_{tip} = \sqrt{\frac{A}{\pi} + r_{hub}^2} = \sqrt{\frac{355.39}{\pi} + 21.504^2} = 23.99 \text{ [in]}$$

This result yields a max ramjet diameter of 47.98 [in]. This diameter is 1.22 [in] (~2.5%) smaller than the max allowed constraint given by the RFP. It should be noted that the "State-of-the-art" and "Goal" assumption is relevant to the year 2002. Therefore, the burner duct L/D of the BFTJ is 2.0 with the total length of the burner being 96 [in].

6.2 Technology Limitation

The entry into service date of 2030 led to the assumption that the technology available will be "State-of-the-art". With this assumption, the L/D of the afterburner section is 2.5 [8] as shown in **Figure 82**. This length ensures that the flame will be completely captured and stable within the burner duct.

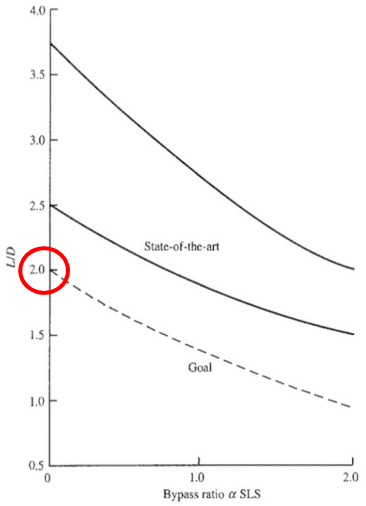

Figure 82: Technology limitations on afterburner length [8]

6.3 Thermodynamics

The total temperature (T_{t7}) for the AB is 3900 [°R]. This assumption is based on the technology level 5 limiting T_{t7} to 4000 [°R] [8] [13]. When the turbojet is in operation, the afterburner duct is represented as adiabatic expansion with no work. Therefore, at this condition $T_{t5} = T_{t7}$.

The total PR of the afterburner when active is dictated by the FOM, π_{AB} = 0.96. This FOM accounts for the mixing and burning efficiencies of the burner. However, when inactive, the duct is assumed to have $\pi_{AB} = 0.99$, a 1% loss in P_0. The thermodynamic process for the ramjet is shown in **Figure 83**.

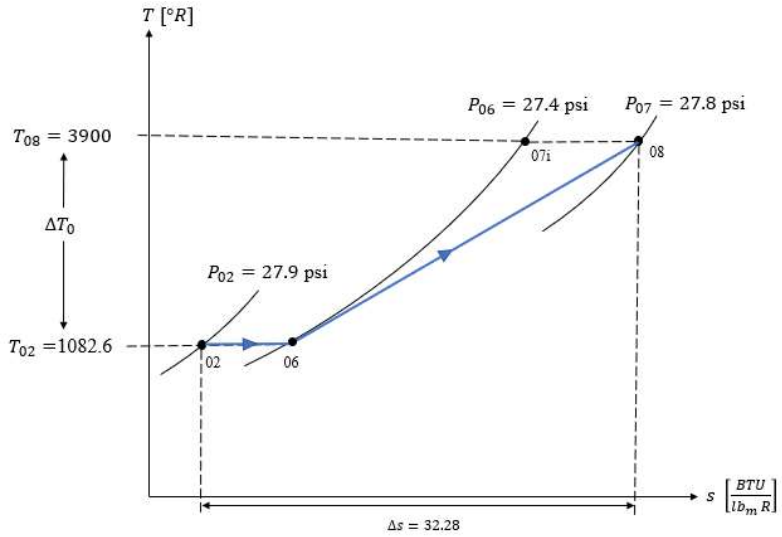

Figure 83: Afterburner T-s diagram, ramjet operation

7 Nozzle Design

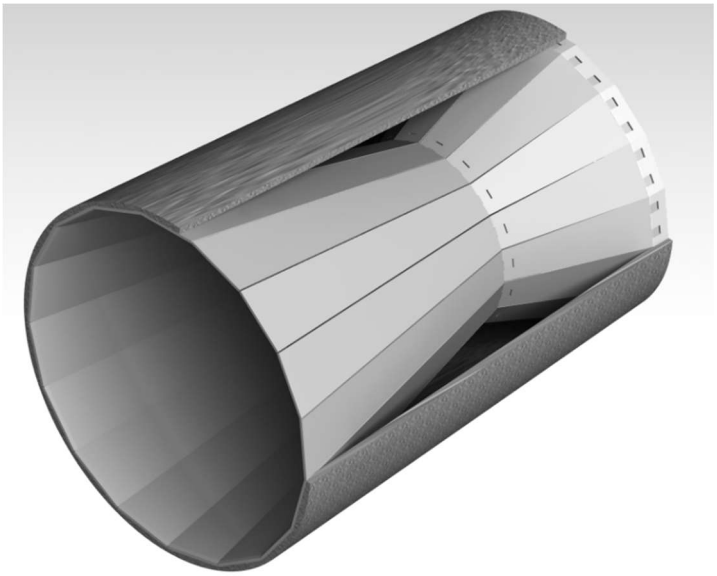

Figure 84: Isometric view of Nozzle

The nozzle is designed to be convergent-divergent with variable geometry. Variable geometry will adjust the throat area and exit area with the goal of maximizing thrust. Though performance is to be maximized, marginal losses in thrust will occur due to implementing variable geometry. A bell-shaped divergent section was considered to prevent any losses in axial thrust. Although it is necessary, it should be noted the implementation of variable geometry is much more costly than that for a fixed geometry design.

7.1 Design Constraints

The boundary conditions for the design is reference flight conditions at max dry power. These boundary conditions are summarized in **Table 51.** These values are referenced from on-design cycle analysis at maximum dry power. The geometry, displayed in the next section, was determined by a thermodynamic analysis of the component using the given boundary conditions.

Table 51: Boundary Condition for Nozzle Design

π_n	**0.98**
T_{t7} [°R]	3026.5
P_{07} [psi]	69.8
$\dot{m}_7$ [lb_m/s]	212.07
M_7	0.22
A_7 [ft^2]	0.514
P_9/P_0	1

7.2 Geometry

Figure 85 illustrates the geometry of the nozzle during on-design operation at maximum dry and wet power. The dimensions for the horizontal lengths from station 7 to 8 and station 8 to 9 and nozzle inlet area is held fixed. The dimensions that change are the throat and exit areas. The throat area is adjusted to account for the differences in density at the throat during different throttle settings. During ramjet operation, the temperature increases significantly leading to a decrease in density. For a choked throat to pass approximately the same mass flow as that for no afterburner operation, the throat area must increase [9].As displayed in **Figure 85**, the throat area is larger for wet power than for dry power.

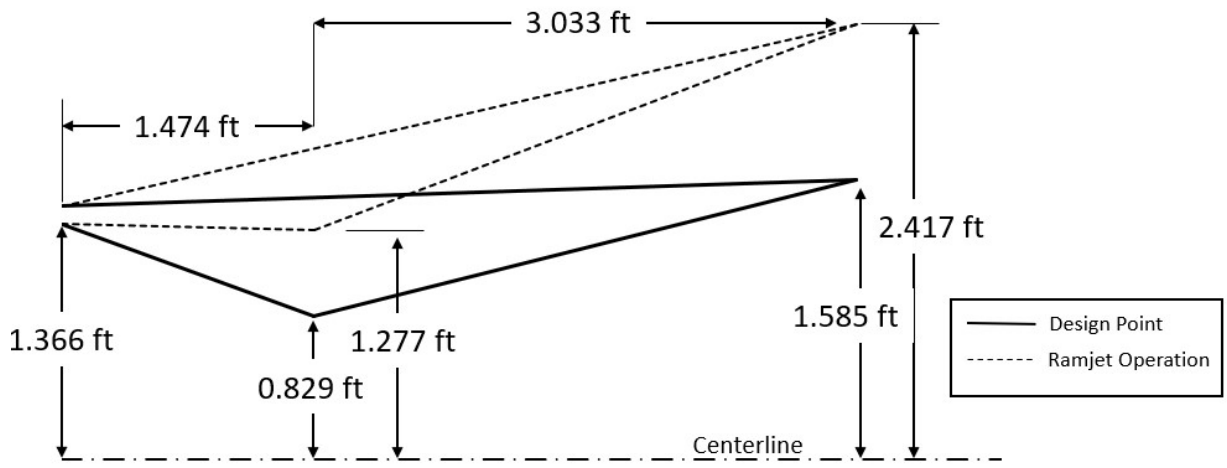

Figure 85: Dimensioned drawing of nozzle for both wet and dry power

Variable geometry is needed to control the exit area to make the nozzle perfectly expanded. Perfect expansion will maximize the jet velocity at the exit without incurring losses from a difference in pressure due to over expanding.

7.3 Thermodynamics

The thermodynamics for the on-design conditions at maximum wet power are displayed in **Figure 86**. The nozzle perfectly expands the flow to a static pressure of 2.73 psi yielding an exit velocity V_9 = 4647.4 ft/s (M_9 = 2.724). This corresponds to a thrust of 30632 [lbf].

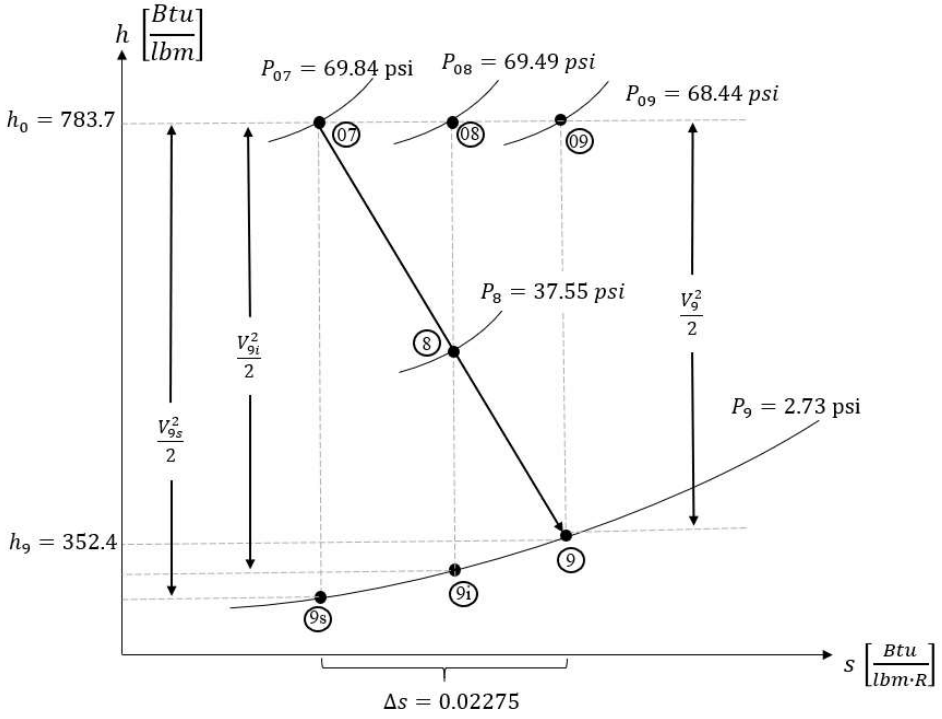

Figure 86: Nozzle h-s diagram (Wet Power)

7.4 Performance

The performance of the nozzle is assessed by minimizing the loss in thrust due to any vector components of the exit velocity not in the axial direction. The length of the nozzle was also considered for performance. An infinitely long cone, for the divergent portion, will incur no losses in jet thrust, but is not applicable. **Figure 87** illustrates the areas of losses incurred within a convergent-divergent nozzle.

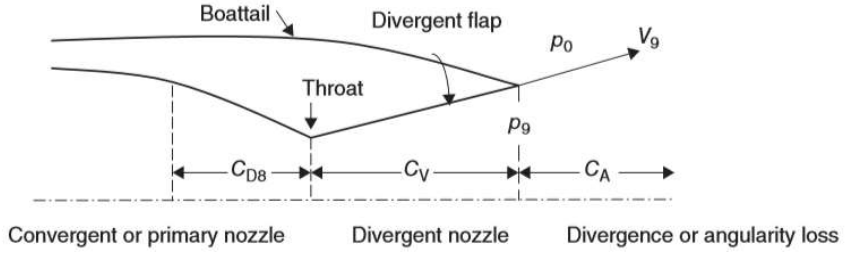

Figure 87: Flow losses of convergent-divergent nozzle [Farokhi, 9]

The losses within the divergent portion are caused by viscous flow losses. By observing the h-s diagram in **Figure 86**, the ideal velocity (V_i) is achieved only if the divergent portion of the nozzle was expanded isentropically [Farokhi, 9]. This loss coefficient is given by the ratio of actual exit velocity over this ideal exit velocity.

$$C_V = \frac{V_9}{V_{9i}} \tag{35}$$

The losses at the exit plane of the nozzle are caused by the angularity of the exhaust and is assessed by the divergence correction factor given by the following equation.

$$C_{A\,\text{conical}} = \frac{1 + \cos(\alpha)}{2} \tag{36}$$

The gross thrust coefficient is given by the following equation.

$$C_{fg} = C_{D8} C_V \frac{V_{9i}}{V_{9s}} \left[C_A + \frac{\frac{\gamma - 1}{2\gamma}\left(1 - \frac{P_0}{P_9}\right)}{\left[\left(\pi \frac{P_{07}}{P_0} \frac{P_0}{P_9}\right)^{\gamma - \frac{1}{\gamma}} - 1\right]} \right] \tag{37}$$

The actual jet thrust is given by the following relationship between ideal jet thrust and the gross thrust coefficient.

$$F_{g-actual} = C_{fg} F_{g-ide} \tag{38}$$

The nozzle performance for different flight conditions is summarized in **Table 52. Figure 88** displays the locations for parameters calculated for the nozzle.

Table 52: Geometry and nozzle performance for perfect expansion

Mach	Alt [kft]	T_{t7} [°R]	θ [°]	α [°]	A_8[ft^2]	A_9 [ft^2]	A_9/A_8	C_{fg}	F_{lost} [lbf]
1.6	40	3026.5	20.0	14.0	2.16	7.90	3.655	0.9783	604.8
2.1	40	2948.1	20.6	17.6	2.08	9.88	4.754	0.9705	1188.0
1.15	40	2419.9	20.1	9.3	2.15	5.51	2.558	0.9747	334.1
0.98	40	1037.8	19.8	4.6	0.20	0.34	1.667	0.9872	279.1
3	60	3900.0	2.7	20.3	5.28	18.35	3.479	0.8553	3770.4

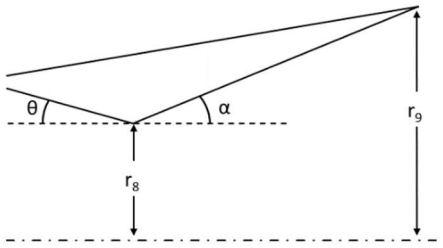

Figure 88: Parameter locations

The losses incurred by perfectly expanding the nozzle at Mach 3 are far greater than that suffered at all other flight conditions. This requires further analysis to find the ideal exit area that maximizes the jet thrust from both the pressure difference at the exit and the jet velocity. The ideal thrust is obtained by maximizing the following equation by adjusting A_9, which will affect P_9, V_9, and thrust loss.

$$F_{jet} = (P_9 - P_0)A_9 + \dot{m}_7 V_9 - F_{loss} \tag{39}$$

For some flight conditions, perfect expansion may not lead to the maximum thrust output. By over expanding the flow, the velocity becomes greater than that from perfect expansion, but losses are incurred due to a pressure at the exit less than ambient pressure. During under expansion, the velocity decreases while the pressure at the exit is greater than ambient pressure.

8 Airworthiness and Secondary Systems

The following chapter introduces and describes engineering standards applied to the presented design. Referenced in this section is the FAA Code of Federal Regulations (CFR). To be specific, only 14 CFR Part 33 and Part 36 are mentioned. Airworthiness is a top priority for the design as well as safety and protection of the environment in which the engine will operate.

8.1 14 CFR Part 33 – Airworthiness Standards: Aircraft Engines

8.1.1 Fire Protection (33.17)

In accordance with 14 CFPR 33.17 at any given flight condition, the engine must be designed and constructed with materials that minimize the occurrence and spread of fire. In addition, the design and construction of turbine engines must minimize the probability of the occurrence of an internal fire that could result in structural failure or other hazardous effects. Certain measurements to prevent fire throughout the engine include having components which contain or convey flammable fluid during normal engine operation, to be fire resistant and fireproof. **Figure 89** illustrates the flammable fluid leakage zone, fire zone and most importantly the fire wall for a commercial engine.

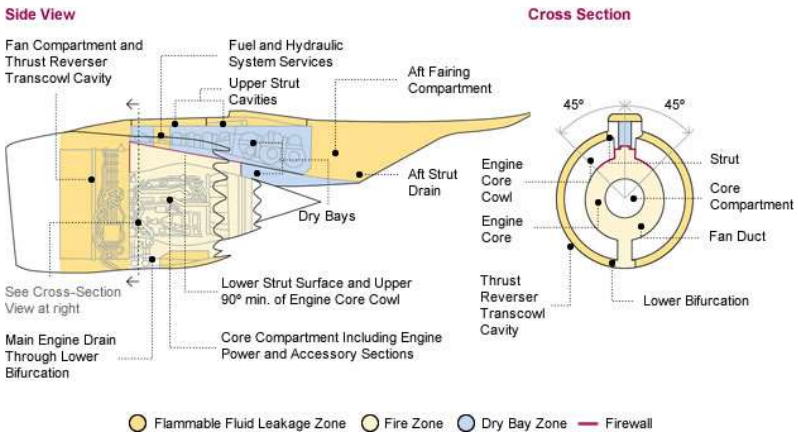

Figure 89: Fire Protection

8.1.2 Stall and Surge Characteristics (33.65)

In accordance in 14 CFR 33.65 when the engine is starting, changing power/thrust, or becomes exposed to different inlet mass flow/air temperature, it must not stall or surge to the extent of flameout in the burner, structural failure of the components, overheating, or failure of engine to recover thrust. Certain measures to prevent compressor surge/stall include variable compressor vanes and bleed valves. The incorporation of variable inlet guide vanes (VIGV) and

variable stator vanes (VSV) can allow for efficient and safe operating performance. As the RPM of the compressor slows down the vanes close giving the rotor a smaller relative velocity. As the shaft speed of the compressor increases, the vanes open giving the rotors a larger relative velocity [Gunston]. VIGV and VSV operate in the same manner. They control the angle at which the flows enter the rotor and therefore the relative velocity that the rotor experiences. These guide vanes are driven via shortly levers connected to a surrounding ring. **Figure 90** illustrates the mechanical side of implementing variable compressor vanes.

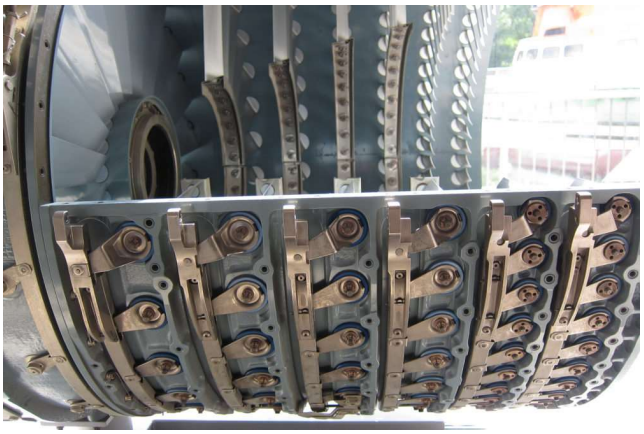

Figure 90: Depiction of mechanical side of VIGVs and VSVs

Another mechanism to prevent compressor surge is through the use of bleed valves. During off design performance the compressor can either receive more or less mass flow than it was designed for. The fluctuation in mass flow affects the axial velocity of the flow and therefore affects the angles at which the flow strikes the blades. During a mission leg that requires less mass flow than the design point, bleed valves would be opened to extract the extra mass flow and control the axial velocity inside compressor. The primary reason for incorporating bleed valves at start up - or at low speeds – is to prevent stall at the inlet of the compressor [Gunston].

8.1.3 Bleed Air System (33.66)

In accordance with 14 CFR 33.66 design and construction of the engine must be so that it provides bleed air without having any adverse effects on the engine. For obvious reasons there is one exception; the engine must be designed to have bleed air without any adverse effect including reduced thrust or power output. Following 14 CFR 33.66 the BFTJ was designed to have bleed airports after the HPC and before the Main Burner. **Figure 91** illustrates the location and flow of the bleed air system.

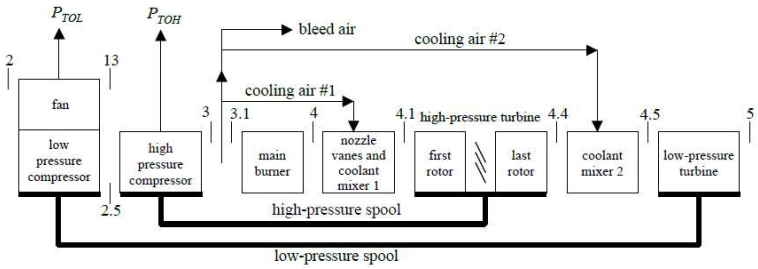

Figure 91: Bleed Air System

8.2 14 CFR Part 36 – Aircraft Noise Levels

8.2.1 Blade Frequencies

The design of the LPC led to high flow tip speeds and high blade rotational speeds. High blade rotational speeds are correlated with strong shock waves and vibrational stresses. In addition, the high blade rotational speeds have high passing frequencies when a row of rotating blades (rotors) interact with the stationary blades (stators). The passing frequencies are calculated as follow:

$$\mathrm{f_{Hz}} = \frac{\mathrm{RPM}}{60} * \mathrm{NOB} \tag{40}$$

Table 53 shows the passing frequencies for the three stages in the LPC. Research has shown the human ear is sensitive to certain frequency ranges. Keeping in mind that this proposed engine will enter service for a SJ, sound emission is a critical topic of research for the design.

Table 53: Rotor passing frequencies

RPM: 6945	**Rotor 1**	**Rotor 2**	**Rotor 3**
NOB	27	40	56
$\mathbf{f_{Hz}}$	3125.6	4630.5	6482.6

Figure 92 comes from a Penn State University Mechanical and Nuclear Engineering paper on *Human Response to Sound*. [5] It shows that, independent of sound intensity, the human ear is less sensitive to the frequency range between 2 kHz and 5 kHz. From the values above, the first rotor would emit sound frequencies within this range. This rotor is the most important as it is the rotor closest to the nacelle entrance and most likely to propagate audible noise to the far-field. The second and third rotor, could potentially operate at a disturbing frequency and are located deeper into the engine which has the potential of being muffled by the turbomachinery directly upstream. Further research will be conducted to study the true effects of this LPC's contribution to the engine's overall noise emissions.

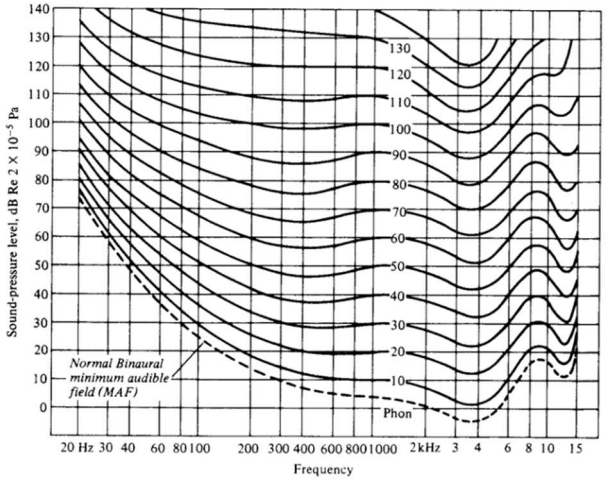

Figure 92: Equal-loudness contours for pure tones as studies by Penn State [5]

8.2.2 **Acoustic Liners**

Modern engines in service today, such as the GEnx, GE90, CFM56, Trent 1000 and others use acoustic liners along the fan casing. The purpose of the liners is to absorb some of the sound waves propagating from the fan blades. The majority of noise emission of turbofan and turbojet engines emit from the fan and the nozzle (jet noise). The current design of this fan has high flow tip speeds and rotational speeds. The first rotor blades see a M_U of 1.247 and a blade-passing frequency of 2565.2 Hz. Although no sound testing can be done at this early phase of design, historical data shows that this design could produce high noise emissions.

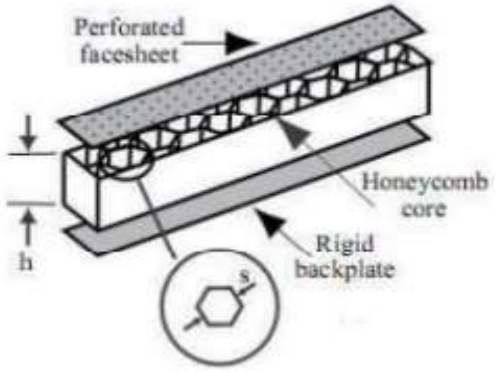

Figure 93: Schematic of standard acoustic liners used in modern aircraft engines today [1]

Further research will be conducted in order to better estimate the sound reduction by incorporating acoustic liners in the fan casing. The high M_U and f_{Hz} were allowed in the design by the assumption that the technology available by 2030 will allow for enough improvements in noise mitigation.

8.2.3 Trailing Edge Blowing (TEB)

A study conducted by Wenjie Wang and Peter Thomas of Beihang University in Beijing shows that this new technology could reduce sound levels by 10 dB by using 5% of the inlet mass flow. As mentioned in the report, when a rotor passes the viscous vortex wake from an upstream stationary blade, it is subject to unsteady loads. The TEB method essentially pulses air flow to the passing rotor and has the ability to delay flow separation on the rotor. This is shown clearly in **Figure 94** [11].

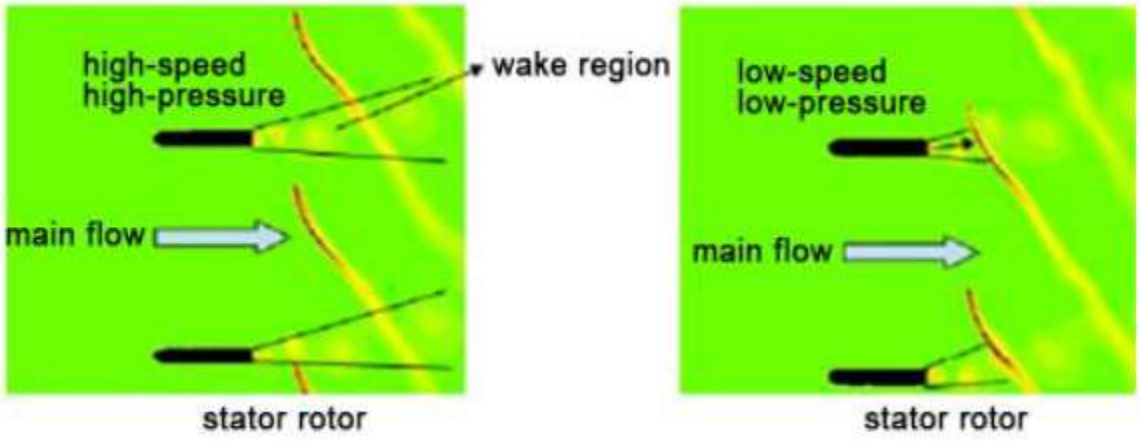

Figure 94: Representative schematic of TEB affecting boundary layer separation on a passing row of rotors [11]

The current engine design has a cross-sectional diameter that is 2.5% smaller than the limitation given by the RFP. Therefore, if additional mass flow is required to incorporate TEB to the IGV, then the engine can be scaled to accommodate such changes.

8.3 Lubrication Systems

The lubrication system for the BFTJ-56 will provide lubrication between moving parts such as ball bearings for the shaft to securely rotate in place. The lubricant will also aid cleaning out particulates within the bearings and aid in cooling required for the bearings within the turbine wheels. The oil used for lubrication is Mobil Jet II Turbine Oil (MIL-PRF-23699). The BFTJ-56 will utilize a dry-sump lubrication system. This will require the need for an oil tank, pump, piping, filters, and an oil cooler. **Figure 95** displays a general depiction of a dry-sump lubrication system used by an axial flow turbine engine.

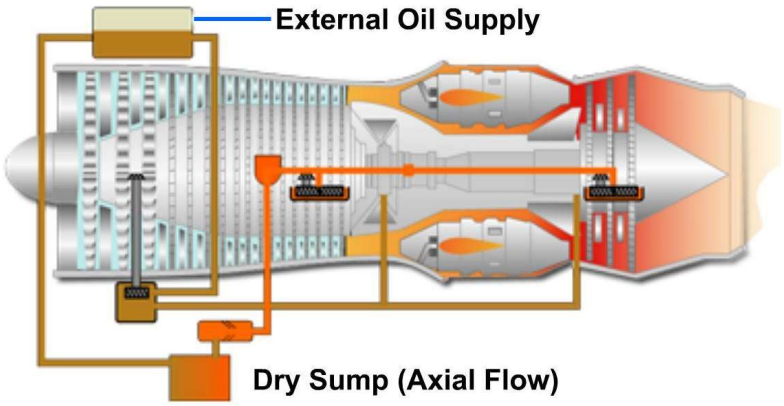

Figure 95: Dry sump oil lubrication system [16]

The oil supply will need a source to cool its temperature due to cooling of the turbine bearings. This cooling will come from the fuel supply and will act as a heat exchanger, with heat transferring from the high temperature oil to the lower temperature fuel. **Figure 96** illustrates the implementation of a heat exchanger between the fuel and oil supply.

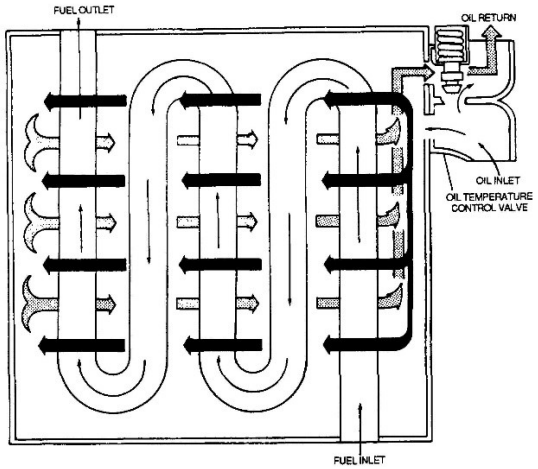

Figure 96: Heat exchanger between fuel and oil

The oil pump of the lubrication system is a gear-type oil pump. This type of oil pump has two elements, pressure oil and scavenge oil. **Figure 97** shows a general illustration of the gear-type oil pump that will be used by the engine's lubrication system. **Figure 98** breaks down the lubrication system by subsystems and components used.

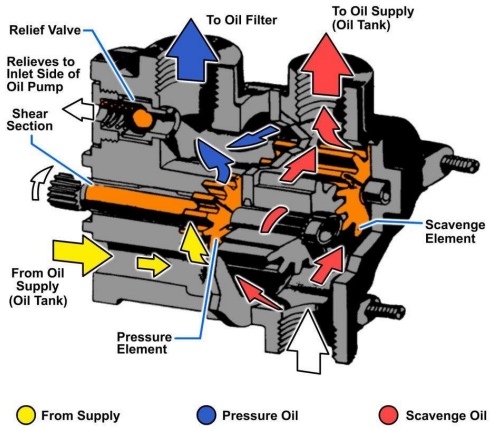

Figure 97: Illustration of gear-type oil pump [16]

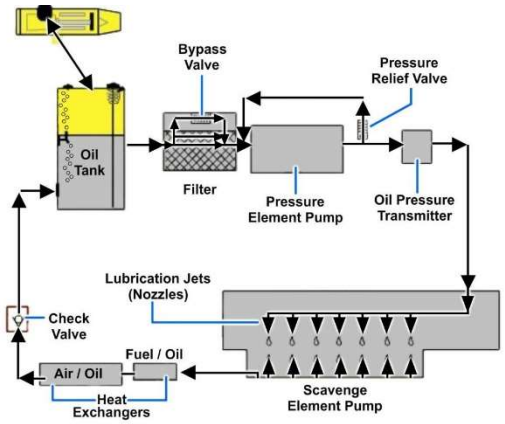

Figure 98: Schematic of lubrication system [16]

9 Conclusion and Recommendations

The BFTJ-56 is a two-spool turboramjet engine capable of cruising at Mach 0.98 and up to Mach 3.0. BFTJ-56 out competes the baseline engine described in the RFP in all aspects. The BFTJ-56 is capable of achieving the required thrust for the Mach 1.15, 2.1, and 3.0 flight conditions while the baseline engine does not, according to the GasTurb model. Additionally, at the subsonic flight conditions the BFTJ-56 can achieve the required thrust at a lower TIT than the baseline engine. All this is possible while reducing the engine diameter by ~2.5% with a total length of 26.6 [ft], ~21.8% smaller than the allowed per the nacelle requirements.

The BFTJ-56 consists of a 3-5-1-1 architecture that achieves an OPR of 20:1. The variable geometry inlet design resembles that of the SR-71 inlet and achieves a 72.8% total PR recovery at Mach 3.0 and 91% at Mach 0.98. The LPC and HPC designs perform well on and off-design with the lowest surge margins being 22.4% and 26.9% for each, respectively.

The turbine was designed with a single-stage HPT and LPT, with no inter-turbine duct. Cooling is not necessary due to material technological advancements by 2030, allowing temperatures in the turbine to reach up to 4000 [°R] [13]. However, to alleviate thermal stress in vanes and blades of the HPT and LPT, they are protected by two layers of Zirconia-Yttria TBCs. Further thermal and stress analysis is recommended to optimize the design of the turbines. The nozzle was determined to not be perfectly expanded at all flight conditions. Further analysis can be conducted to determine the optimal expansion at each mission leg to maximize the jet thrust with respect to pressure thrust, jet velocity, and losses of the jet thrust through the nozzle.

The BFTJ-56 at his preliminary design phase meets all requirements and is therefore a feasible engine that is worth pursuing further and worth taking to the next level.

References

[1] Azimi, Mohammadreza & Fatholla Ommi. (2014). *Using Acoustic Liner for Fan Noise Reduction in Modern Turbofan Engines.* International Journal of Aeronautical and Space Sciences. Modares University, Tehran, Iran.

[2] Dannaemann, Martin, & Kucher, Michael. (2018). *Experimental Study of Advanced Helmholtz Resonator Liners with Increased Acoustic Performance by Utilizing Material Damping Effects.* Institude of Lightweight Engineering and Polymer Technology. Dresden, Germany. MDPI Journal.

[3] Fite, Brain E. (2006). *Aerodynamic Performance Measurements for a Forward Swept Low Noise Fan.* NASA. Glenn Research Center, Cleveland, OH.

[4] Lieblein, Seymour, & Schwenk, Francis C., & Broderick, Robert L. (1953). *Diffusion Factor For Estimating Losses And Limiting Blade Loadings In Axial-Flow-Compressor Blade Elements.* NACA Research Memorandum. Lewis Flight Propulsion Laboratory. Cleveland, OH.

[5] Penn State University. (2000). *Human Response to Sound.* Noise Control.

[6] Kline, S. J., Abbot, D.E., & Fox, R. W. (1959). *Optimum Design of Straight-Walled Diffusers.* Journal of Basic Engineering, 321-331.

[7] Mattingly, J. D. (1996). *Elements of Gas Turbine Propulstion (J.J. Corriagn, & J. W. Bradley, Eds.)* New York: McGraw Hill.

[8] Mattingly, J. D., Heiser, W. H., & Pratt, D. T. (2002). *Aircraft Engine Design (2n ed.)* (J. S. Przemieniecki, Ed.) Reston, Virginia, United States of America: American Institute of Aeronautics and Astronautics Inc.

[9] Farokhi, S. (2014). *Aircraft Propulsion* (2nd ed.). Chichester, West Sussex, United Kingdom: John Wiley & Sons Ltd.

[10] Sofrin, T. G., & Pickett, G.F. *Multiple Pure Tone Noise Generated by Fans at Supersonic Tip Speeds.* Pratt & Whitney Aircraft Division United Aircraft Corporation.

[11] Wang, Wenjie, & Thomas, Peter J. (2018). *Acoustic Improvement of Stator-Rotor Interaction with Nonuniform Trailing Edge Blowing.* Fluid and Acoustic Engineering Laboratory, Beihang University, Beijing, China. MDPI Journal.

[12] Gunston, B. *The Development of Jet and Turbine Aero Engines* 2nd Ed. 1997

[13] Knip, Gerald, Jr. Analysis of an Advanced Technology Subsonic Turbofan Incorporating Revolutionary Materials. Cleveland: National Aeronautics & Space Administration, 1987.

[14] Lefebvre, Arthur H, and Dilip R. Ballal. *Gas Turbine Combustion: Alternative Fuels and Emissions*. Boca Raton: Taylor & Francis, 2010. Print.

[15] Melconian, J.O; Modak, A.T. Combustor design. In: SAWYER, JAW. (Ed.) Sawyer's gas turbine engineering handbook design. Volume 1, Theory & design. 3. ed. Connecticut: Turbo machinery International Publications, 1985. v.1, Chapter. 5, p 5-1-5-62

[16] United States Navy, Aviation Machinists Mate 3&2, NAVEDTRA 14008

[17] S. Manning Meier and D.K. Gupta, The evolution of thermal barrier coatings in gas turbine engine applications Journal of Engineering for Gas Turbines and Power; Vol. 116, 250-257, 1994

Appendix A LPC Thermodynamic and Aerodynamic Data

Table 54: Complete thermodynamic properties of LPC (mid-span), entering values

	Units	IGV	R1	S1	R2	S2	R3	S3	Exit
P_0	[psia]	10.21	10.15	17.45	17.29	25.55	25.33	34.77	34.50
P	[psia]	7.95	7.89	11.31	13.54	16.83	20.38	24.35	28.64
T_0	[°R]	589.8	589.8	698.8	698.8	787.3	787.3	868.1	868.1
T	[°R]	549.1	549.0	617.4	651.7	698.7	740.0	784.0	823.1
h_0	[BTU/lb_m]	141.51	141.51	167.66	167.66	188.89	188.89	208.27	208.27
h	[BTU/lb_m]	131.75	131.71	148.14	156.35	167.64	177.53	188.10	197.48
ρ	[lb_m ft^{-3}]	0.03908	0.03881	0.04945	0.05609	0.06500	0.07436	0.08383	0.09392
a	[ft s^{-1}]	1148.7	1148.5	1218.0	1251.3	1295.7	1333.4	1372.5	1406.3
Area	[ft^2]	1074.9	1093.4	850.3	749.7	646.9	565.5	501.6	430.5

Table 55: LPC thermodynamic characteristics

Stage #	η_{tt}	π	τ	ΔP_0 [psia]	ΔT_0 [°R]	Δh_0[BTU lb_m^{-1}]
1	0.89	1.704	1.185	7.562	109	26.15
2	0.91	1.465	1.127	8.608	88.5	21.23
3	0.90	1.362	1.103	9.826	80.8	19.38

Table 56: Complete LPC aerodynamic properties (Mid), entering values

	Stations							
	R1	**S1**	**R2**	**S2**	**R3**	**S3**	**Exit**	**Units**
α	9.00	45.07	21.90	47.40	22.20	45.98	8.90	[°]
β	53.64	29.79	49.92	26.71	49.70	28.92	53.25	[°]
V	700.6	988.8	752.6	1031.6	754.2	1004.9	735.1	$[ft\ s^{-1}]$
V_{ax}	691.9	698.3	698.3	698.3	698.3	698.3	726.2	$[ft\ s^{-1}]$
V_u	109.6	700.0	280.7	759.3	285.0	722.7	113.7	$[ft\ s^{-1}]$
W	1167.0	804.6	1084.7	781.8	1079.7	797.8	1213.8	$[ft\ s^{-1}]$
Wu	939.7	399.7	830.0	351.4	823.5	385.8	972.6	$[ft\ s^{-1}]$
U	1049.3	1099.7	1110.7	1110.7	1108.5	1108.5	1086.3	
M_{rel}	1.02	0.81	0.87	0.80	0.81	0.73	0.52	
M_U	0.91	0.90	0.89	0.86	0.83	0.81	0.77	
	R1	**S1**	**R2**	**S2**	**R3**	**S3**		
Δα	-	20.1	-	25.2	-	37.1		[°]
Δβ	23.9	-	23.2	-	20.8	-		[°]
σ_S	41.7	33.5	38.3	34.8	39.3	27.4		[°]

Appendix B High Pressure Compressor Data

Table 57: Blade Data for HPC Rotors

		Rotor 1	Rotor 2	Rotor 3	Rotor 4	Rotor 5
NOB		32	55	84	109	139
b_{avg} [in]		4.116	2.740	2.139	1.801	1.490
AR		1.80	1.90	2.00	2.10	2.20
TR		0.90	0.90	0.90	0.90	0.90
c [in]	TIP	2.546	1.535	1.123	0.892	0.692
	MID	2.287	1.442	1.070	0.858	0.677
	HUB	2.044	1.349	1.013	0.819	0.658
s [in]	TIP	2.124	1.569	1.139	0.902	0.706
	MID	1.827	1.432	1.065	0.853	0.675
	HUB	1.530	1.295	0.992	0.805	0.643
c_{ax} [in]	TIP	1.570	1.000	0.731	0.554	0.406
	MID	1.657	1.056	0.771	0.585	0.428
	HUB	1.744	1.111	0.812	0.615	0.451
Δβ [°]	TIP	17.5	16.9	15.0	13.0	11.5
	MID	23.9	21.6	19.2	16.1	13.5
	HUB	33.5	28.0	24.7	20.0	16.2
σ_s [°]	TIP	51.9	49.3	49.4	51.6	54.1
	MID	43.6	42.9	43.9	47.0	50.8
	HUB	31.4	34.5	36.8	41.3	46.8

Table 58: Blade Data for HPC Stators

		IGV	Stator 1	Stator 2	Stator 3	Stator 4	Stator 5	OGV
NOB		32	55	84	109	139	178	188
b_{avg} [in]		4.916	3.255	2.360	1.958	1.638	1.354	1.314
AR		1.80	1.85	1.95	2.05	2.15	2.25	2.30
TR		1.10	1.10	1.10	1.10	1.10	1.10	1.10
c [in]	TIP	2.854	1.783	1.230	0.971	0.779	0.619	0.597
	MID	2.731	1.759	1.211	0.955	0.762	0.602	0.571
	HUB	2.611	1.747	1.195	0.941	0.746	0.585	0.546
s [in]	TIP	3.183	1.944	1.298	1.006	0.795	0.625	0.593
	MID	2.682	1.744	1.206	0.948	0.757	0.600	0.571
	HUB	2.181	1.544	1.113	0.889	0.718	0.575	0.550
c_{ax} [in]	TIP	2.834	1.453	0.920	0.667	0.529	0.436	0.568
	MID	2.705	1.387	0.878	0.636	0.505	0.416	0.542
	HUB	2.576	1.321	0.836	0.606	0.481	0.396	0.516
Δα [°]	TIP	13.9	21.5	17.0	14.7	16.8	18.8	35.8
	MID	16.0	22.6	17.3	14.7	16.8	18.9	36.8
	HUB	18.9	23.6	17.5	14.7	16.9	19.0	37.9
σ_s [°]	TIP	6.9	35.4	41.6	46.6	47.2	45.2	17.9
	MID	8.0	38.0	43.5	48.2	48.4	46.3	18.4
	HUB	9.5	40.9	45.6	49.9	49.8	47.4	18.9

Table 59: Complete Thermodynamics of High-Pressure Compressor, entering values

	Units	IGV	R1	S1	R2	S2	R3	S3	R4	S4	R5	S5	OGV	Exit
P	[psi]	29.1	27.9	38.6	47.1	60.3	73.2	88.1	104.7	120.2	139.5	158.4	179.1	188.6
P0	[psi]	34.5	34.4	58.4	57.8	89.5	88.7	124.9	123.9	162.0	160.9	203.3	202.1	201.5
h	[Btu lbm^{-1}]	198.4	196.5	218.0	231.2	249.5	264.3	279.6	294.2	306.8	320.5	333.1	345.3	350.7
h_0	[Btu lbm^{-1}]	208.3	208.3	245.2	245.2	279.0	279.0	308.5	308.5	333.6	333.6	357.2	357.2	357.2
T	[°R]	825.4	818.3	907.3	961.0	1034.6	1093.6	1154.2	1211.9	1260.8	1314.3	1362.6	1409.6	1430.1
T_0	[°R]	865.8	867.8	1017.2	1017.2	1152.1	1152.1	1267.7	1267.7	1364.7	1364.7	1454.9	1454.9	1454.9
C_p	[Btu lbm^{-1} R^{-1}]	0.244	0.244	0.246	0.247	0.250	0.251	0.253	0.255	0.257	0.258	0.260	0.261	0.262
γ		1.400	1.391	1.386	1.383	1.379	1.375	1.371	1.367	1.364	1.361	1.358	1.356	1.354

Table 60: HPC Stage Thermodynamic Characteristics

Stage #	η_{tt}	π	τ	ΔP_0 [psi]	ΔT_0 [R]	Δh_0[Btu lbm^{-1}]
1	0.89	1.684	1.177	23.5	149.4	36.9
2	0.90	1.534	1.138	30.9	134.9	33.9
3	0.91	1.397	1.106	35.2	115.6	29.5
4	0.90	1.298	1.081	36.9	97.0	25.1
5	0.89	1.257	1.071	41.3	90.2	23.6
HPC	0.864	5.88	1.715	167.8	589.1	148.9

Table 61: Aerodynamics of HPC MID Radius, entering values

	Units	IGV	R1	S1	R2	S2	R3	S3	R4	S4	R5	S5	OGV	Exit
α	[°]	0.0	16.0	49.3	26.7	52.1	34.9	55.6	40.9	56.9	40.0	55.7	36.8	0.0
β	[°]	0.0	55.5	31.6	53.8	32.1	53.4	34.3	55.0	39.0	57.6	44.0	0.0	0.0
V_{ax}	[ft s^{-1}]	704.1	739.0	761.9	746.6	746.6	705.6	680.9	640.0	633.6	619.0	619.0	617.2	570.9
V_u	[ft s^{-1}]	0.0	211.9	884.6	375.5	960.0	491.3	993.1	553.4	970.7	520.0	907.8	461.9	0.0
V	[ft s^{-1}]	704.1	768.7	1167.4	835.7	1216.1	859.8	1204.1	846.1	1159.2	808.5	1098.7	770.9	570.9
W_u	[ft s^{-1}]	0.0	1076.9	468.6	1018.3	468.7	951.7	464.3	915.6	513.0	974.1	598.3	0.0	0.0
W	[ft s^{-1}]	704.1	1306.0	894.5	1262.7	881.5	1184.7	824.1	1117.1	815.2	1154.2	860.9	1220.7	1629.0
U	[ft s^{-1}]	0.0	1288.8	1353.2	1393.8	1428.7	1442.9	1457.4	1469.0	1483.7	1494.1	1506.1	1515.1	1525.7
M_{rel}		0.500	0.934	0.795	0.836	0.777	0.738	0.731	0.662	0.675	0.659	0.617	0.674	0.313

Appendix C Turbine Data

Table 62: Blade data for Turbine Blades

		HPT		LPT	
		Stator 1	Rotor 1	Stator 2	Rotor 2
NOB		40	56	69	86
b_{avg} [in]		2.563	2.929	3.687	5.079
AR		0.8	0.92	1.59	2.7
TR		1.1	0.9	1.1	0.9
c [in]	Tip	2.90	2.09	1.70	1.39
	Mid	2.71	1.93	1.55	1.23
	Hub	2.52	1.78	1.41	1.08
s [in]	Tip	2.85	2.93	2.28	1.69
	Mid	2.72	3.09	2.18	1.79
	Hub	2.59	3.26	2.07	1.88
c_{ax} [in]	Tip	3.33	3.14	2.41	1.91
	Mid	3.20	3.18	2.32	1.88
	Hub	3.08	3.28	2.22	1.91
$\Delta\alpha$ or $\Delta\beta$ [°]	Tip	62.24	73.86	64.03	63.53
	Mid	64.00	85.36	68.44	76.04
	Hub	65.82	95.06	73.37	87.60
σ_s [°]	Tip	-31.12	20.99	-19.02	27.51
	Mid	-32.00	13.66	-20.08	18.24
	Hub	-32.91	7.18	-21.18	9.21

Table 63: Turbine Aerodynamic Data, entering values

		S1	R1	S2	R2	Exit	Units
Hub	α	0	65.8	15.5	57.9	16.7	[°]
	β	0	40.4	54.7	34.6	53.0	[°]
	V_{ax}	865.8	1021.6	1210.3	992.4	803.4	[ft/s]
	V_u	0.0	2275.0	335.7	1579.8	241.4	[ft/s]
	V	865.8	2493.8	1256.0	1865.7	838.9	[ft/s]
	W	0.0	1340.6	2095.1	1205.6	1335.3	[ft/s]
	U	0.0	1406.9	1374.4	895.4	825.2	[ft/s]
	M	0.300	0.907	0.475	0.712	0.325	
	M_r	0.000	0.488	0.793	0.460	0.517	
	M_U	0.000	0.512	0.520	0.342	0.319	
Mid	α	0.0	64.0	14.1	54.3	13.9	[°]
	β	0.0	29.0	56.3	19.8	56.3	[°]
	V_{ax}	865.8	1021.6	1210.3	992.4	803.4	[ft/s]
	V_u	0.0	2094.7	305.0	1381.1	198.4	[ft/s]
	V	865.8	2330.5	1248.1	1700.7	827.5	[ft/s]
	W	0.0	1168.3	2183.9	1054.7	1446.3	[ft/s]
	U	0.0	1528.0	1512.9	1024.2	1004.3	[ft/s]
	M	0.300	0.848	0.472	0.649	0.320	
	M_r	0.000	0.425	0.826	0.403	0.560	
	M_U	0.000	0.556	0.572	0.391	0.389	
Tip	α	0.0	62.2	13.0	51.0	11.8	[°]
	β	0.0	15.9	57.9	4.3	59.3	[°]
	V_{ax}	865.8	1021.6	1210.3	992.4	803.4	[ft/s]
	V_u	0.0	1940.9	279.4	1226.9	168.3	[ft/s]
	V	865.8	2193.3	1242.1	1578.0	820.9	[ft/s]
	W	0.0	1062.5	2278.8	995.2	1572.4	[ft/s]
	U	0.0	1649.1	1651.4	1152.9	1183.4	[ft/s]
	M	0.300	0.798	0.470	0.602	0.318	
	M_r	0.000	0.387	0.862	0.380	0.609	
	M_U	0.000	0.600	0.625	0.440	0.458	

Appendix D Engine Candidate List

Table 64 - Engine Selection Workbook pg.3

M_{ref}	1.6
h_{ref} [ft]	40000

Engine #	Pi C	PicL	Tt4 [°R]	Tt7 [°R]	$\dot{m}_{ref}$ [lbm/s]	TSL/WTO	Subsonic Fuel [lbm]	Supercruise Fuel [lbm]	M = 0.98 Thrust [lbf]	A_0 [ft^2]	A_9 [ft^2]	M = 1.15 Thrust [lbf]	A_0 [ft^2]	A_9 [ft^2]	M=2.1 Thrust [lbf]	A_0 [ft^2]	A_9 [ft^2]	M = 3 Thrust [lbf]	A_0 [ft^2]	A_9 [ft^2]
16BB (TJ)	35	4.5	3600	-	834.6	0.7436	82492	87426	10401	11.9	13.8	20812	15.8	17.8	45760	22.8	28.4	30999	33.7	48.8
16BB_AB	35	4.5	3600	2800	661.8	0.6751	82366	87120	10552	10.4	12.3	20394	13.8	15.9	45038	20	24.9	30999	26.7	44.4
16BB_AB1	35	5	3750	3700	522.2	0.623	82134	86685	10184	8.7	10.6	20171	12	14	45001	17.6	21.7	31114	21.2	37.8
16BBA	30	4	3600	-	760.8	0.6888	82956	87505	10254	11.2	13	20770	15.1	16.7	45371	21.5	27	30998	31.8	46.3
16BBB	25	4	3600	-	689.6	0.6336	83568	87677	10268	10.7	12.3	20510	14.3	15.8	44949	20.2	25.7	31100	30.1	44.2
16BBC	30	4	3600	3700	511.3	0.6076	82430	86585	10775	8.8	11.1	20175	12	13.8	45004	17.4	21.7	31150	21.4	37.8
16BBD	30	4	3600	4200	526.5	0.6645	82302	86696	10230	9.1	10.9	20240	12.4	14.3	45000	18	22.4	31015	22.1	38.6
16BBE	30	4	3700	3700	508.5	0.603	82541	86757	10164	8.7	10.5	20341	12	13.9	45000	17.4	21.7	31084	21.3	37.7
16BBF	25	4	3700	3700	484.7	0.5728	83113	86872	10249	8.6	10.2	20689	11.9	13.5	45002	16.8	21.3	31086	21.2	37.1
16BBG	20	3.4	3700	3700	460.1	0.5386	83845	87023	10422	8.6	10	20231	11.8	12.9	44999	16.3	21.1	31095	21.3	36.3
16BBH	28	4	3750	3700	491.2	0.5844	82849	86840	10577	8.6	10.4	20973	11.9	13.7	44999	16.9	21.2	31385	20.95	37.1
16BBI	32	4	3750	3700	509.3	0.6068	82442	86763	10230	8.7	10.5	20245	11.9	13.8	44998	17.3	21.5	31066	21.1	37.4
16BBJ	32	4.5	3750	3700	509.1	0.607	82418	86745	10419	8.7	10.6	20252	11.9	13.8	45002	17.3	21.5	31057	21	37.4
16BBK	32	5	3750	3700	508.8	0.6071	82397	86728	10235	8.6	10.5	20255	11.8	13.8	44996	17.3	21.4	31038	21	37.4
16BBL	20	3.4	3500	3700	490.9	0.5652	83472	86884	10553	9.3	10.8	20657	12.6	13.9	45003	17.3	22.4	31081	22.7	39

Appendix E GasTurb Baseline Cycle Verification

Property	*Unit*	*Value*	*Comment*
Intake Pressure Ratio		1	
No (0) or Average (1) Core dP/P		1	
Inner Fan Pressure Ratio		1.8	
Outer Fan Pressure Ratio		2	
Core Inlet Duct Press. Ratio		1	
IP Compressor Pressure Ratio		2.8	
Compr. Interduct Press. Ratio		0.98	
HP Compressor Pressure Ratio		4.25	
Bypass Duct Pressure Ratio		0.975	
Turb. Interd. Ref. Press. Ratio		0.98	
Design Bypass Ratio		1.7	
Burner Exit Temperature	R	2492	
Burner Design Efficiency		0.9995	
Burner Partload Constant		1.6	used for off design only
Fuel Heating Value	BTU/lb	18552.4	
Overboard Bleed	lb/s	0	
Power Offtake	hp	100	
HP Spool Mechanical Efficiency		0.98	
Gear Ratio		1	
LP Spool Mechanical Efficiency		0.99	
Burner Pressure Ratio		0.95	
Turbine Exit Duct Press Ratio		0.99	
Hot Stream Mixer Press Ratio		1	
Cold Stream Mixer Press Ratio		1	
Mixed Stream Pressure Ratio		1	
Mixer Efficiency		0.6	
Design Mixer Mach Number		0.4603	
Design Mixer Area	in²	0	

Figure 99: AIAA Baseline Engine GasTurb Input File

```
          W         T         P        WRstd
Station  lb/s        R        psia       lb/s
 amb                518.67    14.696
  2     479.000     518.67    14.696    479.000
 13     301.592     650.05    29.392    168.818
 21     177.407     623.79    26.453    108.087
 22     177.407     623.79    26.453    108.087
 24     177.407     853.05    74.068     45.142
 25     177.407     853.05    72.586     46.063
  3     172.085    1312.61   308.492     13.041
 31     152.570    1312.61   308.492
  4     155.430    2492.00   293.067     17.084
 41     164.301    2432.72   293.067     17.843
 43     164.301    1997.55   117.715
 44     174.945    1958.21   117.715
 45     179.676    1937.76   114.220     44.684
 49     179.676    1453.87    32.261
  5     180.267    1453.01    32.261    137.442
  6     180.267    1453.01    31.939
 16     301.592     650.05    28.657
 64     481.860     962.78    29.778
  8     481.860     962.78    29.778    324.001
Bleed     0.000    1312.61   308.492
-----------------------------------------------
Efficiencies:   isentr  polytr    RNI     P/P
 Outer LPC      0.8622  0.8749  1.000   2.000
 Inner LPC      0.9000  0.9079  1.000   1.800
 IP Compressor  0.9197  0.9303  1.445   2.800
 HP Compressor  0.9010  0.9180  2.729   4.250
 Burner         0.9995                 0.950
 HP Turbine     0.9219  0.9136  3.271   2.490
 LP Turbine     0.9268  0.9151  1.653   3.540
 Mixer          0.6000
-----------------------------------------------
HP Spool mech Eff 0.9800  Nom Spd  14372 rpm
LP Spool mech Eff 0.9900  Nom Spd   6482 rpm
P22/P21=1.0000 P25/P24=0.9800 P45/P44=0.9703
-----------------------------------------------

FN       =  21698.96 lb
TSFC     =    0.4745 lb/(lb*h)
WF       =    2.8601 lb/s
s NOX    =    0.5983

Core Eff =    0.4370
Prop Eff =    0.0000
BPR      =    1.7000
P2/P1    =    1.0000
P3/P2    =     20.99
P5/P2    =    2.1952
P16/P13  =    0.9750
P16/P6   =   0.89726
P16/P2   =   1.95000
P6/P5    =   0.99000
P63/P6   =   1.00000
P163/P16 =   1.00000
XM63     =   0.56091
XM163    =   0.37699
XM64     =   0.46030
A64      =   1352.53 in²
WBld/W2  =   0.00000
A8       =    987.27 in²
CD8      =   0.96000
XM8      =   1.00000
PWX      =     100.0 hp
WBLD/W22 =   0.00000
Wreci/W25=   0.00000
Loading  =    100.00 %
e444 th  =   0.89002
WBLD/W25 =   0.00000
WCHN/W25 =   0.05000
WCHR/W25 =   0.06000
WCLN/W25 =   0.02667
WCLR/W25 =   0.00333
WLkBy/W25=   0.00000
```

Figure 100: AIAA Baseline Engine GasTurb On-Design Output File (RFP)

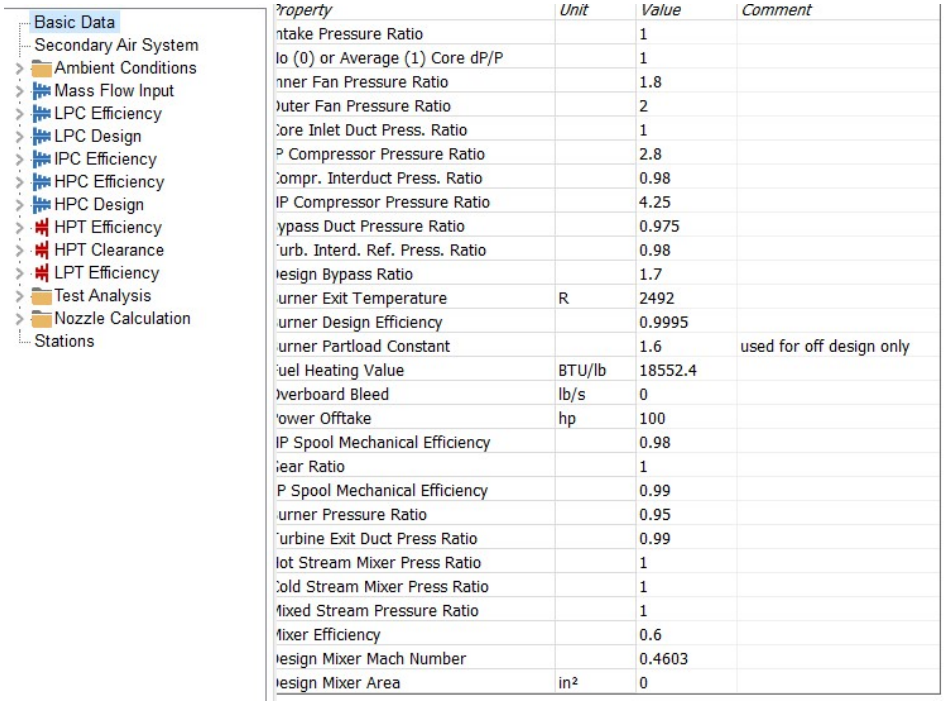

- Basic Data
- Secondary Air System
- Ambient Conditions
- Mass Flow Input
- LPC Efficiency
- LPC Design
- IPC Efficiency
- HPC Efficiency
- HPC Design
- HPT Efficiency
- HPT Clearance
- LPT Efficiency
- Test Analysis
- Nozzle Calculation
- Stations

Property	Unit	Value	Comment
ntake Pressure Ratio		1	
lo (0) or Average (1) Core dP/P		1	
nner Fan Pressure Ratio		1.8	
Outer Fan Pressure Ratio		2	
Core Inlet Duct Press. Ratio		1	
P Compressor Pressure Ratio		2.8	
Compr. Interduct Press. Ratio		0.98	
IP Compressor Pressure Ratio		4.25	
ypass Duct Pressure Ratio		0.975	
Turb. Interd. Ref. Press. Ratio		0.98	
esign Bypass Ratio		1.7	
urner Exit Temperature	R	2492	
urner Design Efficiency		0.9995	
urner Partload Constant		1.6	used for off design only
uel Heating Value	BTU/lb	18552.4	
verboard Bleed	lb/s	0	
ower Offtake	hp	100	
IP Spool Mechanical Efficiency		0.98	
ear Ratio		1	
P Spool Mechanical Efficiency		0.99	
urner Pressure Ratio		0.95	
Turbine Exit Duct Press Ratio		0.99	
lot Stream Mixer Press Ratio		1	
Cold Stream Mixer Press Ratio		1	
Mixed Stream Pressure Ratio		1	
Mixer Efficiency		0.6	
esign Mixer Mach Number		0.4603	
esign Mixer Area	in²	0	

Figure 101: Design Team GasTurb Input File (Baseline Engine Replication)

```
          W         T         P        WRstd
Station  lb/s        R       psia        lb/s
 amb                518.67    14.696
  2     478.999     518.67    14.696    479.000
 13     301.592     649.71    29.392    168.773
 21     177.407     627.41    26.453    108.400
 22     177.407     627.41    26.453    108.400
 24     177.407     857.94    74.067     45.271
 25     177.407     857.94    72.586     46.195
  3     172.084    1319.67   308.490     13.076
 31     152.570    1319.67   308.490
  4     155.414    2492.00   293.066     17.082
 41     164.284    2433.04   293.066     17.842
 43     164.284    1995.33   117.062
 44     174.928    1956.48   117.062
 45     179.659    1936.21   114.721     44.467
 49     179.659    1448.31    31.991
  5     180.251    1447.48    31.991    138.326
  6     180.251    1447.48    31.671
 16     301.592     649.71    28.657
 64     481.843     960.29    29.683
  8     481.843     960.29    29.683    324.598
Bleed    0.000    1319.67   308.490
-------------------------------------------------
Efficiencies:   isentr  polytr    RNI    P/P
 Outer LPC      0.8645  0.8770  1.000  2.000
 Inner LPC      0.8700  0.8803  1.000  1.800
 IP Compressor  0.9197  0.9303  1.435  2.800
 HP Compressor  0.9010  0.9180  2.711  4.250
 Burner         0.9995                 0.950
 HP Turbine     0.9220  0.9136  3.271  2.504
 LP Turbine     0.9270  0.9151  1.662  3.586
 Mixer          0.6000
-------------------------------------------------
HP Spool mech Eff 0.9800  Speed    14351 rpm
LP Spool mech Eff 0.9900  Speed     6482 rpm
P22/P21=1.0000 P25/P24=0.9800 P45/P44=0.9800
-------------------------------------------------
hum [%]     war0       FHV     Fuel
   0.0   0.00000   18552.4    Generic
```

```
FN       =  21618.08 lb
TSFC     =     0.4736 lb/(lb*h)
WF       =     2.8440 lb/s
s NOX    =     0.6104
P5/P2    =     2.1769 EPR
Core Eff =     0.4357
Prop Eff =     0.0000
BPR      =     1.7000
P2/P1    =     1.0000
P3/P2    =      20.99
P5/P2    =     2.1769
P16/P13  =     0.9750
P16/P6   =    0.90483
P16/P2   =    1.95000
P6/P5    =    0.99000
P63/P6   =    1.00000
P163/P16 =    1.00000
XM63     =    0.55152
XM163    =    0.38039
XM64     =    0.46030
A64      =    1354.95 in²
WBld/W2  =    0.00000
A8       =     984.94 in²
CD8      =    0.96400
XM8      =    1.00000
PWX      =      100.0 hp
WBLD/W22 =    0.00000
Wreci/W25=    0.00000
Loading  =     100.00 %
e444 th  =    0.88989
WBLD/W25 =    0.00000
WCHN/W25 =    0.05000
WCHR/W25 =    0.06000
WCLN/W25 =    0.02667
WCLR/W25 =    0.00333
WLkBy/W25=    0.00000
```

Figure 102: Design Team GasTurb Output File (Baseline Engine Replication)

```
          W         T         P        WRstd
Station  lb/s       R        psia       lb/s
 amb               389.97     1.040
  2    424.251   1082.60    31.118   289.462
 13    347.897   1113.15    32.900   227.660
 21     76.354   1106.98    32.543    50.372
 22     76.354   1106.98    32.543    50.372
 24     76.352   1270.75    52.858    33.227
 25     76.352   1270.75    52.289    33.589
  3     74.061   1671.33   134.284    14.550
 31     65.663   1671.33   134.284
  4     66.534   2492.00   125.972    17.014
 41     70.352   2449.48   125.972    17.836
 43     70.352   2045.01    55.050
 44     74.933   2023.01    55.050
 45     76.969   2010.12    54.105    41.156
 49     76.969   1712.71    26.194
  5     77.223   1712.20    26.194    78.718
  6     77.223   1712.20    26.109
 16    347.897   1113.15    31.403
 64    425.120   1226.76    29.693
  8    425.120   1226.76    29.693   323.581
Bleed    0.000   1671.33   134.285
-----------------------------------------------
Efficiencies:   isentr  polytr    RNI    P/P
 Outer LPC      0.5370  0.5404  0.882  1.057
 Inner LPC      0.5404  0.5431  0.882  1.046
 IP Compressor  0.9449  0.9484  0.898  1.624
 HP Compressor  0.8835  0.8967  1.228  2.568
 Burner         0.9995                 0.938
 HP Turbine     0.9230  0.9156  1.396  2.288
 LP Turbine     0.9050  0.8969  0.751  2.066
 Mixer          0.6000
-----------------------------------------------
HP Spool mech Eff 0.9800  Speed    14343 rpm
LP Spool mech Eff 0.9900  Speed     5100 rpm
P22/P21=1.0000 P25/P24=0.9892 P45/P44=0.9828
-----------------------------------------------
hum [%]     war0       FHV     Fuel
   0.0   0.00000   18552.4    Generic
```

```
FN        =  -3190.51 lb
TSFC      =   -0.9832 lb/(lb*h)
WF        =    0.8714 lb/s
s NOX     =    1.1958
P5/P2     =    0.8418 EPR
Core Eff  =    0.5956
Prop Eff  =    1.0445
BPR       =    4.5564
P2/P1     =    0.8088
P3/P2     =      4.32
P5/P2     =    0.8418
P16/P13   =    0.9545
P16/P6    =   1.20276
P16/P2    =   1.00915
P6/P5     =   0.99676
P63/P6    =   1.00000
P163/P16  =   1.00000
XM63      =   0.27512
XM163     =   0.59349
XM64      =   0.46092
A64       =   1354.95 in²
WBld/W2   =   0.00000
A8        =    984.94 in²
CD8       =   0.96400
XM8       =   1.00000
PWX       =     100.0 hp
WBLD/W22  =   0.00000
Wreci/W25=    0.00000
Loading   =    100.28 %
e444 th   =   0.88011
WBLD/W25  =   0.00000
WCHN/W25  =   0.05000
WCHR/W25  =   0.06000
WCLN/W25  =   0.02667
WCLR/W25  =   0.00333
WLkBy/W25=    0.00000
```

Figure 103: AIAA Baseline Engine GasTurb Output File (Off-Design at Mach 3) - Inoperable